Imperial College of Science, Technology and Medicine
Department of Physics

Optical diagnostics of ultra-thin target laser-plasma interactions

Emma-Jane Ditter

September 2019

Submitted in part fulfilment of the requirements for the degree of
Doctor of Philosophy of Imperial College London

Blackett Laboratory
Imperial College London
Prince Consort Road
London SW7 2BZ

Declaration

I hereby certify that the material of this thesis, which I now submit for the award of Doctor of Philosophy, is entirely my own work unless otherwise cited or acknowledged within the body of text.

Emma-Jane Ditter

August 2019

Copyright

The copyright of this thesis rests with the author and is made available under a Creative Commons Attribution Non-Commercial No Derivatives licence. Researchers are free to copy, distribute or transmit the thesis on the condition that they attribute it, that they do not use it for commercial purposes and that they do not alter, transform or build upon it. For any reuse or redistribution, researchers must make clear to others the licence terms of this work.

Abstract

This thesis presents experimental and simulation results of the properties of the reflected and transmitted light for laser interactions with thin foils spanning the relativistic transparency and the sheath or radiation pressure acceleration regime. These diagnostics were used to obtain a better understanding of the plasma properties and it's temporal evolution as it transitioned from an opaque plasma to a relativistically transparent one.

For thin foils $\leq$100 nm irradiated with intensities $\geq 10^{21}\,\mathrm{W\,cm^{-2}}$ at normal incidence, the dominant ion acceleration mechanism transitions from radiation pressure acceleration to relativistic transparency as the electron density of the plasma decreases below the relativistic critical density. This transition was diagnosed in the reflected and transmitted light both through the spatial profiles and the quantity of emitted energy, and through the pulse length and instantaneous frequency of the transmitted radiation. The limit of opacity was found to be 25 nm for the given experimental conditions. Differences between linear and circular polarisation were quantified and a study on harmonic generation on the front and rear surface was also completed. A temporal measurement of the coherent transition radiation emitted from targets $\geq$25 nm was made, measuring the lifetime of the hot electron bunch at $\sim$37 fs. These results were supported by 2D PIC simulations which allowed for further information on the electron heating and density variations to be obtained.

Imaging the target's front surface during a high power laser plasma interaction is often difficult due to experimental constraints and the high levels of fluence. However, by capturing the near field of the reflected light, an image of the front surface can be inferred through the Fourier transform. In this thesis, the front surface of a target irradiated at 45 degrees with

an intensity of $3\times10^{21}\,\mathrm{W\,cm^{-2}}$ was imaged, showing unexpected spatial variations between the first harmonic reflection and the second harmonic generation.

Role of the Author

The experiments described in this thesis would not have been possible without the team of technical staff, laser scientists and fellow researchers both at the Rutherford Appleton Laboratory, UK, and the J-KAREN-P laser, Kansai Photon Science Institute, Japan. For both experiments, the author was involved in the planning, setting-up and running the experiment and was responsible for the diagnostics presented in this thesis.

The PIC simulations presented in Chapter 5 were performed using the EPOCH code, the Extendible PIC Open Collaboration project developed in the UK. All simulation parameters and input decks were chosen or written by the author and run on the Imperial College supercomputer. The experimental ion data used to benchmark the simulation data in Chapter 5 was collected and analysed by Aodhan McIlvenny of Queen's University, Belfast.

All analysis, both from experimental and simulation results, was performed by the author.

Contents

1 Introduction **1**

1.1 Lasers 1

1.2 Plasma based accelerators 3

1.2.1 Protons for Inertial Confinement Fusion 4

1.2.2 Hadron Therapy 6

1.3 Diagnosing solid density interactions 7

1.4 Thesis outline 8

2 Theory **11**

2.1 Characterisation of a Laser Pulse 11

2.1.1 Mathematical representation of a laser pulse 11

2.1.2 Normalised Vector Potential, $\mathbf{a_0}$ 14

2.2 Plasma Parameters 14

2.2.1 Plasma Frequency 15

2.2.2 The Critical Density 15

2.2.3 Plasma Dispersion Relation 16

2.2.4 Debye Length 18

2.2.5 Single Particle Motion 19

2.2.6 Ponderomotive Force 21

2.2.7 Laser Self-Focusing 22

2.2.8 Ionisation Mechanisms 23

2.3 Overdense Plasma Heating Mechanisms 25

2.3.1 Collisional Heating 25
2.3.2 Resonance Absorption 26
2.3.3 Vacuum Heating 26
2.3.4 J × B Heating 27
2.4 Ion Acceleration Mechanisms 28
2.4.1 Sheath Acceleration 28
2.4.2 Radiation Pressure Acceleration 30
2.4.3 Relativistic Transparency 32
2.4.4 Electron Temperature Scaling 33
2.5 Second Harmonic Generation in a Plasma 33
2.5.1 Coherent Wake Acceleration 34
2.5.2 Relativistic Oscillating Mirror 34
2.5.3 Optical Transition Radiation 35

3 Experimental Methods **39**

3.1 Ti:Sapphire Lasers 39
3.2 FROG 40
3.2.1 Apparatus 40
3.2.2 Retrieval Algorithm 43
3.2.3 Calibration 46
3.2.4 Wigner Transforms 47
3.3 Laser Parameters 48
3.4 Imaging the laser near field 49
3.5 Simulating laser-plasma interactions 49
3.5.1 Resolution 50
3.5.2 Calculating Gamma 51

4 Transmission Through Thin Foils: Experimental Results 53

4.1 Motivation . . . 54

4.2 Set-Up . . . 55

4.2.1 Laser . . . 55

4.2.2 Experimental Layout and Targetry . . . 56

4.3 Diagnostics . . . 57

4.3.1 Transmitted Light Diagnostic . . . 57

4.3.2 Reflected Light Diagnostics . . . 58

4.3.3 Transmitted FROG . . . 59

4.4 Experimental Results from the Transmission Screen . . . 60

4.4.1 Transmitted Beam Spatial Profiles . . . 60

4.4.2 Energy Transmitted . . . 62

4.4.3 Discussion and Summary of Transmitted Light . . . 64

4.5 Experimental Results from the Reflection Analysis . . . 66

4.5.1 Reflected Beam Spatial Profiles . . . 66

4.5.2 Energy Reflected . . . 68

4.5.3 Discussion and Summary of the Reflected Light . . . 69

4.6 Experimental Results from the FROG . . . 70

4.6.1 Discussion and Summary of FROG Results . . . 77

4.7 Conclusion . . . 78

5 Transmission through Thin Foils: Simulations 81

5.1 Electron Density . . . 82

5.2 Transmitted Electric Field . . . 96

5.3 Transition Radiation . . . 102

5.4 FROG traces from Simulations . . . 104

5.5 Particle Diagnostic . . . 107

5.6 Summary . . . 116

6 Reflected light from ultra-intense laser-plasma interactions 119

6.1 Motivation . . . 119

6.2 Experimental Set-Up . . . 121

6.2.1 Laser . . . 121

6.2.2 Experimental Layout . . . 121

6.2.3 Diagnostic: Reflection Screen . . . 122

6.3 Characterisation of the Reflected Beam . . . 123

6.4 Conclusion . . . 129

7 Conclusion and Future Work 131

7.1 Thin foils at normal incidence . . . 131

7.2 Thin foils at oblique incidence . . . 133

7.3 Future Work . . . 134

7.4 Impact on the Field . . . 135

Bibliography 135

List of Tables

4.1 List of experimental parameters used in the Gemini 2017 run. 56

5.1 Parameters for the EPOCH Gemini simulations 82

6.1 List of experimental parameters used in the J-KAREN-P 2018 run. 121

List of Figures

1.1 The set-up of a chirped pulse amplification system, where the stretching and recompression is typically done with reflective gratings. 2

1.2 A proposed layout of fast ignition fusion 6

1.3 The stopping range of ions with respect to particle number for various particles incident on human tissue. 7

2.1 Electric field for a linearly and circularly polarised laser pulse 12

2.2 Electric field reflecting inside a plasma density gradient 18

2.3 Motion of an electron in a linearly or circularly polarised laser field for different values of a_0. 21

2.4 A diagram showing the effect of the laser's electric field on the atomic potential 24

2.5 Vacuum and $\mathbf{J} \times \mathbf{B}$ heating mechanisms in a plamsa 27

2.6 Figure explaining Sheath Acceleration 29

2.7 Radiation pressure acceleration 31

2.8 Angular distribution of radiation for transition radiation 36

2.9 Figure of OTR 37

3.1 Set-up of a FROG autocorrelator 41

3.2 A flow diagram of the FROG retrieval algorithm. 45

3.3 The electric field and the FROG trace of a double pulse. 47

3.4 The difference between the FROG trace and the Wigner transform of a chirped input pulse 47

4.1 Gemini experimental set-up diagram 56

4.2 Calibration plot for the transmission camera in $1\,\omega$ 58

4.3 Spatial profile of the transmitted beam for all target thicknesses, polarisations and harmonics . . . 60

4.4 Spatial profiles of the transmitted beam for targets 2-15 nm on a linear color scale 61

4.5 Spatial profiles of the transmitted beam for targets 25-50 nm on a linear color scale . . . 62

4.6 Transmitted energy with target thickness for both polarisations and harmonics . 63

4.7 Spatial profiles of the reflected beam . . . 67

4.8 Reflected energy with target thickness for both polarisations and harmonics . . . 68

4.9 Spatial images of the experimental and retrieved FROG traces, with the temporal and spectral intensity and phases shown below . . . 72

4.10 Transmitted temporal and spectral envelopes for each target thickness . . . 73

4.11 Transmitted FWHM pulse length with target thickness . . . 74

4.12 Mean temporal chirp with target thickness . . . 75

4.13 Instantaneous frequency with time for different target thickness . . . 76

5.1 Electron density snapshots for 10 and 50 nm targets irradiated by a linearly polarised laser pulse . . . 83

5.2 Electron density snapshots for 10 and 50 nm targets irradiated by a circularly polarised laser pulse . . . 86

5.3 Electron energy distribution with time as a function of target thickness for linear and circular polarisation . . . 89

5.4 Temperature of the hot electron population with time for all targets and polarisations . . . 92

5.5 Electron density with simulation time for all target thicknesses and polarisations 95

5.6 Transmitted electric field in the simulation box . . . 97

5.7 Time taken for targets to become transparent with target thickness . . . 98

5.8 Transmitted energy with target thickness . . . 100

5.9 Transmitted energy for simulations and experiments, 1ω . . . 101

5.10 Electric field and electron density of a 25 and 50 nm target . . . 102

5.11 Electron longitudinal momentum with x position . . . 103

5.12 Wigner transforms of the transmitted electric field . . . 104

5.13 Transmitted pulse length in the simulation . . . 106

5.14 Momentum phase space for a 5 nm target 108

5.15 Proton momentum phase space for a 5 nm target irradiated by a circularly polarised laser pulse 109

5.16 Momentum phase space for a 15 nm target 112

5.17 Momentum phase space for a 50 nm target 113

5.18 Maximum proton energy on-axis found experimentally and through simulations for linear and circularly polarised light 114

6.1 The experimental set-up 122

6.2 Calibration curves of the reflection cameras. 123

6.3 Near and far field of the reflected laser light for a focus scan in the first and second harmonic 124

6.4 Quantity of reflected energy for 1ω and 2ω light at different focus positions . . . 126

6.5 Reflected Energy for a thickness scan 128

Chapter 1

Introduction

1.1 Lasers

Lasers (Light Amplification by Stimulated Emission of Radiation) are coherent electromagnetic beams that exist in either a continuous or pulsed beam format. A laser pulse is spatially and temporally coherent, allowing for it to be focused and for the frequency bandwidth to be tuned. Pulse energy can be varied from microwatts level to multi-petawatts through various amplification techniques, one of which will be presented shortly. The highly tunable nature of lasers, from varying wavelengths, bandwidths, pulse lengths and energy, makes them an interesting tool for use in multiple sectors [1]. In particular, they are one of the mechanisms of creating plasmas for research in the scientific community.

Lasers are particularly interesting in this field of research as the electromagnetic fields can be as strong as, and even exceed, the atomic binding energies of molecules. Thus, as the laser interacts with a material the properties of each are changed. The material may experience effects such as change in refractive index, whereas the laser may experience changes in phase and wavelength. Such interactions are the cause of numerous effects such as self-phase modulation, self focusing and high harmonic generation and are the foundation of the field of non-linear optics. If the electromagnetic fields of the laser exceed the binding energy of the electrons in the atoms, the material is rapidly ionised and becomes a plasma. Once in a plasma state, the material is able

to absorb energy from the laser pulse through a variety of mechanisms which leads to many interesting effects; these will be discussed shortly.

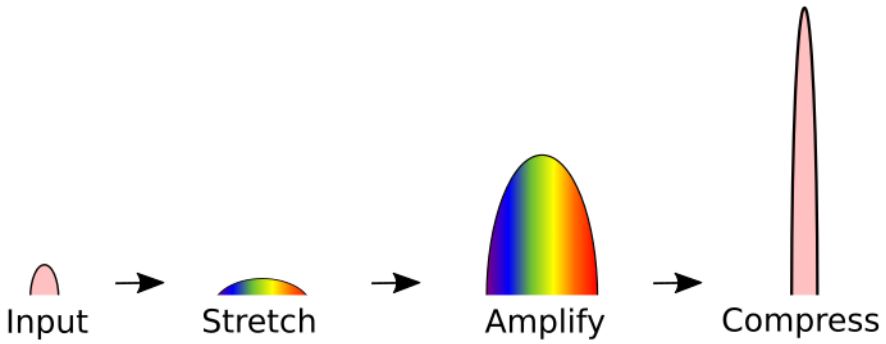


Figure 1.1: The set-up of a chirped pulse amplification system, where the stretching and re-compression is typically done with reflective gratings.

For a laser-plasma interaction, a primary characteristic used to describe the laser is the intensity achievable. This defines the type of interaction occurring, as for intensities above $10^{18}\,\mathrm{W\,cm^{-2}}$ the interaction is considered relativistic. Previously, laser amplification was limited by damage in the amplification chain due to laser self-focussing and self modulation, which also significantly affected the beam spatial quality. Since it's invention in the 1980's however, high energy short pulses are achievable thanks to the development of chirped pulse amplification (CPA) which was pioneered by Donna Strickland and Gerard Mourou [2]. CPA consists of stretching the initial short laser pulse of large bandwidth both spectrally and temporally by diffraction gratings so that each frequency sees the gain medium independently. The chirped pulse then goes through the gain medium, and if this gain medium has a bandwidth similar to the bandwidth of the laser pulse, then each frequency will be amplified by the same amount. This means that the medium must be made up of a material that has a lattice or crystal structure such that the energy levels of the atoms span the range of the laser pulse frequency. The laser pulse photons then stimulate photon emission from the excited atoms of this gain material and hence the flux of photons of a given frequency is increased. To achieve amplification the gain medium must be in population inversion. Once the gain medium is depleted, the positively chirped pulse is then recompressed by reversing the stretching mechanism. A schematic of this system is shown in Figure 1.1. Thus, high intensities can be attained by focussing multi-joule, ultrashort pulses down to micron level spot sizes.

1.2 Plasma based accelerators

Charged particles have traditionally been accelerated using large electromagnetic fields. Initially done using linear or circular accelerators, such technology comes with huge financial costs as well as infrastructure and technical limitations. In these accelerators, particle energy is limited due to the accelerating gradient of the RF cavities. The Kilpatrick limit of $\approx 195\,\mathrm{MV/m}\,\nu[\mathrm{GHz}]^{-1/2}$ [3] defines the maximum accelerating gradient possible before breakdown on the cavity walls occurs. For circular designs, the particle energies are proportional to $1/r^2$, where r is the radius of curvature of the accelerator. As the energies are limited by losses from for example synchrotron radiation, to achieve higher particle energies longer or larger diameter accelerators are needed, both of which come with large financial costs.

In comparison, plasmas are a medium well suited for particle acceleration due to their already ionised state, meaning there are no physical limitations to the accelerating gradients achievable and no risk of breakdown. A plasma can be generated by the direct irradiation of a target by a laser pulse. Particles are then accelerated by large electric fields induced in the plasma or through radiation pressure, with the resultant energies related to the intensity of the laser and the acceleration mechanism used. Additionally, different acceleration mechanisms generate particle beams with different properties, allowing for further tuning of the energy spectrum output. For electron acceleration, underdense gas and a laser wakefield is generally used to achieve high particle energies [4]. For ions, which includes protons up to high Z nuclei, overdense target interactions are usually used. While the maximum particle energy obtainable from a laser based accelerator has not matched the record achieved by conventional accelerators, it has many advantages over it's conventional counterpart. Smaller and more compact, laser particle accelerators occupy significantly smaller footprints than the linear or circular accelerators, reaching muliple 10's of meters long (Linac2, CERN) or 27 km in circumference (Large Hadron Collider) respectively. Additionally, with multiple different acceleration mechanisms possible for a single laser system, the species of particle accelerated could be changed by simply changing the material of the target or tuning of the laser parameters. Finally, lasers are now developing the ability to run at kilojoule energies and high repetition rates [5]. For example, the BELLA

laser at Lawrence Berkeley National Laboratory can reach petawatt levels at a repetition rate of 1 Hz.

Two uses of laser plasma based particle accelerators are given below.

1.2.1 Protons for Inertial Confinement Fusion

Inertial Confinement Fusion (ICF) is a potential source of unlimited green energy that has been researched theoretically and experimentally for decades [6] [7] [8]. It consists of igniting fusion in a hot spot in a small spherical fuel pellet, typically made of deuterium and tritium (DT), with the use of high power laser pulses (1.5 MJ in 7.5 ns [9]). The burn wave propagates from the hotspot radially outwards through alpha particle heating and ignites the remaining fuel. This is done by either directly irradiating the pellet with laser light in a process called direct drive [7], or indirectly by x-ray formation in a hohlraum called indirect drive.

In direct drive [7], multiple shaped laser pulses are incident spherically symmetrically onto the cryogenic fuel pellet that contains a few milligrams of fuel. The plastic ablator layer surrounding the fuel heats and explodes outwards causing a resultant force that drives fuel implosion. As the shock wave reaches the centre, the imploding material stagnates and the kinetic energy is transformed into internal energy. The centre of the pellet is made up of DT gas which is of lower density. Therefore there is a large rise in entropy which results in a large temperature increase. If the conditions are correct a hot spot is created at the centre, and if the Lawson Criterion is met ignition is reached; a burn wave propagates from the hotspot and ignites the fuel causing it to explode. The main issue of direct drive lies in it requiring a homogeneous spread of energy over the whole spherical surface where any variation from equilibrium will produce instabilities and hence limit the efficiency of the reaction.

Indirect drive [10] is currently the more researched experimental method which consists of placing the pellet inside a hollow cylinder coated with gold called the hohlraum [9]. The laser is shone into the hohlraum through the extremities and the energy is absorbed by the walls and re-radiated as x-rays. The x-rays lack coherence and thus produce a more uniform isotropic

radiation that reduces instabilities. The x-rays are then incident on the pellet and ignite fusion in a similar manner to direct drive. However, the hohlraum's higher capsule implosion efficiency only partially compensates for the energy loss in the walls.

With the lack of success of the National Ignition Facility (NIF), ICF's flagship research laboratory, at igniting energy-producing fusion, a previously considered method was trialled using two different laser pulses [8]. Fast ignition consists of two pulses, the first used to compress the fuel and the second to heat the core, igniting fusion. This would greatly reduce the energy requirements from the driving laser and improve efficiency. It would also enable scientists to decouple the heating and compressing stages which would then reduce instabilities.

An alternative way to transport heat to the hot spot is through energetic protons which would deposit their energy locally through the Bragg peak (See Section 1.2.2). The protons would be produced by the laser irradiation of a thin foil placed in a focusing cone whose tip would be the centre of the fuel pellet, and hence the hot spot. A suggested layout is shown in Figure 1.2. A preliminary investigation into the energy, intensity and spatial structure requirements of a driving proton beam was done via simulations by Roth *et al* [11]. They concluded this would be a feasible option once proton energies of upto 25 MeV could be produced with an energy efficiency of above 10%. Current experiments have achieved efficiencies of around 2%, with the efficiency strongly dependent on the proton beam energy spectrum [11] [12].

Once achieved, fast ignition could provide the world with a sustainable and clean energy source thus limiting the effect of energy production on climate change. The deuterium fuel can be sampled easily from sea water and tritium can be produced on the chamber walls from neutron bombardment of lithium in a process called tritium breeding; this technology will be tested and implemented in future magnetic confinement reactors such as ITER [13]. Apart from just being a green energy source, it is also more compact and can have a varying repetition rate to match energy demand.

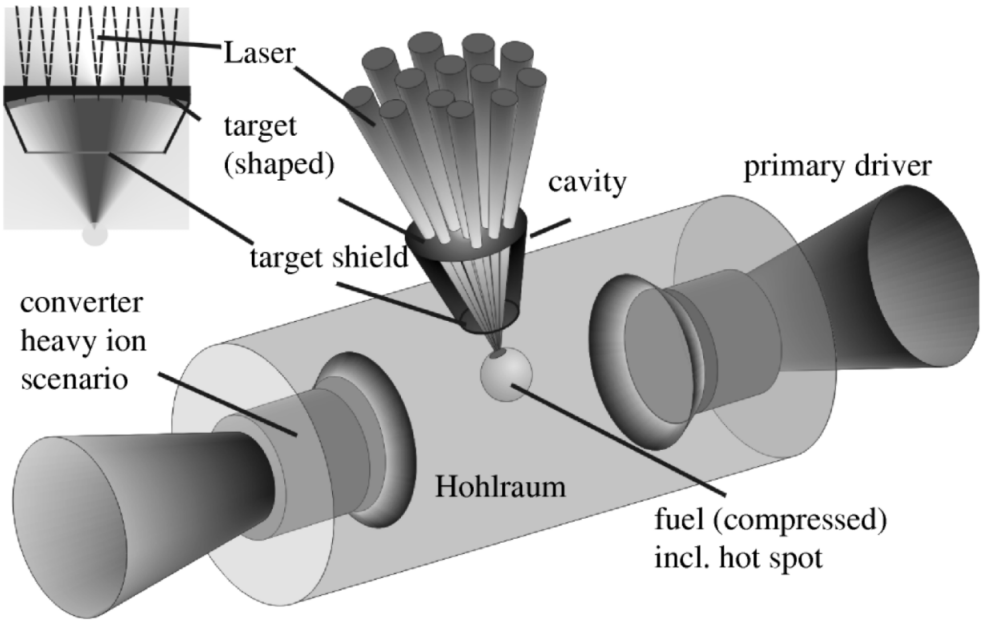


Figure 1.2: A proposed layout of fast ignition fusion (diagram not to scale) [11]

1.2.2 Hadron Therapy

Protons and heavier ions have long been used in cancer therapy due to their unique characteristic way of losing energy [14]. An energetic proton loses small amounts of energy through ionisation of electrons as it propagates through matter, before losing the majority of its energy in a very short distance through collisions with the nuclei. In comparison, photons lose the majority of their energy near the surface of the matter, with a decreasing rate of energy loss for further propagation. This is shown in Figure 1.3 where the the rate of energy loss per distance is shown for different particles. The Bragg peak, which can be calculated from the energy of the ion and density of the material using the open source software SRIM (Stopping Range of Ions in Matter) [15], allows clinicians to deposit ionising radiation into the tumour with minimal damage to the surrounding tissue. In order to access all parts in the human body, a maximum value of 250 MeV protons is required [16] [17].

Alternative methods consisted of using x-rays which entailed significant damage to healthy tissue surrounding the tumour. This side effect affects patients recovery time and the ability to treat all tumours. To date most hadron therapy machines source their protons from cyclotrons,

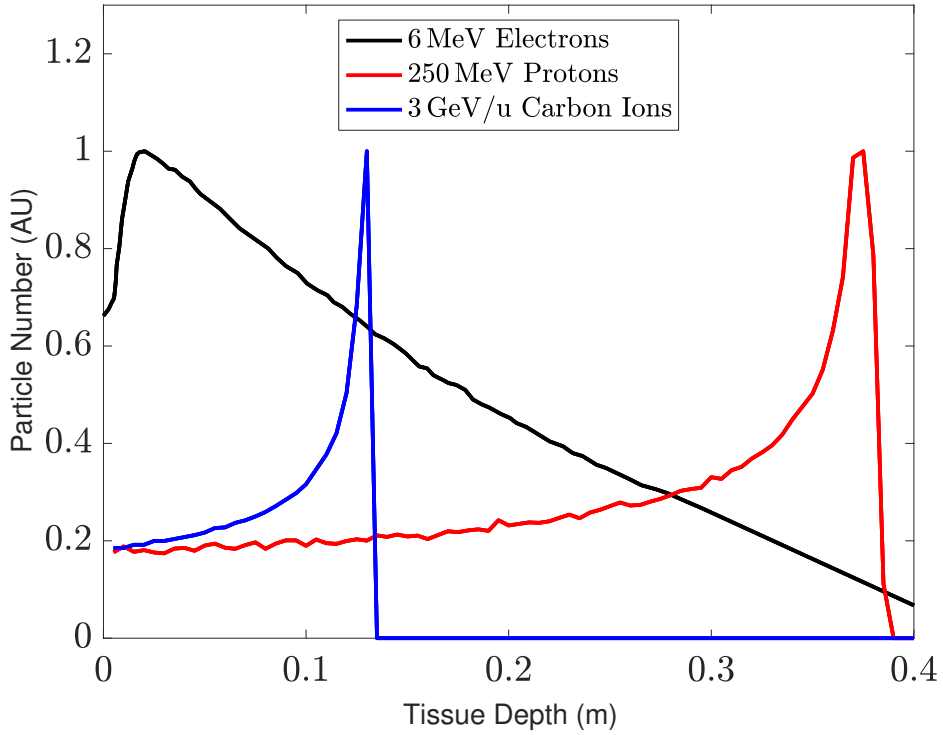


Figure 1.3: The stopping range of ions with respect to particle number for various particles incident on human tissue. The proton and carbon ion spectrums were generated using the open source software TRIM [15]. The electron data was taken from *Sardari et al* [18].

due to the reliability, emittance and mono-energetic features of the beam produced. However cyclotrons are inflexible regarding the energy range and ion species deliverable. Thus, a combination of a laser front end, capable of accelerating a variety of ions to a range of energies, and a magnetic gantry might be the machine of the future. In order to target all possible tumours, a laser front end must still be optimised, with many issues such as proton energy requirements, high repetition rate, monoenergetic beam and beam divergence still under development.

1.3 Diagnosing solid density interactions

In order to continue improving the maximum ion energies achievable, a full understanding of the various acceleration mechanisms and interaction dynamics must be obtained. Given most applications require ion sources that are delivered through overdense laser-plasma interactions, a full evolution of the occurring particle motion is impossible. Techniques such as higher

frequency interferometry are able to probe deeper into the plasma. However these are not able to provide a full picture of the physics occurring. Understanding the particle acceleration mechanism, it's temporal evolution and the method of energy transfer from laser pulse to particles is therefore of crucial importance to researchers seeking to optimise ion energies.

Traditionally, experiments exploring optimised ion acceleration are diagnosed with particle detectors, with the maximum particle energy achieved, the spectrum and flux a measure of success. The experiments are also typically probed transversely with higher frequency lasers to gain information such as density scale length on the front and rear surface. While this helps gain information on particle motion, extremely high densities cause the target to remain overdense for the vast majority of practically useable wavelengths. Thus, alternative diagnostics must be used to gain further information on the interaction.

1.4 Thesis outline

This thesis demonstrates how optical diagnostics, in particular charicterisation of the reflected and transmitted light can be used to gain information on the laser-plasma interaction occurring. Chapter 2 explains the necessary theoretical background, including an introduction to lasers, plasmas and the various ion aceleration mechanisms possible. Chapter 3 introduces the experimental knowledge necessary to understand the body of this thesis, including a detailed description of the FROG (See Section 3.2.1).

The first of the results chapters, Chapter 4, presents experimental data taken on the Gemini laser, RAL UK, in 2017. The experiment consisted of irradiating nanometer scale thin-foils and observing the differences in transmitted and reflected light for both the laser fundamental and second harmonic. The transition between radiation pressure and relativistic transparency acceleration mechanisms was seen, as well as interesting spectral properties of the transmitted light. Chapter 5 presents numerical simulations of the interactions occuring in Chapter 4, including additional insight into the temporal evolution of the electron density and the target's transition into transparency. Chapter 6 presents results from an experimental campaign on the

J-KAREN-P laser in Japan, where the properties of the target's front surface were explored by examining the spatial paterns of the reflected light. The beam patterns showed variations in the reflection and formation regions of the different harmonics. Finally, Chapter 7 summarises the work presented in this thesis and introduces the future avenues of research of the field.

Chapter 2

Theory

2.1 Characterisation of a Laser Pulse

2.1.1 Mathematical representation of a laser pulse

A laser pulse is an electromagnetic pulse that can be fully defined by it's temporal intensity, $I(t)$, and phase, $\phi(t)$. A pulse propagating in the $\hat{z}$ direction can be described mathematically as:

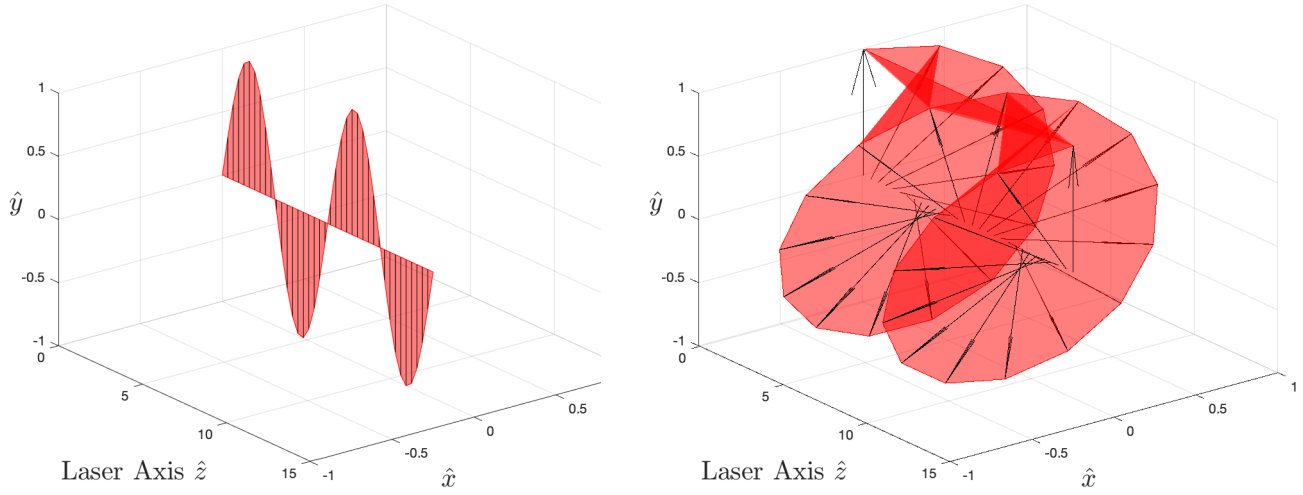
$$\mathbf{E}(z,t) = \frac{1}{2}\mathbf{E}_0 \exp(i[kz - \omega t + \Phi(t)]) + c.c. \tag{2.1}$$

where $c.c.$ indicates the complex conjugate and ω, k and Φ the frequency, wavenumber and phase of the pulse respectively. A laser pulse can be polarised, where the electric and magnetic fields define an angle and magnitude of oscillation relative to the coordinate system. The magnitude of the electric field can be separated into it's orthogonal constituents $|\mathbf{E}_0| = \sqrt{E_x^2 + E_y^2}$, where each has a respective magnitude and phase, dependent on polarisation: $E_{x,y} = A\,|E_0|\,e^{i\phi_{x,y}}$. For a fixed peak amplitude E_0, $A = 1$ for linear polarisation and $A = \frac{1}{\sqrt{2}}$ for circular polarisation. For linear and circular polarisation respectively, the laser electric field can be defined as:

$$\mathbf{E}_l(t) = \frac{1}{2}E_0 \exp(i[kz - \omega t + \phi(t)])\hat{\mathbf{x}} + c.c. \tag{2.2}$$

$$\begin{aligned}\mathbf{E}_c(t) =& \frac{1}{2}E_0\left(\exp[i(kz-\omega t+\phi(t))]\hat{\mathbf{x}}+\exp[i(kz-\omega t+\phi(t+\pi/2))]\hat{\mathbf{y}}\right)\\ &+ c.c.\end{aligned} \tag{2.3}$$

Figure 2.1 shows the electric field of a linearly and circularly polarised pulse.



(a) Linear Polarisation (b) Circular Polarisation

Figure 2.1: Electric field for a linearly and circularly polarised laser pulse. The electric field is shown in red, with black arrows indicating the instantaneous direction of oscillation.

Described through its intensity, $I(t)$, and phase, $\phi(t)$, in the temporal domain, a laser pulse can also be described through its spectrum $S(\omega)$ and spectral phase $\varphi(\omega)$ in the frequency domain. These properties are linked through the Fourier Transforms:

$$E(t) = \frac{1}{2\pi}\int_{-\infty}^{\infty}\tilde{E}(\omega)\exp(i\omega t)d\omega \tag{2.4}$$

$$\tilde{E}(\omega) = \int_{-\infty}^{\infty}E(t)\exp(-i\omega t)dt \tag{2.5}$$

where the tilde represents the Fourier Transform. The spectrum and spectral phase are related by:

$$\tilde{E}(\omega) = \sqrt{S(\omega)}\exp(-i\varphi(\omega)) \tag{2.6}$$

where the spectral phase $\varphi(\omega)$ can be expanded through a Taylor series:

$$\varphi(\omega) = \varphi_0 + (\omega - \omega_0)\,\varphi_1 + \frac{(\omega - \omega_0)^2}{2}\,\varphi_2 + \ ... \tag{2.7}$$

Here, each order corresponds to different phase variations. The zeroth order represents the absolute phase and relates the phase of the carrier wave to the envelope. While important for ultra-short single cycle pulses, for multi-cycle pulses such as those used in this thesis, the term has almost no effect on the overall pulse shape. The first order phase corresponds to a shift in time or frequency, i.e. $E(t-\tau)$ Fourier Transforms to $\tilde{E}(\omega)\exp(-i\omega\tau)$ [19]. In a laboratory, a shift in time can be easily measured with interferometry, whereas a shift in frequency can be measured with a spectrometer. The second order phase corresponds to a linear chirp, or a linear change of frequency with time. The laser pulse can be either positively chirped (increasing frequency with time) or negatively chirped (the opposite). Higher order phases give more complex pulses with additional distortions and, along with linear chirp, are only distinguishable on diagnostics such as a FROG, described in Section 3.2.1. The second order phase term is of particular interest in this thesis, and will be discussed more in Chapters 4 and 5.

Dispersion through a medium

Materials have refractive indexes that vary with frequency, $\eta(\omega)$, thus upon propagating through a material a laser pulse will experience Group Delay Dispersion (GDD). Each frequency component, travelling at different group and phase velocities depending on the refractive index of the material, are attenuated differently depending on the absorption coefficient $\alpha(\omega)$. The effect is generally dealt with in the frequency domain as it is more intuitive: assuming a linearly dispersive medium of length L, an initial laser pulse E_{in} is affected in the following manner:

$$\tilde{E}_{out}(\omega) = \tilde{E}_{in}(\omega)\,\exp\left(-\alpha(\omega)\frac{L}{2}\right)\,\exp\left(i\,\eta(\omega)\frac{\omega}{c}L\right) \tag{2.8}$$

Thus two modifications are occurring: in the first term absorption is changing the spectrum, as

shown in Equation 2.9, and in the second dispersion is changing the spectral phase, as shown in Equation 2.10. This can be shown mathematically:

$$S_{out}(\omega) = S_{in}(\omega)\ \exp(-\alpha(\omega)L) \tag{2.9}$$

$$\varphi_{out}(\omega) = \varphi_{in}(\omega) + i\,\eta(\omega)\frac{\omega}{c}L \tag{2.10}$$

2.1.2 Normalised Vector Potential, $\mathbf{a_0}$

Laser pulses of varying energy and wavelength can be compared through the dimensionless parameter of a_0, known as the normalised vector potential and given by:

$$\mathbf{a}_0 = \frac{e\mathbf{E}_0}{m\omega c} \tag{2.11}$$

It can be related to the intensity of the laser pulse by taking the time average of the Poynting vector $\mathbf{S}$:

$$I = \langle \mathbf{S} \rangle = \frac{\alpha}{2}\epsilon_0 c E_0^2 = \frac{2\alpha\pi^2\epsilon_0 c^5 m^2}{e^2}\left(\frac{a_0^2}{\lambda^2}\right) \tag{2.12}$$

where $\alpha = 1, 2$ for linear or circular polarisation respectively. Hence, $a_0 \approx 0.855(I\lambda^2)^{1/2}$ where I is given in 10^{18} W cm^{-2} and λ is given in µm. This parameter is important as it describes the response of an electron to an electromagnetic field, and will be addressed in more detail in Section 2.2.5. Physically, a_0 is a measure of how strong the laser-plasma interaction is, as for $a_0 > 1$ the motion of an electron becomes relativistic.

2.2 Plasma Parameters

A plasma can be described as "a quasi neutral gas of charged and neutral particles that exhibit collective behaviour" [20]. All particles interact with each other either through long range electric and magnetic fields or through collisions, which occur due to localised charge neutrality

violations or particle motion. The term "collective behaviour" is used to describe how the particles in the plasma interact as a whole, where their motion is governed by parameters described below.

2.2.1 Plasma Frequency

Consider a neutral plasma: if an electron is displaced from it's initial position, a restoring electric field will oppose the displacement. Once released, the electron will be accelerated back to it's initial position and over shoot due to inertia. Thus, the electrons in a plasma oscillate at a characteristic frequency of ω_p, which is given by:

$$w_p = \sqrt{\frac{e^2 n_e}{m_e \epsilon_0}} \tag{2.13}$$

where e is the elementary charge, n_e is the electron density, m_e the electron mass and ϵ_0 the vacuum permittivity. The plasma frequency is one of the factors that defines the opacity limit of the plasma (the other being collisions) and measures the ability of electrons to respond to external electromagnetic fields. For an electromagnetic wave of frequency $\omega_l < \omega_p$, the wavenumber k becomes imaginary (see section 2.2.3) and thus the incident wave is reflected and is not able to propagate through the plasma.

2.2.2 The Critical Density

Equation 2.13 can be rearranged to define the critical density, the minimum plasma density required to reflect a laser pulse of frequency ω_l. This occurs when the laser frequency ω_l is equal to the plasma frequency ω_p and is given by:

$$n_{crit} = \frac{\omega_l^2 m_e \epsilon_0}{e^2} \tag{2.14}$$

In a relativistic regime the mass of the electron must be modified by the Lorentz factor to $m_e^{rel} = \gamma\, m_e$. Therefore the critical density becomes:

$$n_{crit}^{rel} = \frac{\langle\gamma\rangle\, \omega_l^2 m_e \epsilon_0}{e^2} \tag{2.15}$$

For relativistic laser pulses, where $a_0 \geq 1$, a higher critical density is required. Additionally, the time averaged γ factor, $\langle\gamma\rangle$, can be written in terms of the normalised vector potential, a_0:

$$\langle\gamma\rangle = \begin{cases} \sqrt{1 + a_0^2} & \text{for circular polarisation.} \\ \sqrt{1 + \frac{a_0^2}{2}} & \text{for linear polarisation} \end{cases} \tag{2.16}$$

thus showing the relativistic critical density also has a polarisation dependence.

2.2.3 Plasma Dispersion Relation

An electromagnetic pulse propagating through vacuum has velocity c related to it's wavevector k and frequency ω by $\omega = ck$. Once in a plasma medium, the pulse is affected by dispersion. The dispersion relation defines how the pulse propagates and can be calculated from the following Maxwell's equations:

$$\nabla \times \mathbf{B} = \mu_0 \mathbf{j} + \frac{1}{c^2}\frac{\partial \mathbf{E}}{\partial t} \tag{2.17}$$

$$\nabla \times \mathbf{E} = -\frac{\partial \mathbf{B}}{\partial t} \tag{2.18}$$

By taking the time derivative of the first equation, the curl of the second, and substituting for vector identities, the two equations above can be rearranged into the wave equation:

$$\nabla^2 \mathbf{E} = \mu_0 \frac{\partial \mathbf{j}}{\partial t} + \frac{1}{c^2}\frac{\partial^2 \mathbf{E}}{\partial t^2} \tag{2.19}$$

This assumes a neutral, semi-infinite plasma such that $\nabla \cdot \mathbf{E} = 0$. The current term $\mathbf{j}$ can be assumed to come entirely from the motion of the electrons as ions are assumed to remain

stationary over the time scale of interest. Hence $\mathbf{j} = -en_e\mathbf{v}_e$, where n_e is the electrons density, each with velocity $\mathbf{v}_e$. An equation for the velocity can be found using the Lorentz equation and assuming a non-relativistic interaction such that $m_e\dfrac{\partial(\mathbf{v}_e)}{\partial t} = e\mathbf{E}$. Thus, the current term becomes:

$$\mathbf{j} = \frac{e^2 n_e \mathbf{E}}{i\omega_l m_e} \tag{2.20}$$

Substituting equation 2.20 into equation 2.19 and by using standard vector calculus identities for plane waves: $\nabla \rightarrow ik$ and $\partial_t \rightarrow -i\omega$, the dispersion relation can given by:

$$w_l^2 = w_p^2 + c^2 k_l^2 \tag{2.21}$$

where ω_l is the laser frequency, ω_p the plasma frequency and k_l the laser wavenumber.

For the case of a laser pulse incident on a plasma boundary, Equation 2.21 shows that when $\omega_p > \omega_l$ the wavenumber becomes imaginary. The electric field decays exponentially to a distance known as the skin depth, l_s, given by:

$$l_s = \frac{c}{\sqrt{\gamma}\,\omega_p} \tag{2.22}$$

The skin depth is an important parameter in overdense interactions as it defines the reflecting region of the laser pulse in the plasma. Hence has a large effect on the quantity of energy absorbed. For a laser pulse of wavelength of 800 nm incident into a plasma of electron density 1.19×10^{30} m^{-3}, the skin depth is found to be approximately 5 nm.

For non-zero angles of incidence, the dispersion relation for an electromagnetic wave in a plasma can be rewritten as:

$$\frac{\omega_l}{c}\,\epsilon = k^2 \tag{2.23}$$

where ϵ is the permittivity (dielectric function) of the plasma and k is the wave vector of the laser pulse. Equation 2.23 becomes important when considering a laser pulse obliquely incident onto a plasma with a density gradient. Assuming a planar density gradient perpendicular to the target's surface and in the $\hat{z}$ direction, the dielectric constant is a function of z only, i.e $\epsilon(z)$.

Thus, by assuming a laser pulse propagating into the plasma along the z-y plane of incidence,

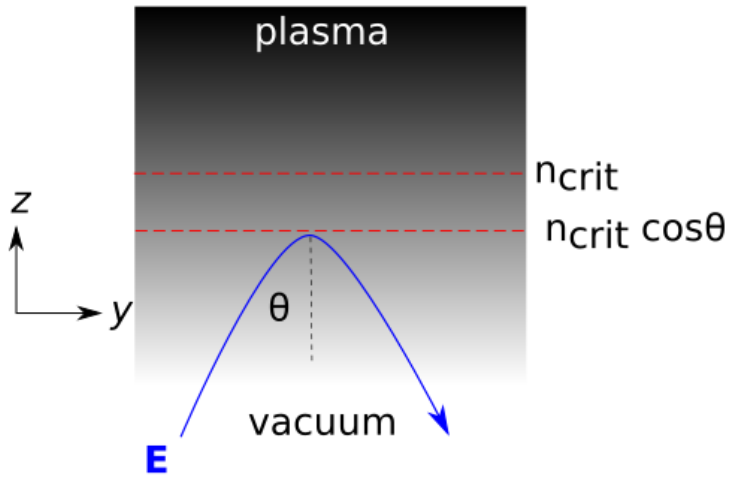


Figure 2.2: Electric field, **E**, reflecting inside a plasma density gradient

and polarised in the $\hat{x}$ direction, $E_x = \mathbf{E}(z)\exp\left(\frac{i\omega y \sin\theta}{c}\right)$, the wave vector of the pulse must be conserved, such that $k_y = (w/c)\sin\theta$ and $k_z = (w/c)\cos\theta$. The wave equation for the electric field can then be written as:

$$\frac{\mathrm{d}E(z)}{\mathrm{d}z^2} + \frac{\omega^2}{c^2}\left(\epsilon(z) - \sin^2\theta\right)E(z) = 0 \tag{2.24}$$

This has solution $\epsilon(z) = \sin^2\theta$, and as $\epsilon(z) = 1 - \omega_p^2(z)/\omega^2$, reflection occurs when $\omega_p = \omega\cos\theta$ or $n_e = n_{crit}\cos^2\theta$.

2.2.4 Debye Length

Macroscopically, a plasma is defined as neutral. Therefore, when a test charge is placed inside a cold plasma, the surrounding particles move to screen the charge such that at a distance much greater than the particle separation, no electric field is felt. However, as the plasma has some thermal energy, particles on the very edge of the field are able to escape the test charge's potential well. This occurs when the particle's thermal energy, $k_B T_e$, is equal to the potential energy. The spatial scale length of this phenomenon is known as the Debye length, λ_D, where

particles beyond this distance no longer feel the force of the test charge's field. It is given by:

$$\lambda_D = \sqrt{\frac{\epsilon_0 k_B T_e}{n_0 e^2}} \tag{2.25}$$

where k_B is the Boltzmann constant, T_e the electron temperature, e the charge of an electron and n_e the electron density, assumed to follow a Boltzmann distribution given by $n_e = n_0 e^{\frac{e\phi}{k_B T_e}}$. Thus, for distances longer than the Debye length, the charge is effectively screened, and particles in a plasma only feel the force of those within a sphere of radius the Debye length.

2.2.5 Single Particle Motion

For a laser pulse propagating in the $\hat{\mathbf{z}}$ direction, the force on an electron in the laser field is defined by the Lorentz force, given by:

$$\mathbf{F} = \frac{d\mathbf{p}}{dt} = -e(\mathbf{E} + \mathbf{v} \times \mathbf{B}) \tag{2.26}$$

By assuming a short time scale such that the background ion population remains stationary, for a linearly polarised pulse with electric field $\mathbf{E} = E_x \cos(kz - wt)\hat{\mathbf{x}}$ and magnetic field $\mathbf{B} = B_y \cos(kz - wt)\hat{\mathbf{y}}$, the equations of motion of an non-relativistic electron are given by:

$$\begin{aligned} m\dot{v}_x &= -eE_x \cos(kz - \omega t) + eB_y v_z \cos(kz - \omega t) \\ m\dot{v}_y &= 0 \\ m\dot{v}_z &= ev_x B_y \cos(kz - \omega t) \end{aligned} \tag{2.27}$$

where $E_x = cB_y$. Now assuming an electron initially at rest, such that $v_x = v_y = v_z = 0$, and integrating the above equations, the velocity of the electron can be described by:

$$\begin{aligned} v_x &= a_0 c \sin(kz - wt) \\ v_y &= 0 \\ v_z &= \frac{a_0^2 c}{2} \sin^2(kz - \omega t) \end{aligned} \tag{2.28}$$

Equations 2.28 show that an electron irradiated by a linearly polarised laser pulse has a longitudinal velocity proportional to a_0^2 and transverse velocity proportional to a_0. The motion of the electron is therefore:

$$\begin{aligned} x &= \frac{a_0 c}{\omega}\left(\cos(kz - wt) - 1\right) \\ y &= 0 \\ z &= \frac{a_0^2 c}{4}t - \frac{a_0^2 c}{8}\sin 2(kz - \omega t) \end{aligned} \tag{2.29}$$

Thus, an electron irradiated by a linearly polarised laser pulse experiences a constant drift velocity, $v_d = \frac{a_0^2 c}{4}$, in the direction of laser propagation, where $v_z = \frac{1}{2}v_x^2$. The electron also traces a "figure of eight" motion in the transverse direction, as shown in Figure 2.3a.

In comparison, for a circularly polarised pulse, with electric field $\mathbf{E} = E_x \cos(kz - wt)\hat{\mathbf{x}} + E_y \sin(kz - wt)\hat{\mathbf{y}}$ and magnetic field $\mathbf{B} = B_x \sin(kz - wt)\hat{\mathbf{x}} + B_y \cos(kz - wt)\hat{\mathbf{y}}$, the equations of motion of the electron are given by:

$$\begin{aligned} m\dot{v}_x &= -eE_x \cos(kz - \omega t) + eB_y v_z \cos(kz - \omega t) \\ m\dot{v}_y &= -eE_y \sin(kz - \omega t) + eB_x v_z \sin(kz - \omega t) \\ m\dot{v}_z &= -eB_y v_x \cos(kz - \omega t) + eB_x v_y \sin(kz - \omega t) \end{aligned} \tag{2.30}$$

with velocities:

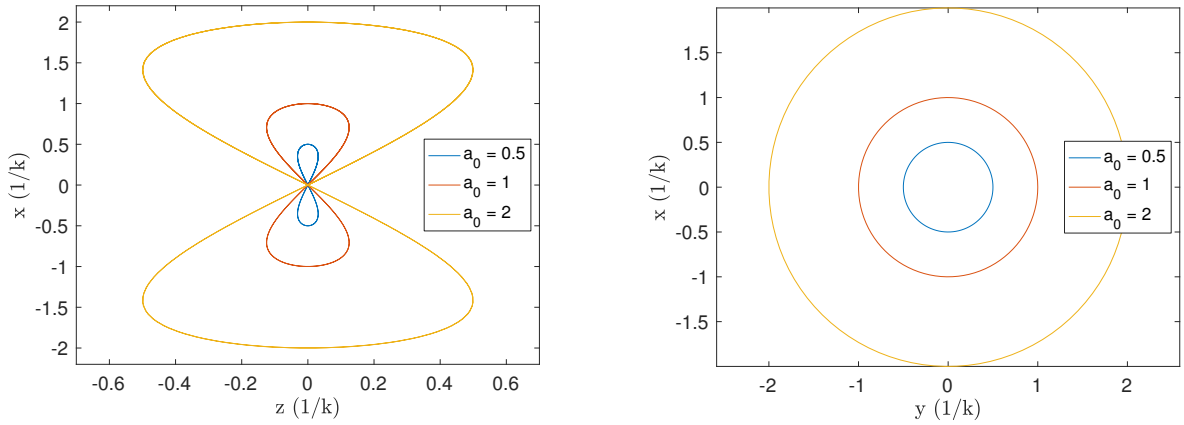
$$\begin{aligned} v_x &= a_0 c \sin(kz - wt) \\ v_y &= a_0 c \cos(kz - wt) \\ v_z &= C_1 \end{aligned} \tag{2.31}$$

where C_1 is a constant of integration. Thus the electron traces a circle in the transverse $\hat{\mathbf{x}} - \hat{\mathbf{y}}$ plane with radius proportional to a_0, and a constant drift velocity, $v_{drift} = C_1$, as shown in Figure 2.3b. The motion of the electron is then:

$$\begin{aligned} x &= \frac{a_0 c}{\omega}\left(\cos(kz - wt) - 1\right) \\ y &= \frac{a_0 c}{\omega}\left(1 - \sin(kz - wt)\right) \\ z &= C_1 t + C_2 \end{aligned} \tag{2.32}$$

Thus, an electron irradiated by a circularly polarised laser pulse experiences a constant drift velocity, $v_d = C_1$, in the direction of laser propagation, as well as tracing a circular motion in the transverse direction. Note that as the laser intensity, and hence a_0 increases, the transverse and longitudinal momentum of electrons in a linearly polarised field increases, whereas for circular polarisation the drift velocity is independent of laser a_0.

These differences in particle motion due to laser polarisation are important when considering both the mechanisms and rate of target heating in laser-plasma interactions, in particular for overdense targets, as will be discussed in later sections. Animations of the above are available in [21].



(a) Electron motion in the drift frame due to linearly polarised light for different a_0.

(b) Electron motion in the drift frame due to circularly polarised light for different a_0.

Figure 2.3: Motion of an electron in a linearly or circularly polarised laser field for different values of a_0.

2.2.6 Ponderomotive Force

Electrons in a plasma experience the ponderomotive force, F_p. Unlike a plane wave, a laser pulse has a transverse gradient in intensity which causes the electrons in the centre of the beam to oscillate and move from regions of high intensity to regions of lower intensity. Once displaced, the magnitude of the restoring force in the region of lower intensity is smaller, and hence the electrons never return to their initial position. The ponderomotive force is given by:

$$\mathbf{F}_p = m\left\langle \frac{\partial \mathbf{v}}{\partial t} \right\rangle = -\frac{1}{2}mc^2\nabla\langle \mathbf{a}_0^2 \rangle \tag{2.33}$$

where $\langle \mathbf{a}_0^2 \rangle$ is the time averaged normalised vector potential. It acts along the gradient of electric and magnetic fields of the laser pulse and is proportional to the gradient of it's intensity, i.e $F_p \propto \nabla\langle E_0^2 \rangle \propto \nabla\langle I \rangle$. It has an associated ponderomotive potential, U_p, given by:

$$U_p = \frac{1}{2}mc^2 a_0^2 \tag{2.34}$$

Thus, the ponderomotive force causes electron density gradients in the plasma that induce effects such as laser self focusing.

2.2.7 Laser Self-Focusing

The convergence or divergence of a laser pulse can be modified in the underdense plasma through self-focusing. Due to relativistic or ponderomotive effects, the laser pulse experiences a variation in transverse refractive index, causing a change in localised phase velocity. This leads to a curvature in the wave front causing a focussing or defocussing effect.

As a_0 is proportional to the electric field of the laser, the electrons in the centre of the laser pulse experience a greater mass change (as a higher a_0) which changes the plasma frequency throughout the laser spot. The refractive index of a plasma η can be given by:

$$\eta \quad = \quad \sqrt{1 - \frac{\omega_p^2}{\gamma\omega_l^2}} \quad = \quad \sqrt{1 - \frac{n_e}{n_{crit}^{rel}}} \tag{2.35}$$

where ω_p is the plasma frequency, ω_l is the laser frequency, and γ is the relativistic gamma. The second part of Equation 2.35 shows that self-focusing is also possible in laser pulses with $a_0 < 1$ due to the ponderomotive force, F_p. As F_p is proportional to the gradient of the electric field squared, $F_p \propto \nabla E^2$, in the most intense part of the beam, the electrons are pushed out, causing a local change in electron density, n_e. Thus, the refractive index is locally increased, causing wavefront deformations that focuses the laser beam.

Relativistic self-focusing occurs above a threshold power, P_t, which is given by [22]:

$$P_t = \frac{4\pi\epsilon_0 m_e^2 c^5 \omega_l^2}{e^2 \omega_p^2} = 17.3 \left(\frac{\omega_l^2}{\omega_p^2}\right) \; [\,\mathrm{GW}\,] \tag{2.36}$$

As the laser pulse self-focuses, the instantaneous intensity increases as well as the rate of energy depletion. Thus, the pulse loses energy and the self-focussing effect stops. To guide a laser pulse through an underdense channel, a balance between diffraction and self-focusing must be reached. Experimental results have measured beam guiding through a plasma [23] [24], and this phenomena can also be exploited to enhance laser intensity on target [25].

2.2.8 Ionisation Mechanisms

Energy transfer from the laser pulse to the electrons is initially done through ionisation as the electrons are still bound to the atoms in the solid target. The level of ionisation achieved determines both the electron density of the plasma and therefore the type of interaction that occurs, as well as the being a measure of the strength of the laser field. Two parameters help characterise the initial stages of the interaction: the Keldysh parameter which indicates the dominant ionisation method occurring, and the coupling parameter, which indicates the coupling strength of the plasma.

Keldysh Parameter

The Keldysh parameter, γ_K, is defined as the ratio of ionising potential, ϵ_i, to ponderomotive potential, U_p, and defines the dominant ionisation mechanism [27]. It is given by:

$$\gamma_K = \sqrt{\frac{\epsilon_i}{2U_p}} \tag{2.37}$$

For $\gamma_K \gg 1$ multiphoton ionisation occurs. This process, shown in Figure 2.4 b, depends on the rate of collisions between photons and electrons and occurs mainly at lower intensities ($\sim 10^{11}\,\mathrm{W\,cm^{-2}}$). For $\gamma_K \approx 1$ tunnel ionisation occurs, as shown in Figure 2.4 c. The laser field

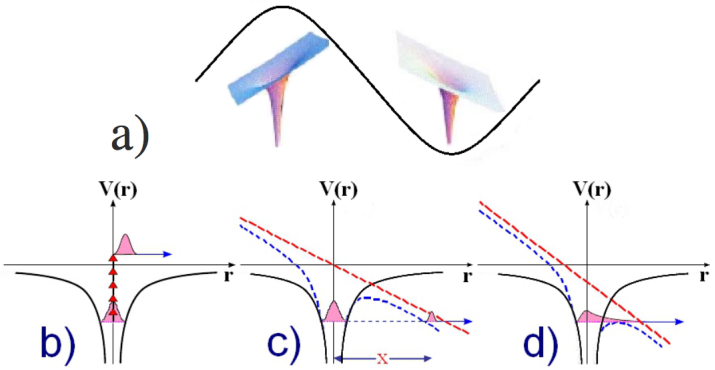


Figure 2.4: A diagram showing the effect of the laser's electric field on the atomic potential. a) Represents the distortion of the atomic potential due to the laser pulse, b) multiphoton ionisation, c) tunnel ionisation, d) barrier suppression ionisation. The black curve represents the initial Coulomb potential. The dashed blue curve represents the distorted Coulomb potential. The dashed red line represents the energy of the least bound electron in the field-free case. [26]

is strong enough to distort the atom's Coulomb potential and the electron can tunnel out. For $\gamma_K \ll 1$ barrier suppression ionisation occurs, as shown in Figure 2.4 d. The laser field suppresses the Coulomb potential entirely and the electron is spontaneously ejected. This is a very rapid process and occurs at very high intensities.

Coupling Parameter

The coupling parameter, Γ, is defined as the ratio of ionisation potential energy to thermal kinetic energy and given by:

$$\Gamma = \frac{Ze^2 n_e^{1/3}}{4\pi\epsilon_0 k_B T_e} \tag{2.38}$$

Where Z is the ionisation level, e the charge of an electron, n_e the number of electrons and T_e their temperature. Γ characterises the ionisation level and coupling strength of a plasma. For $\Gamma \gg 1$, the thermal energy dominates; the plasma is fully ionised and the electrons interact weakly with the ions, creating a "weakly coupled" plasma. For $\Gamma \approx 1$, the thermal energy is approximately equal to the ionisation potential energy. By assuming a Boltzmann distribution for the electron temperature, the plasma will be partially ionised. Therefore the electrons interact strongly with the ions, creating a "strongly coupled" plasma. For $\Gamma \ll 1$, no ionisation occurs as no plasma is formed so the target remains intact. For an electron density of $n_e =$

1.2×10^{30} m^{-3} and a plasma initially at 200 eV, the coupling parameter $\Gamma = 0.4582$ hence the plasma thermal energy dominates.

2.3 Overdense Plasma Heating Mechanisms

As overdense plasmas ($n_e \geq n_{crit}$) are opaque to laser light, laser energy is absorbed at the plasma surface and within the skin depth. Primarily absorbed by electrons due to their higher charge to mass ratio, the energy is later transmitted to the ions and bulk of the plasma through a variety of mechanisms outlined below. Energy absorption, and later redistribution, depends on laser intensity, wavelength, angle of incidence and polarisation, as well as a host of secondary factors [28]. Understanding how the energy is absorbed and redistributed in the plasma is of primary importance to understanding the interaction dynamics occurring. The absorption mechanisms can be split into those occurring in a classical regime, where $a_0 \approx (I\lambda^2)^{1/2} < 10^{18}\,(\mathrm{W/cm^2})^{1/2}\mu\mathrm{m}$, such as collisional and resonant heating, and those occurring for relativistic intensities, with $(I\lambda^2)^{1/2} \geq 10^{18}\,(\mathrm{W/cm^2})^{1/2}\mu\mathrm{m}$, such as vacuum and $\mathbf{J} \times \mathbf{B}$ heating (See Section 2.3.4).

2.3.1 Collisional Heating

Collisional heating, also known as inverse bremsstrahlung, consists of energy transfer through collisions between electrons accelerated in the laser field and cold ions in the surrounding plasma and skin depth. The energy transfer depends on the ion-electron collision rate; the frequency of which is given by:

$$\nu_{ei} \propto \frac{n_e Z}{(T_e[K])^{3/2}} \tag{2.39}$$

where n_e and T_e are the electron density and temperature and Z the ionisation state of the plasma. This absorption mechanism is most effective for cool dense plasmas and for long density scale lengths [29]. Overdense plasmas can also experience collisional heating, with electrons accelerated by the evanescent electric field heating the plasma through collisions.

The fractional energy absorption in a plasma from collisional heating is given by [29]:

$$f_b = 1 - \exp\left(-\frac{32\,L\,\nu_{ei}}{15c}\cos^5\theta\right) \tag{2.40}$$

where L is the length of the plasma density gradient and θ is the angle of incidence. Thus, for a cool dense plasma with high collision frequency the absorption fraction tends to 1.

2.3.2 Resonance Absorption

Resonance absorption is a collisionless energy transfer mechanism that occurs for a laser pulse with incident angle $\theta \neq 0$. If there exists an electric field component parallel to the target surface, the laser pulse will be reflected at the density of $n_{crit}\cos^2\theta$ whereas the component parallel to the density gradient will propagate until n_{crit} (See Section 2.2.3). This evanescent electric field causes fluctuations in the charge density which, if $\omega_l = \omega_p$, causes a resonant electron plasma wave at the critical surface [29]. Therefore, some of the laser energy is transferred to electrostatic oscillations that transfers energy to the remaining plasma through collisions. This heating mechanism is dominant for intensities less than 10^{18} W cm^{-2} and is responsible for hot electron production. Very steep density scale lengths prevent large oscillations of the electrons, leading to a loss in efficiency of energy transfer. Note the electron beam created is perpendicular to the target surface and parallel to the electric field that excites it, and is thus independent of the incoming laser angle.

2.3.3 Vacuum Heating

Vacuum heating occurs in a similar method to resonant heating but for higher intensity lasers and plasmas with steep density gradients. The electrons in the density gradient are again accelerated by the longitudinal component of the laser pulse. Within half a laser cycle, they gain longitudinal momentum and propagate beyond the critical surface. Thus, when the electric field of the laser reverses, they no longer feel the restoring force and travel balistically through

the target. The electrons are accelerated in bunches at the laser frequency and normal to the targets front surface. Energy is then lost through collisions.

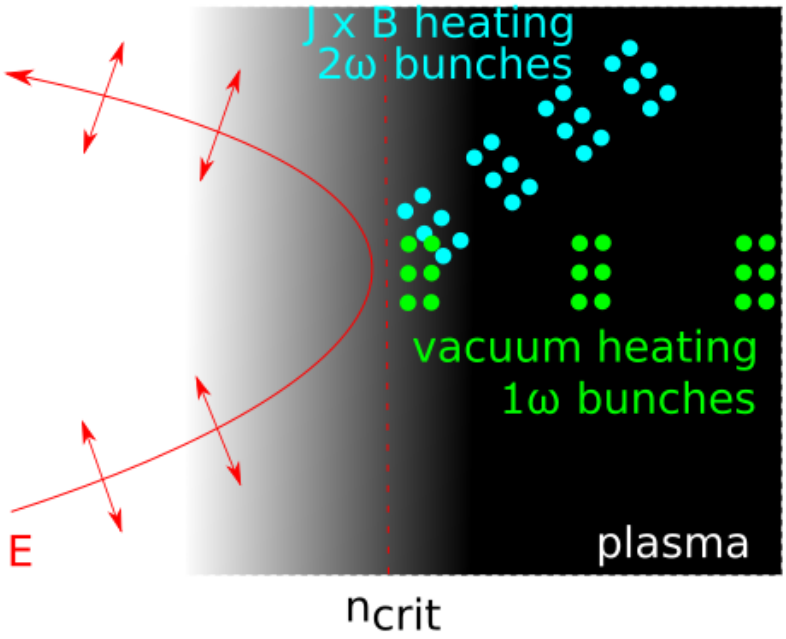


Figure 2.5: Vacuum and $\mathbf{J} \times \mathbf{B}$ heating mechanisms in a plasma. Vacuum heating produces electron bunches perpendicular to the critical surface in 1ω bunches, whereas $\mathbf{J} \times \mathbf{B}$ heating produces electron bunches along the laser axis at twice the laser frequency.

2.3.4 $\mathbf{J} \times \mathbf{B}$ Heating

$\mathbf{J} \times \mathbf{B}$ heating occurs for relativistically high laser intensities, i.e. $a_0 > 1$, where the $\mathbf{v} \times \mathbf{B}$ term in the Lorentz force can no longer be ignored and becomes comparable to the contribution of the electric field. As shown in Section 2.2.6, for linearly polarised light the magnetic field causes the electron to oscillate longitudinally at twice the laser frequency with velocity $v_d = \frac{1}{2}a_0^2 c$. Hence a similar effect to vacuum heating occurs: electrons are accelerated in the laser field and propagate into the target along the laser axis. The electrons are accelerated in bunches at twice the laser frequency, and heat the target through collisions or electrostatic oscillations. Energy absorption increases for increasing laser intensity, and peaks for normal incidence laser angles [30]. This effect is heavily suppressed for circularly polarised light as it depends on the electron longitudinal oscillation (See Section 2.2.5).

2.4 Ion Acceleration Mechanisms

While this thesis concentrates on optical diagnostics from thin foil laser-plasma interactions, similar experiments in the literature are benchmarked using the ion energies and spectra. In order to fully understand the plasma dynamics, an overview of the particle acceleration mechanisms relevant to this thesis will be given.

The acceleration regimes of interest to this thesis are those occurring from high power, relativistic, short pulse lasers. For pulse lengths in the order of 10's of femtoseconds, the particle acceleration mechanisms will depend on particle motion. As the laser pulses are highly relativistic, strong target heating and significant electron motion is expected in a fully ionised plasma.

2.4.1 Sheath Acceleration

Sheath acceleration is the most researched ion acceleration mechanism [31] [32] [33] [34] and consists of irradiating a solid target of thickness $> 1\,\mu m$ with a high intensity laser pulse. It works by accelerating electrons into the target by one of the heating methods described above, usually vacuum or $J \times B$ heating. As the electrons stream to the rear surface, initially they escape into the vacuum and leave a positively charged rear surface behind. A large electric field is then set up on the target's surface, known as an electrostatic sheath. Electrons with sufficient energy escape the sheath and continue into the vacuum, thereby increasing the charge differential, whereas lower energy electrons are dragged back into the bulk of the target. The sheath field is maintained by the continuously accelerated and recirculating electrons, which in turn is able to accelerate surface ions in the strong electric fields. Sheath fields are established on both target surfaces, as shown in Figure 2.6.

In order to quantitatively describe the acceleration of particles through sheath acceleration, analytical models were developed to predict the ion spectrum and maximum energies obtained in experiments [32] [36] [37] [38] [39] [40] [41] and references there-in. By assuming a collisionless

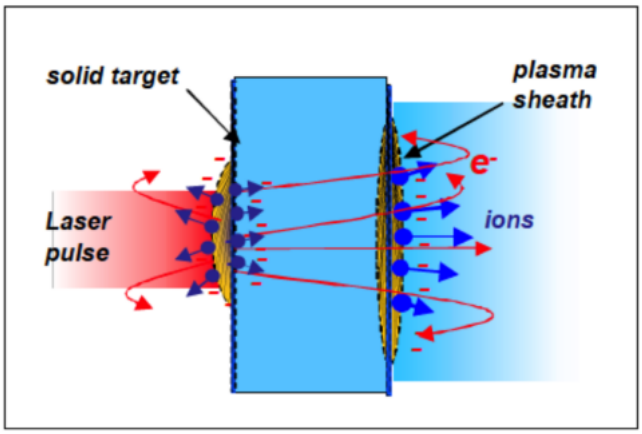


Figure 2.6: Figure showing the sheath acceleration mechanism. Here, the accelerated and recirculating electrons are shown in red, ions shown in blue and the sheath fields in gold [35].

plasma expansion, Mora [40] showed that the maximum ion energy obtainable is given by:

$$E_{max} = 2\,Z\,k_B\,T_e\,ln(\tau + \sqrt{\tau^2 + 1})^2 \tag{2.41}$$

where Z is the ion charge number, T_e is the electron temperature and τ is given by $\tau = \omega_{pi}t/\sqrt{2e}$. ω_{pi} is the ion plasma frequency and t refers to the acceleration time, or the time for which the ions are under the influence of the sheath. It has been shown that the approximation $t_{acc} \approx 1.3\tau_l$ [42], where τ_l is the pulse length of the laser, agrees well with experimental and simulation results.

Sheath acceleration is characterised by it's thermal ion spectra. A relatively thick target ensures it remains overdense for the duration of the laser pulse, thus ensuring a constant supply of accelerated electrons to maintain the sheath field. The ion energies obtained are highly dependent on the electron temperature (see section 2.4.4 and equation 2.41), and therefore on the plasma conditions generated by the laser pulse. For a $\sim 1\,\mu$m wavelength laser with pulse length 750 fs, the maximum proton energy currently measured lies at 94 MeV [43]. For a much shorter pulse length laser (800 nm and ~40 fs) the highest ion energy lies around 35 MeV [44] [45] [46].

2.4.2 Radiation Pressure Acceleration

Radiation pressure acceleration (RPA) consists of accelerating electrons using the radiation pressure of the photons. First shown theoretically by Esirkepov et al. [47] and Robinson et al. [48], RPA occurs when the radiation pressure exerted by the laser pulse due to the momentum of the photons is greater than the thermal pressure exerted by the expanding plasma. The radiation pressure due to an intense laser pulse can be calculated by considering the momentum change of a photon reflecting off a slab. The pressure exerted by the radiation P_R is then given by:

$$P_R = (1 + R)\frac{I_l}{c} \tag{2.42}$$

where R is the reflectivity of the target surface ($R = 0$ is full absorption, $R = 1$ is perfect reflection) and I_l is the intensity of the laser. For laser intensities of $I_l \approx 10^{20}\,\mathrm{W\,cm^{-2}}$, the pressure exerted can reach $P_R = 100\,\mathrm{Gbar}$.

Depending on the target thickness two sub regimes exist: the hole boring regime where the laser bores a hole through a thick target or the light-sail regime when the laser pulse accelerates a slab of material using the radiation pressure of the photons. In hole boring, upstream ions are reflected off a sheath field and hence have a limited acceleration time [49] [50], as opposed to light sail where downstream ions are accelerated continuously by the laser. As the latter is of particular interest to this thesis, it will be expanded on below.

Light Sail Regime

For thin targets, the electrons in the focal spot are pushed out due to radiation pressure, establishing a strong space charge field. This accelerates the ions, causing the plasma to propagate in the forward direction. If the electron population is able to remain at relatively low kinetic energies such that they do not escape the space-charge field, the accelerated plasma slab remains overdense and thus sustains the acceleration mechanism for the duration of the laser pulse. This is shown in Figure 2.7.

To maximise ion energies, the target thickness must be optimised such that the plasma slab

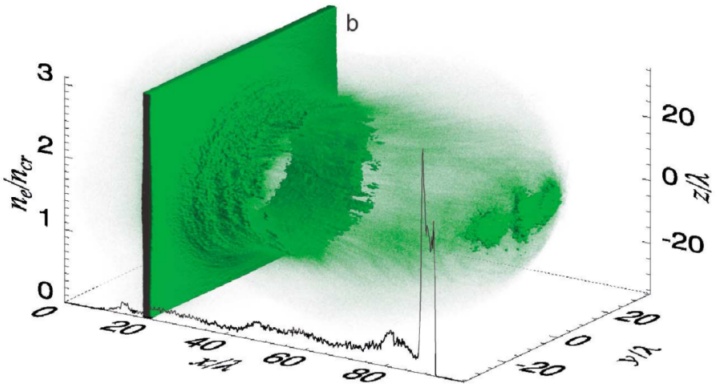


Figure 2.7: Light Sail RPA in a 3D simulation. The ion density is shown in green, with the density lineout along the laser axis shown in black. Taken from Esirkepov et al. [47]

is thick enough to remain overdense for the duration of the laser pulse. For a target of the order of the skin depth, the laser electric field penetrates a significant distance into the target, thus heating a large percentage of the electrons in the focal spot. This causes rapid target expansion and reduce it's density. If the electron density drops such that the target becomes relativistically underdense, the laser will transmit though, terminating the radiation pressure acceleration. Conversely, a thick target means a large number of particles and hence a large mass to accelerate, resulting in less kinetic energy per nucleon. Thus, to optimise ion energies, a compromise between these two effects must be obtained.

The stability of the target can also be improved by reducing the laser pulse length. Shorter pulses would give hydrodynamic instabilities, such a Rayleigh-Taylor instabilities [51], less time to develop thus maintaining the structural integrity of the target. Additionally, as the plasma slab's velocity increases, the critical density increases due to the Doppler shift of the laser in the frame of the foil.

The velocity of the ions is given by:

$$v_{ls} = (1 + R)\frac{\tau}{m_i n_i l_t}\frac{I}{c} \tag{2.43}$$

where l_t is the target thickness. Thus, light sail is an interesting acceleration regime as it has longer acceleration times and better ion energy scaling with laser intensity than sheath

acceleration (I^2 instead of $I^{0.5}$ for sheath acceleration, see Section 2.4.4). Once intensities above $10^{22}\,\mathrm{W\,cm^{-2}}$ are achieved, a relativistic equation of motion, as derived in [52], must be used. Circular polarisation is used to reduce electron heating and ensure the target remains above critical density. Experimentally this regime has been observed for a range of laser parameters, and is identified though the monoenergetic bunch feature of the high energy ions [53].

Rykovanov et al [21] found the optimum target thickness l_{opt} to be given by:

$$l_{\mathrm{opt}} = \frac{a_0 n_{\mathrm{crit}} \lambda}{\pi n_e} \tag{2.44}$$

Thus, for a laser of wavelength $\lambda = 800\,\mathrm{nm}$ and target with electron density $n_e = 685 n_{\mathrm{crit}}$ and $a_0 = 12.5$, the optimum target thickness for light sail acceleration is 5 nm.

2.4.3 Relativistic Transparency

The relativistic transparency (RT) regime is a type of enhanced sheath acceleration that occurs for targets that transition into transparency during the laser-plasma interaction. In optimum RT conditions, the interaction begins with sheath acceleration, where the electrons in the focal spot are accelerated to the rear surface and establish a space-charge field. As the electrons stream forward and the target expands, the local electron density in the focal spot decreases until it drops below the relativistic critical density γn_{crit}. Thus, the laser is able to penetrate the target and volumetrically heat and accelerate the electrons directly to relativistic velocities. The ions are subsequently accelerated in the space charge field which allows the electrons to transfer their kinetic energy to the ions by reducing their relative drift velocity [54]. As the change in density occurs on timescales shorter than the laser pulses used in this thesis (less than a few femtoseconds), the plasma can be considered to act as a shutter, with this phenomenon known as “plasma shuttering” [55].

For optimum acceleration, the target should go relativistically transparent before the peak of the laser pulse, thus ensuring the electrons interact with the peak laser intensity. This can be controlled by varying the target thickness, as shown by Henig et al. [56]. The ion

spectra produced is similar to that of sheath acceleration: thermal with enhanced ion energies [57]. However, spectra with features such as monoenergetic bunches (shown by using circular polarisation by Yin et al [58]) or enhanced spectral peaks (shown by Dover at al [59]) are also possible. Relativistic transparency currently holds the record for the highest proton energies measured of 94 MeV [43].

2.4.4 Electron Temperature Scaling

As described above, all acceleration mechanisms are heavily dependent on the temperature of the electron population. An analytical model based on energy absorption is very difficult to construct due to the competing effects of different heating mechanisms and the large number of variables such as laser intensity, polarisation, angle of incidence, plasma scale length and bulk electron temperature. Most models attempt to correlate the electron temperature with the normalised laser vector $a_0 \simeq \sqrt{I\lambda^2}$; the ponderomotive, or Wilks [49], scaling estimates that $T_e \propto (I\lambda^2)^{\frac{1}{2}}$. While this is reasonably accurate for lower intensity, it vastly overestimates electron temperatures at intensities above $10^{19}\,\mathrm{W\,cm^2}$ [60] [61] [62]. Thus, for relativistic intensities the Beg scaling is used [60], where $T_e \propto (I\lambda^2)^{\alpha}$ was fit onto experimental data and a value of $\alpha \approx \frac{1}{3}$ was found [62]. Since, Haines et al. [63] have developed an analytical model based on conservation of energy and momentum in the relativistic domain that agrees closely with the Beg scaling. The analytical model predicts absorption efficiencies $> 90\%$ for relativistic intensities [63]. Another model based on the weighted averages of the electron kinetic energy has been developed by Kluge et al. [64], including a time dependence to the electron current [65]. The analytical values agree well with experimental and simulation results, and pave the way for a time resolved relativistic analytical model in the future.

2.5 Second Harmonic Generation in a Plasma

High harmonic radiation can be produced in the plasma through many different mechanisms, and can be used as a diagnostic of the existing plasma conditions. As for most ion acceleration

experiments only the second harmonic is diagnosed, an overview of various second harmonic generation mechanisms is given below.

2.5.1 Coherent Wake Acceleration

CWE is a method of second harmonic generation that occurs at non relativistic intensities and oblique angles, and can somewhat be seen as the opposite to resonant absorption. The electrons are accelerated in bunches into the target by the laser pulse through the previously described methods and cause a density wave [66]. The density wave causes plasma oscillations with frequency related to the localised density. When the plasma wave phase-matches with the incoming laser pulse, radiation is emitted through linear mode conversion [67] and can be reflected back in the specular direction. Thus, harmonics in the range of ω_p to $\omega(n_e^{max})$ are emitted from the front and rear surface, with maximum efficiencies reaching 0.001% [68]. CWE scales linearly with the quantity of charge in the electron bunches, is most efficient for short density scale lengths [69] and can achieve harmonics up to 10 - 20 ω_0 depending on the plasma density.

2.5.2 Relativistic Oscillating Mirror

Harmonic generation by the relativistic oscillating mirror (ROM) method occurs on the front surface for relativistic laser pulses (I $>10^{18}\,\mathrm{W\,cm^{-2}}$) incident on targets with shallow density gradients [69] [70]. The electrons in the density gradient are accelerated normal to the critical surface into the target, either through the p - polarised oblique laser pulse or through the $J \times B$ force for normal incidence. Thus, the critical surface oscillates and couples with the laser pulse to generate new harmonics through the phase redistribution of incoming photons. ROM mechanism has been extensively studied in simulations [71] [72] and experimentally [73] [74] [75]. Note that no harmonics are produced for circularly polarised light at normal incidence [76]. However, this rule assumes a planar target and does not take into account target buckling that occurs in experimental conditions. Additionally, due to selection rules, only odd number

harmonics are produced for normal incidence or s - polarised light, as the radiation couples to the $J \times B$ accelerated electrons at frequency 2ω. This is not seen experimentally due to target distortion [73]. ollision frequency

2.5.3 Optical Transition Radiation

Transition radiation was first discovered theoretically by Ginzburg and Frank in 1945 [77] when observing a charged particle pass perpendicularly between two homogeneous media. Explored more in depth experimentally from 1959 [78], transition radiation is often used to measure the longitudinal temporal duration of electron bunches in conventional accelerators by directing the electron beam into a foil and measuring the emitted transition radiation. By Fourier transforming the spectrum of the emitted transition radiation, the temporal duration of the electron bunch can be calculated [79] [80].

In laser-plasma interactions, electrons generated at the targets front surface can propagate through the target to the rear surface. As they approach the plasma-vacuum interface, the electrons propagate through an inhomogeneous media, or medium with changing electric properties. Thus, each electron induces a time dependent polarisation field which in turn excites the free charges, or dipoles, causing them to radiate. This radiation is known as transition radiation.

Alternatively, this could be understood as follows: in each medium (plasma or vacuum), the electron's field are related to it's motion and the properties of the medium. Upon passing the interface, it's fields must reorganise to abide by the new conditions, therefore losing energy in the form of radiation [81].

Transition radiation is formed in an area called the formation zone at the boundary of two media with different dielectric constants. When considering an electron propagating normal to the rear surface, the formation zone can be renamed formation length, L_f, and can be written as [82]:

$$L_f = \frac{c}{\omega} \frac{\beta}{\left| 1 - \beta \epsilon_r^{1/2} \cos\theta \right|} \tag{2.45}$$

where ϵ_r is the dielectric constant of the medium, θ is the observation angle and ω is the frequency of the emitted radiation. For a plasma with $\epsilon_r \gg 1$ (an overdense plasma), Equation 2.45 simplifies to $L_f = c/(\omega_p \cos\theta)$, where θ corresponds to the observation angle. For an observation angle of $\theta \approx 0$ this simplifies to the plasma skin depth $l_s = c/\omega_p$.

The total energy radiated by one particle is given by [83]:

$$W = \frac{\alpha\hbar}{3}\omega_p\gamma \tag{2.46}$$

where $\alpha = e^2/4\pi\epsilon_0\hbar c$ is the fine structure constant. Thus, Equation 2.46 shows that the total radiated energy is proportional to γ, where γ is now the Lorentz factor of the electron. Unlike standard dipoles, the radiation is emitted at an angle proportional to the energy of the electron, given by:

$$\gamma\theta \leq 1 \tag{2.47}$$

Thus, transition radiation is maximised for plasmas with rear surface scale lengths equal to the skin depth and for high energy, and hence high γ, electrons. The angular distribution of radiation is shown in Figure 2.8 for two values of γ. As the electrons become more relativistic, the radiation is emitted at angles closer to the electron axis z, corresponding to angles $\theta \approx 0$.

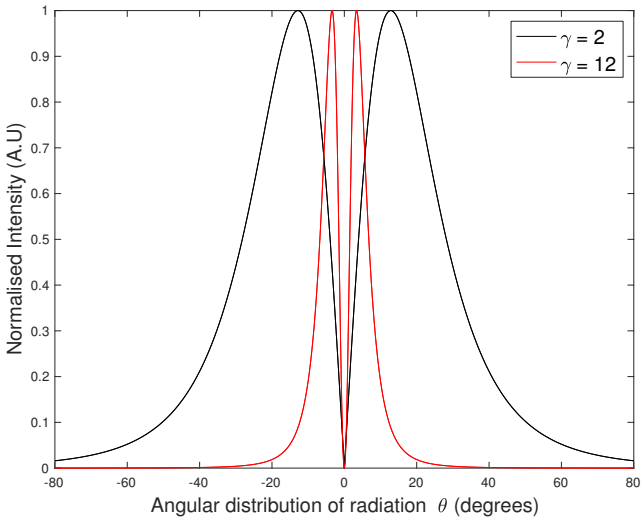


Figure 2.8: Intensity of transition radiation as a function of emitted angles for two values of γ.

As electrons are generally accelerated in bunches in the relativistic regime, the electromagnetic fields created can interfere coherently to produce a signal orders of magnitude greater than the incoherent radiation. Called coherent transition radiation (CTR), the dipoles oscillate at multiple integers of the laser frequency due to electron bunching from the heating mechanisms. Hence they emit radiation at frequencies of $n\omega_l$ for $n = 1, 2, 3, ...$ dependant on the dominant electron acceleration mechanism. For resonant absorption, the radiation is peaked at $n\omega_L$, whereas for $\mathbf{J} \times \mathbf{B}$ heating the radiation is peaked at $2n\omega_L$.

A defining property of transition radiation is the radial polarisation of the emitted radiation, as shown on the right in Figure 2.9. Thus, for a centred electron beam, the radiation is emitted as a 3 dimensional projection of the form shown in Figure 2.8, with polarisation as shown by the arrows in Figure 2.9. The polarisation of the measured radiation is therefore dependent on the observation angle. This can be exploited experimentally to separate transition radiation from alternative sources such as transmitted laser light or general plasma emission.

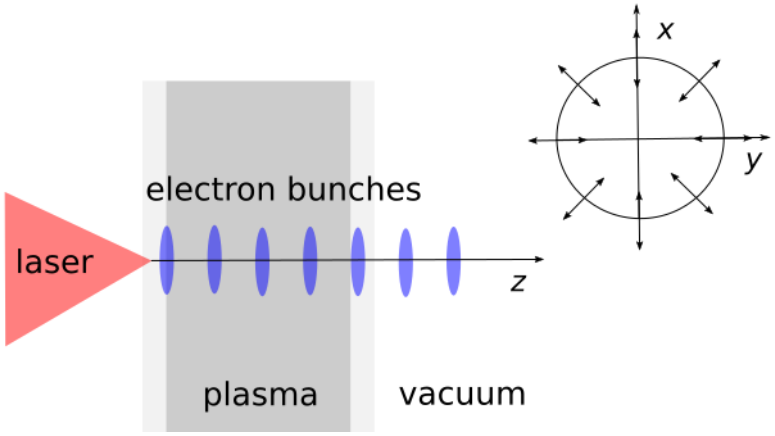


Figure 2.9: Electron bunches propagating through a target, with the radial polarisation of radiation shown on the right.

Spectrally, the emitted radiation depends on the number of bunches in the electron beam, the target thickness and the fast electron temperature. For a large number of electron bunches, produced for example by a long laser pulse, the off-resonant frequencies interfere destructively, and thus a narrow spectral width is observed. As the electron bunches created at the front surface have an energy distribution that spans a range of acceleration times, the bunches exiting the rear surface are not perfectly in phase. Thus, the coherence of the radiation and therefore

it's intensity is limited. This generates a non-flat spectrum with a roll-off dependent on electron direction and observation angle [81], where the spectral cut-off can be approximated to $\omega \sim \gamma\omega_p$. Finally, as target thickness increases the intensity of the signal W at a given wavelength is expected to decrease due to coherence effects. This effect becomes less noticeable for higher temperature fast electrons.

Based on work by Bellei et al [84], an estimate of the temporal width of the CTR signal, Δt_{CTR}, can be calculated by using the following equation:

$$\Delta t_{CTR} \quad = \quad n_b \Delta t \quad \simeq \quad 0.9 \frac{\lambda_{obs}^2}{c \Delta \lambda_{obs}} \tag{2.48}$$

Where n_b corresponds to the number of electron bunches, Δt the time per bunch (the temporal separation of each bunch), λ_{obs} the wavelength of radiation observed and $\Delta\lambda_{obs}$ the bandwidth of the observed radiation. For a 800 nm wavelength laser with pulse length 48 fs, transition radiation emitted at 800 nm with bandwidth 24.5 nm was measured. The corresponding temporal width of CTR was calculated to be $\Delta t_{CTR} = 77$ fs, where differences between transition radiation emission and driving pulse length could be attributed to measurement errors and the rising and falling edges of the laser pulse still capable of accelerating hot electron bunches.

Thus, transition radiation is an interesting diagnostic in a laser-plasma experiment as it gives information on the electron bunch generation, primary electron heating mechanisms, as well as information on the target's rear surface [85].

Chapter 3

Experimental Methods

This chapter describes the experimental and analytical techniques used to obtain the results presented in this thesis. The experimental diagnostics and their calibration are presented first, followed by a description of the simulation techniques used.

3.1 Ti:Sapphire Lasers

The results presented in this thesis are based on experiments performed with a titanium-sapphire laser system: the Astra-Gemini laser at the Central Laser Facility and the J-Karen-P laser at the Kansai Photon Science Institute. Ti:Sapph lasers start with a modelocked oscillator, before a selected pulse is amplified in a titanium-doped sapphire crystal from which the laser gets its name [86]. Due to its wide bandwidth and tunability, it is capable of producing pulses in the range $650 - 1100\,\mathrm{nm}$. However, it is generally lased at the point of peak efficiency, which corresponds to a wavelength of $800\,\mathrm{nm}$. With further amplification stages using for example the chirped pulse amplification scheme (see Section 1.1), it can produce pulses with tens of joules in energy and pulse lengths ranging from $5\,\mathrm{fs}$ to around a few picoseconds. Depending on beam size, amplification and design, the repetition rate of the laser lies within the few pulses per second.

3.2 FROG

In order to properly diagnose the experimental plasma conditions, a good understanding of the temporal and spectral characteristics of the incoming laser pulse is crucial. Most diagnostics, such as calorimeters, spectrometers and autocorrelators are time or spectrum integrated measurements that do not allow for a full 2D (time and space) or 3D (time, space and frequency) reconstruction of the laser pulse. To get a full reconstruction, both the intensity and phase of the pulse must be simultaneously determined.

To fully reconstruct the amplitude and phase of a laser pulse, a diagnostic called a FROG (Frequency Resolved Optical Gating) can be used. A FROG spectrally disperses the autocorrelation trace of a laser pulse, and uses an iterative algorithm to retrieve the temporal and spectral intensity of the input pulse. As the detector is neither time nor spectrally integrating, it is able to find the unique value of $E(t)$ and $\phi(t)$ that produced the detected trace. It is also able to retrieve the phase of the electric field, thus providing information such as the chirp and instantaneous frequency of the incoming pulse. For short pulses, it can be used as a single-shot diagnostic, thus allowing for on-shot information of every laser pulse.

3.2.1 Apparatus

A SHG-FROG can be described as a autocorrelator followed by a spectrometer, so that the detector measures both the temporal and spectral evolution of the pulse along perpendicular axes.

The autocorrelation consists of crossing two identical replicas of the input pulse in a non-linear crystal, as shown in Figure 3.1. This creates a second harmonic pulse propagating in the direction of the sum of the $\hat{k}$ vectors. Second harmonic generation (SHG) is interesting as it allows for the sum of two fields to be expressed as a unique signal that can be distinguished spatially and spectrally from all other products. Thus, the desired signal can be measured with little background noise and no frequency filtering. Mathematically the sum of two identical

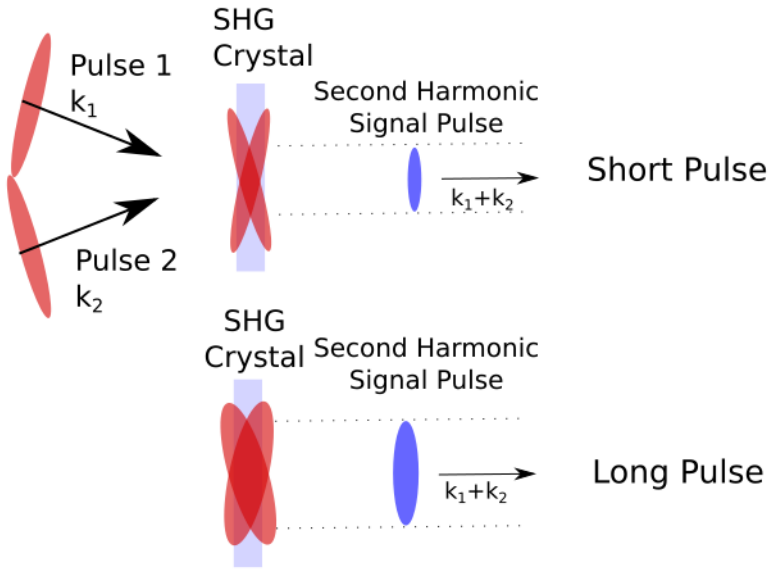


Figure 3.1: Set-up of a FROG autocorrelator shown for a short and long pulse.

electric fields $E_{1,2}(\mathbf{r},t) = E_0(\mathbf{r},t)\exp[i(\omega t - \mathbf{k}_{1,2}\cdot\mathbf{r})] + c.c$ is given by:

$$\begin{aligned}(E_1+E_2)^2 = {} & 4E_0^2 + E_0^2\exp(2i(\omega t - \mathbf{k}_1\cdot\mathbf{r})) + E_0^2\exp(-2i(\omega t - \mathbf{k}_1\cdot\mathbf{r})) \\ & + E_0^2\exp(2i(\omega t - \mathbf{k}_2\cdot\mathbf{r})) + E_0^2\exp(-2i(\omega t - \mathbf{k}_2\cdot\mathbf{r})) \\ & + 2E_0^2\exp(i((\mathbf{k}_1-\mathbf{k}_2)\cdot\mathbf{r})) + 2E_0^2\exp(-i((\mathbf{k}_1-\mathbf{k}_2)\cdot\mathbf{r})) \\ & + 2E_0^2\exp(i(2\omega t - (\mathbf{k}_1+\mathbf{k}_2)\cdot\mathbf{r})) + 2E_0^2\exp(-i(2\omega t - (\mathbf{k}_1+\mathbf{k}_2)\cdot\mathbf{r}))\end{aligned} \tag{3.1}$$

The final line of this equation describes the second harmonic generation in the crystal. The second to fifth term represent the second harmonic of the original pulses.

Second harmonic radiation is produced in a crystal where the polarisation density vector $\mathbf{P}(t)$ responds non-linearly to the radiation $E(t)$ transmitted through it:

$$\mathbf{P} = \epsilon_0(\chi^{(1)}\mathbf{E}(t) + \chi^{(2)}\mathbf{E}^2(t) + ...) \tag{3.2}$$

where $\chi^{(n)}$ is the n-th order susceptibility of the material. Physically, $\mathbf{P}$ relates to the ability of the molecules in the material to respond to an applied electric field. The intensity of second harmonic radiation generated, I_2, is given by the equation:

$$I_2 = I_1^2[\chi^{(2)}]^2L^2\mathrm{sinc}^2(\Delta kL/2) \tag{3.3}$$

where k_1 and k_2 now refer to the wavenumbers of the first and second harmonic respectively such that $\Delta k = 2k_1 - k_2$, $\chi^{(2)}$ is the susceptibility of the material, L is the distance travelled through the crystal, and I_1 is the intensity of the incident radiation. Equation 3.3 shows that I_2 is heavily dependent on the intensity of the incident radiation, the non-linearity of the SHG crystal, the crystal thickness and the phase matching condition, Δk. To optimise the second harmonic signal, a non-linear crystal (typically beta barium borate (BBO) or potassium dihydrogen phosphate KDP) with high $\chi^{(2)}$ is used. Additionally, L is related to the crystal thickness by $L = d\cos(\theta)$ where d is the crystal thickness and θ the intersection angle. L is proportional to the number of dipoles in the medium that radiate coherently, thus thicker crystals produce a stronger I_2.

However, for efficiency, the second harmonic generation is bound by the phase matching condition. This states that the induced polarisation in the crystal, which produces the second harmonic radiation, and the second harmonic radiation produced at an earlier time must have the same phase velocity. This condition ensures that the second harmonic radiation produced at consecutive timesteps interfere coherently, thus making the process orders of magnitude more efficient. The phase matching condition is given by $\Delta k = 0$ and can be rewritten as (for noncollision frequency linear geometry) as $\eta(\omega_1)\cos(\theta/2) = \eta(2\omega_1)$. This is applicable for a single frequency, but, specifically for short pulses, each laser pulse is made up of numerous frequencies, and thus phase-matching must be achieved for the bandwidth of the pulse. The phase-matching bandwidth can be written as [19]:

$$\delta\lambda_{\mathrm{FWHM}} = \frac{0.44\lambda_0/L}{\left|\eta'(\lambda_0) - \frac{1}{2}\eta'(\lambda_0/2)\right|} \tag{3.4}$$

where λ_0 is the central wavelength and $\delta\lambda_{\mathrm{FWHM}}$ is the bandwidth.

Thus, as the phase matching bandwidth is inversely proportional to the thickness of the nonlinear medium, for short pulse laser pulses with large bandwidths a thinner crystal is needed. This is also visible in Equation 3.3, where the sinc^2 function is maximum for $\Delta kL/2 = 0$, so Δk and L are inversely proportional. Therefore, to satisfy Equation 3.3, a compromise between SHG efficiency and phase-matching bandwidth must be found, with thinner crystals more suited to

shorter pulses.

The autocorrelation results in time being mapped transversely across the crystal, thus expressing it as a function of displacement across the crystal. This is shown in Figure 3.1 where pulse 2 precedes pulse 1 at the top of the crystal, with the reverse happening at the bottom of the crystal. For longer pulses, hence spatially thicker, the resultant second harmonic trace has a larger transverse beam size, representing the longer time duration. The autocorrelation is then diffracted by a grating and incident on the detector, where the intensity profile takes the form of:

$$I_{\text{detector}}(\tau, \omega) = \left| \int_{-\infty}^{+\infty} E(t)\, E(t-\tau) \exp(-i\omega t) dt \right|^2 \tag{3.5}$$

where $E(t)$ and $E(t-\tau)$ are the electric field of two identical replicas of the input pulse offset by time τ. Thus, I_{detector} is the spectrum of the output of the SHG crystal, the autocorrelation, given by $E(t)\, E(t-\tau)$. From Equation 3.5, the intensity and phase can be retrieved for all input electric fields, including complex ones. However, the FROG has two trivial ambiguities: the absolute measure of time and the absolute measure of phase. The absolute measure of time cannot be determined as it has no reference pulse (as in interferometry). This also means that, independently, the pulse cannot be directed in time. i.e one cannot distinguish $E(t)$ and $E(-t)$. This ambiguity can be overcome during the calibration, as will be explained in Section 3.2.3. An ambiguity in absolute phase translates into $E(t)$ and $E(t)\exp(i\phi_0)$ being indistinguishable, and can not be resolved.

3.2.2 Retrieval Algorithm

The FROG uses an iterative algorithm to retrieve the electric field and phase of the input laser pulse from the detector image [87] [88] [19]. The algorithm starts by assuming a gaussian laser pulse $E(t)$, and computes the corresponding FROG trace called the retrieved trace. The retrieved trace is then compared to the detector image, and the corresponding FROG error,

$G^{(k)}$ is computed. The error is given by:

$$G^{(k)} = \sqrt{\frac{1}{N^2}\sum_{i,j=1}^{N}\left|I_{\text{detector}}(\omega_i,\tau_j) - \mu I^{(k)}_{\text{FROG}}(\omega_i,\tau_j)\right|^2} \tag{3.6}$$

where I_{detector} is the experimentally measured FROG trace, I_{FROG} is the algorithm retrieved FROG trace of the k-th iteration and μ is a scalar used to minimise the error of the k-th retrieved guess. ω_i, τ_j are the i-th and j-th vector of the frequency and delay respectively. N is the number of pixels of the $N \times N$ FROG matrix.

The algorithm used to analyse the results in this thesis was written by Matthew Streeter [89]. It comprises a range of different methods such as data constraint, generalised projections and a genetic algorithm to achieve the global minimum in the error function. The functionalities of each are explained below.

Data Constraints

The first step constrains the guess electric field within the amplitude limits of the raw experimental data. Thus, the magnitude of the guess electric field must be equal to the square root of the experimental trace. This is repeated in the time and frequency domain, and an approximate solution is rapidly found. Note, this does not change the phase of the guess field and therefore is not likely to be the end solution, except for very simple pulses.

Generalised Projection

The generalised projection method works similarly to the data constraint method, in that the data and mathematical limits must be respected, with the additional constraint that each subsequent guess field must differ as little as possible from the previous. This adds an additional variable to minimise, and is more computationally expensive that the Data Constraint method explained above.

To avoid stagnation, an overall control algorithm is used to swap between the two above retrieval methods. However these methods can cause the algorithm to tend towards a local, not global, minimum. Thus, a third retrieval method is used: a genetic algorithm.

Genetic Algorithm

A genetic algorithm solves a problem by "trial and error". In this case and for each iteration, a group of possible solutions are suggested, with the algorithm calculating the fitness of each. A second generation of solutions are then proposed, derived from the first using two methods. The new guess fields can either be bred from two previous good solutions, where half the values are sampled at random from each parent and combined to form the offspring solution. Else, a new guess field can be generated by randomly changing values of a parent solution, in a process called mutation. The breeding method conserves features of the best solution whereas the mutation method can lead to the discovery of features belonging to the optimal solution. Thus, a compromise between both methods is used to find the optimal solution. Note the guess fields of both methods are non-deterministic, and change for each run of the retrieval algorithm. Thus two retrievals run on a same raw FROG trace may not produce identical results.

The flow of retrieval methods is given in Figure 3.2. For more information on the algorithm set-up and methods, an interested reader can refer to [89].

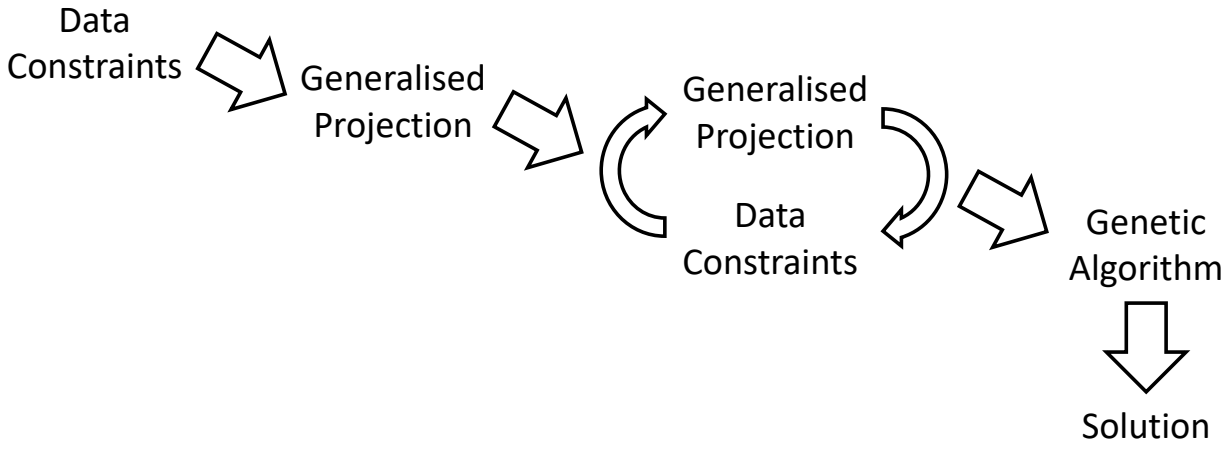


Figure 3.2: A flow diagram of the FROG retrieval algorithm.

Once the algorithm converges on the unique solution with a minimised error function, it outputs the intensity and phase of the retrieved pulse. Examples of raw FROG traces and the corresponding retrieved algorithm-produced traces can be seen in Figure 4.9 in Chapter 4. The validity of the retrieved pulse is expressed as the final value of the error function, which for a good retrieval lies around the 2% mark. It is important to note that an inaccurate FROG retrieval can still produce a low error value, in particular if the detector image has a low dynamic

range. Conversely, the opposite is also possible, with a decent retrieval potentially showing a large error due to effects such as noise. Thus, each FROG retrieval presented in this thesis was manually checked by visually inspecting the raw and retrieved pulses and by ensuring all pulses were symmetric in time. Asymmetric raw FROG traces were discarded as no accurate retrieval would be possible.

3.2.3 Calibration

In order to calibrate the FROG both spectrally and temporally, a double pulse generated by a high repetition rate oscillator or interferometer can be used. This generates an electric field E_{cal} given by:

$$\begin{aligned} E_{\text{cal}}(t) = E_1 \exp\left(-\frac{(t-\Delta t_{\text{sp}}/2)^2}{\sigma_t^2}\right) \exp\left(i\omega_0(t-\Delta t_{\text{sp}}/2)\right) \\ + E_2 \exp\left(-\frac{(t+\Delta t_{\text{sp}}/2)^2}{\sigma_t^2}\right) \exp\left(i\omega_0(t+\Delta t_{\text{sp}}/2)\right) \end{aligned} \tag{3.7}$$

where Δt_{sp} is the known temporal offset and $E_{1,2}$ is the relative magnitudes of the two pulses. This is visualised in Figure 3.3, where the electric field is plotted on the left and the associated FROG trace is plotted on the right. Note, as a FROG trace is an autocorrelation, all FROG traces are symmetric (except in the case of significant spatio-temporal distortions). The asymmetric pulse will appear once the retrieval algorithm is run. The pulse separation Δt_{sp} is the distance between the central peak and a satellite, thus calibrating the FROG temporally. Spectrally, the modulations in frequency correspond to $\Delta\omega = 2\pi/\Delta t$ [90].

For retrieval algorithms with a fixed temporal direction, a double pulse with known, different amplitudes can be used to determine the direction of time. Note, as all autocorrelations are symmetric, this is not visible on the FROG trace, but becomes apparent during the retrieval. Alternatively, for a retrieval agorithm without fixed temporal direction, two FROGs must be used. By placing a source of known linear GVD (group velocity dispersion) in the incoming beam, additional chirp will be added or subtracted to the retrieved value. Thus by comparing these two retrieved values, the absolute direction of time can be retrieved.

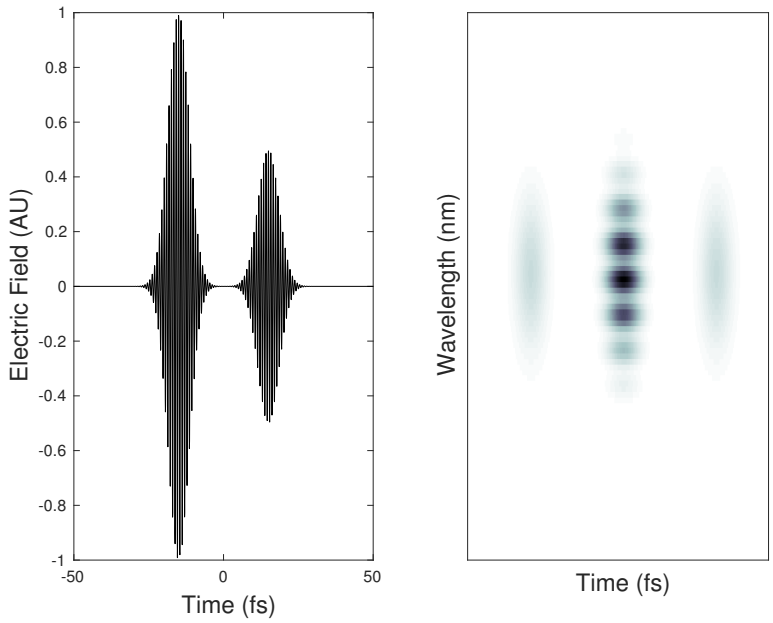


Figure 3.3: The electric field and the FROG trace of a double pulse.

3.2.4 Wigner Transforms

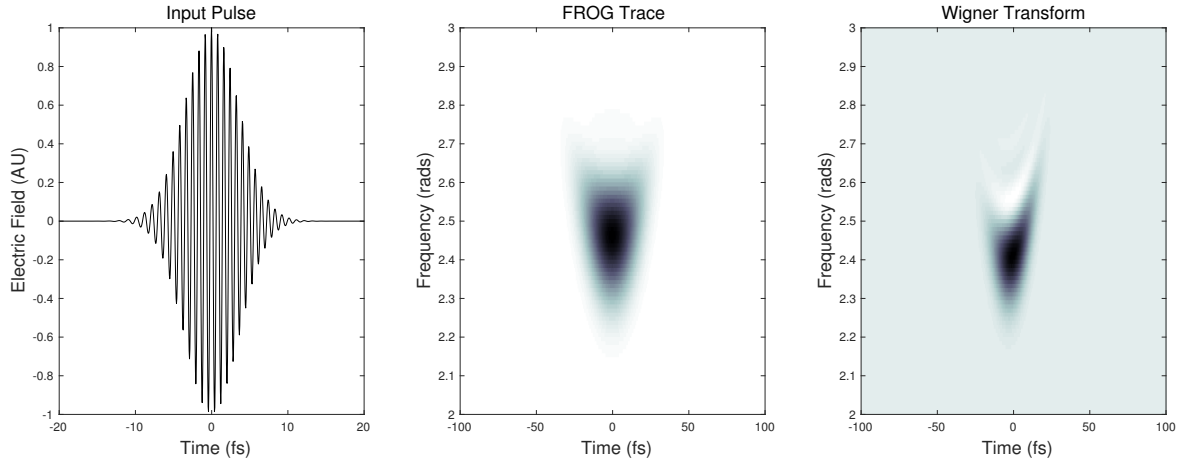


Figure 3.4: The difference between a FROG trace and a Wigner transform. The chirped input electric field is shown on the left, with the corresponding FROG trace and Wigner transform given in the middle and right respectively.

When dealing with ultra-short laser pulses, Wigner transforms [91] offer an intuitive method of visualising the electric filed in the frequency-time space. A Wigner transform is defined as:

$$W(\tau,\omega) = \int_{-\infty}^{+\infty} E(t+\tau)\, E(t-\tau) \exp(-i\omega t) dt \tag{3.8}$$

where the spectrum and intensity are given by $S(\omega) = \int W(\tau,\omega)d\tau$ and $I(\tau) = \int W(\tau,\omega)d\omega$ respectively. Thus, a Wigner transform allows for the properties of the pulse (such as FWHM

temporal duration or chirp) to be visually observed from the distribution map of the pulse, a feat not possible from a FROG trace, as shown below in Figure 3.4.

3.3 Laser Parameters

As the laser is the driver for the laser-plasma interaction, the quality and properties of the laser beam are very important and have large effects on both the electron and ion beams produced. The quality of the focus spot, such as spatial intensity variations and wavefront deformations, as well as laser contrast are two of the main issues encountered experimentally. The quality of the focus spot depends mainly on the parabola optimisation and the beam quality, which can be improved by vacuum spatial filters, deformable optics and a design that reduces aberrations. Experimentally, the focus spot was measured with a magnified camera before every shot to quantify any fluctuations.

Laser contrast, defined as the difference between the peak of the pulse and the pedestal or foot-pulse is another important parameter that affects the efficiency of energy coupling and energies of the accelerated ions. The prepulses are created by various sources such as misaligned compressor gratings, leakage from the regenerative amplifier or amplified spontaneous emission (ASE), and arrive between several picoseconds to several nanoseconds before the peak pulse. Depending on their relative intensity to the main pulse, they can be an issue for ion acceleration as they alter the properties of the target before the interaction with the main pulse. Various methods to reduce the pre-pulse and improve contrast can be used, such as optical parametric amplification (OPA), plasma mirrors or second harmonic generation (SHG). Depending on the ion acceleration regime, different laser polarisations and incident angles are required. The laser seed is generally linearly polarised for ease of amplification and for type-1 phase matching, but certain acceleration regimes such as Radiation Pressure Acceleration (RPA) require circularly polarised light to reduce electron $\mathbf{J} \times \mathbf{B}$ heating. In order to change the laser polarisation without greatly increasing the amount of glass in the optical line (which would cause phase shifts), very thin zero order phase plates are placed close to focus. As many experiments

require normal incidence laser angles, back reflected laser light can become a particular issue when shooting above critical density plasmas. Techniques such as Faraday rotators are used to isolate back reflections, and intermediate focuses and SHG serve to reduce or prevent damage.

3.4 Imaging the laser near field

In order to intercept the laser near field in both transmission and reflection, a scatter screen made of PTFE was placed in the beam within the vacuum chamber and imaged through a window. Due to experimental constraints, it was often difficult to ensure that the screen was placed perpendicularly in the laser beam and imaged face on by the camera. Thus, post processing was required to retrieve the exact laser near field pattern for both the reflected and transmitted beam.

The viewing and interception angle corrections were calculated using a self-written script based on the *fitgeotrans* function in Matlab. As part of the inbuilt Image Processing toolbox, this function works by selecting control points and references them to physical distances. The specified geometric transformation was then inferred using the "projective" method where straight linear are conserved, and converging lines are transformed into parallel lines [92] [93]. The image is therefore transformed to the correct plane. Note, the process includes modifications to the signal levels such that spatial variations in intensity are accounted for. In Chapter 6 this function was used twice, once to compensate for the beam-to-screen angle, then again to compensate for the screen-to-camera viewing angle.

3.5 Simulating laser-plasma interactions

As overdense interactions are extremely difficult to probe due to their high densities and short spatial and temporal scales, numerical simulations were run to gain a better understanding of the temporal and spatial evolution of the plasma in the interaction region. EPOCH [94], a fully relativistic particle-in-cell (PIC) code developed at the University of Warwick was used

to perform the simulations included in this thesis. Run in 2D3V, a 2D cartesian grid was used to spatially locate the particles in the simulation box, whereas the fields were represented in 3D such that the plasma could be assumed to be uniform and continuous in the third dimension. As simulating each individual particle would be too memory and computationally heavy, macro-particles representing around 3.6×10^9 individual particles were used.

Particle motion is determined in the following manner:

1. The Lorenz force is computed for each macro-particle at each grid point and their positions are updated,
2. The new current terms and localised space-charges are calculated on the grid points,
3. The electromagnetic fields are updated on a separate grid using Maxwell's equations. The field grid is offset to the particle grid by half a cell in all directions,
4. The fields at the particle grid points are interpolated,

This process is repeated for every timestep, until the simulation is terminated by the user. The simulations were run on the CX1 super-computer cluster at Imperial College London and were run without ionisation or collisions. Thus each particle species was initialised separately, which enabled the inclusion of contaminants into the bulk of the target, as measured experimentally. The ionisation levels of each ion was calculated by comparing their ionisation potential to the laser intensity.

3.5.1 Resolution

The minimum acceptable spatial and temporal resolution in a PIC code is determined by the Courant condition which prevents electromagnetic fields from growing exponentially in time due to numerical heating [95]. It states:

$$c^2\Delta t^2 < \Delta x^2 + \Delta y^2 \tag{3.9}$$

for a 2D grid, where the cell size is given by Δx and Δy, and the simulation time step as Δt. Additionally, when simulating thin solid targets, resolving the skin depth multiple times

is desirable to get a full and accurate visualisation of particle motion and the associated fields. This also reduces numerical heating and enables a full reconstruction of the rapidly oscillating field of the laser.

3.5.2 Calculating Gamma

The gamma factor of the laser is important in determining the critical density of the plasma at a given time of the laser pulse. This was calculated using the equation:

$$\gamma(t) = \sqrt{1 + \frac{a_0(t)^2}{2}} = \sqrt{1 + \frac{0.855^2}{2} \times (I(t)_{10^{18}\,\mathrm{W\,cm^2}} \lambda_{\mu m}^2)} \tag{3.10}$$

where the intensity is taken as the instantaneous intensity of the laser pulse, and is thus dependent of the time position chosen within the laser pulse.

In EPOCH the laser pulse in initialised as a gaussian laser pulse with electric field E given by:

$$E(r,t) = E_0 \exp\left(-\frac{r^2}{\sigma_r^2}\right) \exp\left(-\frac{t^2}{\sigma_t^2}\right) \tag{3.11}$$

where E_0 is the amplitude of the wave, r and t the distance and time from the centre of the beam, and σ_r and σ_t represent the radius or time where the electric field drops to $1/e$ of the central value. They are related to the more-commonly used experimental terms of r_{FWHM} and t_{FWHM} by:

$$\sigma_r = \frac{r_{\mathrm{FWHM}}}{\sqrt{2\ln(2)}} \qquad\qquad \sigma_t = \frac{t_{\mathrm{FWHM}}}{\sqrt{2\ln(2)}} \tag{3.12}$$

The intensity of the laser pulse can be calculated using the time average of the Poynting vector $\langle \mathbf{S} \rangle$:

$$I(r,t) = \frac{\alpha}{2} c \epsilon_0 E(r,t)^2 \tag{3.13}$$

where c is the speed of light and ϵ_0 the vacuum permittivity and $\alpha = 1, 2$ for linear or circular polarisation respectively. Thus, to find the total energy of a laser pulse, the intensity is

integrated over all space and time:

$$\mathcal{E} = \int_{-\infty}^{+\infty} \int_{0}^{2\pi} \int_{0}^{+\infty} I(r,t) r dr d\theta dt \tag{3.14}$$

A mathematical description of a linearly and circularly polarised pulse is given in Section 2.1.

Chapter 4

Transmission Through Thin Foils: Experimental Results

This chapter presents results from an experimental campaign undertaken on the Astra-Gemini laser of the Central Laser Facility, which ran in February and March 2017 at the Rutherford Appleton Laboratory in Harwell, UK. The experimental campaign was a collaboration between Imperial College London (UK), Queen's University Belfast (UK), The University of Strathclyde (UK), le Laboratoire d'Utilisation de Lasers Intenses at the Ecole Polytechnique (France) and the Central Laser Facility (UK). The aim of the experiment was to explore the optimum conditions for radiation pressure acceleration, by irradiating ultra-thin carbon foils with a high contrast laser pulse. Optical diagnostics looking at the transmitted and reflected light yielded interesting results, providing information on both the interaction dynamics and an indication of the amount of energy absorbed.

This chapter starts with a presentation of the experiment aims, a description of the set-up and an explanation of the diagnostics and calibrations. Secondly, the experimental results are presented and, finally, discussed. The experimental results presented in this chapter are supported by particle-in-cell simulations presented in Chapter 5.

4.1 Motivation

The primary aim of the experiment was to undertake a study of ion acceleration from ultra-thin targets (in the range of 2-100 nm) with a goal to optimise ion energies from the radiation pressure acceleration regime. In these laser and target conditions two acceleration regimes occur: radiation pressure acceleration and relativistic transparency, as described in section 2.4.2. However the plasma conditions in these regimes differ significantly and they produce different ion spectra. Interestingly, these experiments are primarily characterised by particle diagnostics, with little research having been done on optical diagnostics and measuring the quantity of energy coupling into the plasma. With the recent stagnation on progress in achieving ever higher ion energies, a more thorough understanding on the interaction dynamics occurring in the overdense plasma is needed.

As ions are primarily accelerated by electrons, and electrons are the primary absorber of laser light, understanding the dynamics of energy absorption at relativistic intensities and on short time scales is of significant importance for ion acceleration. Laser energy absorption in the relativistic regime has, to-date, only been superficially explored and modelled in overdense plasmas [96] [97]. A general physics model was proposed by Mulser *et al* [98], however it gives only a qualitative overview of the physical processes behind strong absorption. A second theoretical model, exclusively applicable to micron thick targets, was proposed by Levy *et al* and showed that the laser energy absorption into the plasma has minimum and maximum limits for different values of a_0 [99]. Quantitative values based on experimental results can be found in the literature for varying pulse lengths, laser intensities and target thicknesses [63] [96] [97] [100] [101] [102].

Energy absorption occurs from driving electron oscillations along a density gradient, and is therefore expected to be stronger for polarisations that have a component of the electric field directed along the density gradient (i.e. non-normal incidence). The energy absorption factor will have a strong influence on the plasma conditions present during the interaction as strong absorption will entail high thermal pressures and thus fast plasma expansion and electron density decrease [103]. This has been shown to have an effect on the driving laser pulse, with

previous studies showing spectrum broadening and blue shifting due to self-phase modulation from ionisation in an underdense plasma [104]. Additionally, the spatial properties of the transmitted laser pulse have been shown to indicate instabilities in the target and regions of high and low absorption [51]. Thus by combining information obtained from particle diagnostics with that from optical diagnostics, a greater understanding of the plasma interaction can be obtained, helping the pursuit of higher energy ions.

This chapter aims to compliment the literature by presenting results from optical diagnostics from an experimental campaign where ultra-thin targets were irradiated by a short pulse high energy laser with varying polarisations. The results are used to gain a more indepth insight into the plasma dynamics than that possible by only particle data, and are presented below.

4.2 Set-Up

4.2.1 Laser

The Gemini laser system is a Nd-YAG pumped Ti-sapphire laser with a central wavelength of 800 nm and mean pulse length of 47.7 ± 4.8 fs. The mean laser energy measured before the compressor was 15.7 ± 1.9 J, with 4.5 ± 0.54 J delivered on target after a double plasma mirror system. These values were calculated by considering the measurements taken on the laser diagnostics situated before the interaction for all successful shots. A successful shot was defined as the delivered energy lying above 80% of the requested energy as measured by a calorimeter before compression, i.e. above 13.8 J. The laser pulse was then focused using an $f/2$ off-axis parabola down to a focal spot size of $\sim 3\,\mu$m full-width-half-maximum (FWHM), with approximately 24.5% of energy in the FWHM, as measured by dividing the sum of all pixel values above the half maximum by the sum over the whole image. Hence, intensities of around $3.33 \pm 0.67 \times 10^{20}$ W/cm^2 and a maximum a_0 of 12.5 ± 1.3 were obtained. The double plasma mirror system was used to improve the contrast of the laser pulse in order to prevent target heating and expansion before the main interaction. This provided a contrast of $\sim 10^{14}$

at 10 ps for two plasma mirrors, based on a reflectivity of ∼69% each.

A summary of the laser parameters is given in table 4.1 below.

Parameters	Value
Mean Energy on target	4.5 ± 0.54 J
Focal Spot Size	$\sim 3\,\mu$m
Pulse Length	47.7 ± 4.8 fs
Intensity at focus	$3.33 \pm 0.67 \times 10^{20}$ W/cm^2
a_0 at focus	12.5 ± 1.3

Table 4.1: List of experimental parameters used in the Gemini 2017 run.

4.2.2 Experimental Layout and Targetry

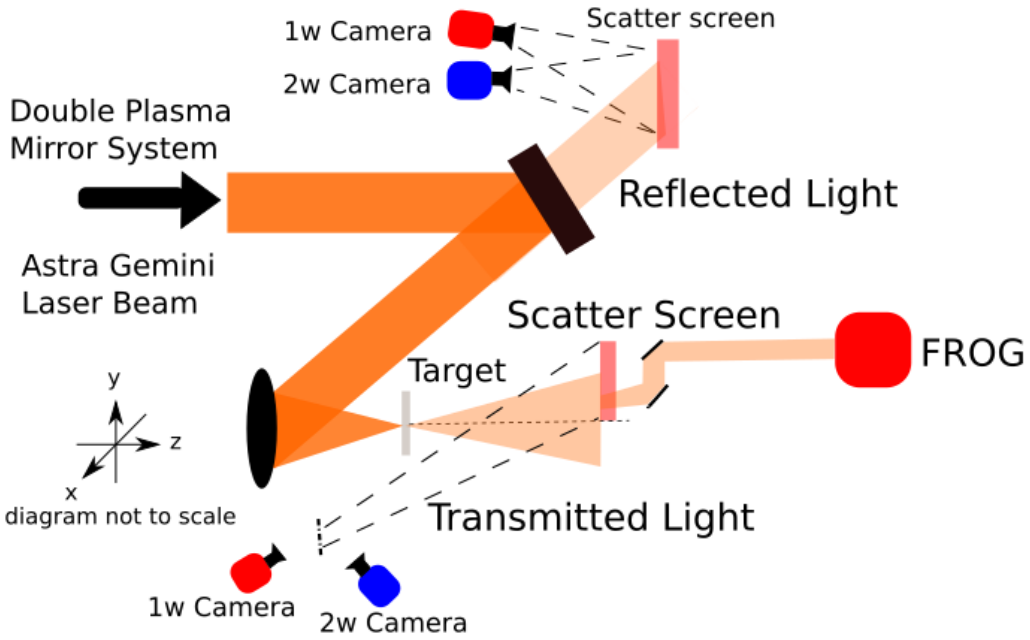


Figure 4.1: The experimental set-up.

The experiment was set up as shown in Figure 4.1, with the diagnostics presented in this chapter shown in red and blue. The transmitted laser light was incident on a scatter screen, which intersected the upper half of the beam. The screen was then imaged with two transmission cameras, as shown in the lower left quadrant. A portion of the transmitted light was captured

by a pick-off mirror through a hole in the transmission screen and directed into the FROG diagnostic. The laser light reflected off the target back propagated through the final turning mirror and was incident onto another scatter screen. This was imaged by two cameras shown in the upper right quadrant. A zero-order, anti-reflectance coated $\lambda/4$ waveplate was used to change the laser polarisation incident on target between linear and circular polarisation.

The targets presented in this chapter are ultra-thin amorphous carbon foils of thickness in the range 2 - 100 nm and mass density 2 g cm^3. The electron density is calculated at 1.2×10^{24} cm^{-3} and the cold skin depth at 5 nm. All targets were shot at normal incidence.

4.3 Diagnostics

4.3.1 Transmitted Light Diagnostic

To diagnose the transmitted light, a scatter screen was placed after the interaction point and imaged with two identical cameras and collection optics through first and second harmonic interference filters. The scatter screen was a 60×30 cm PTFE screen placed 35 cm away from and 1.6 cm above the interaction point. A small 3×3 cm hole, made above the laser $\hat{z}$ axis, was used to place a pick-off mirror in the laser beam for the forward line diagnostics. In order to calibrate the amount of transmitted energy a series of null shots, laser shots with no target placed at the interaction region, were taken. The amount of energy delivered on target was known through a calorimeter and hence, by comparing it to the amount of counts received on the cameras during no target shots, the amount of energy transmitted through the interaction region was calculated. Using this method, all collection effects were taken into consideration such as the scattering effects of PTFE, the partial capture of the transmitted beam and the solid angle of light capture of the cameras. This method assumes an equal distribution of light in the transmitted beam cone. Changes in spectrum were taken into account by putting interference filters of 5 nm bandwidth in front of the cameras. Additionally, null shots of both linear and circular polarisation were taken to account for any polarisation dependent transmission effects.

Upon analysis, no differences between polarisation were found. As null shots are solely in $1\,\omega$, the $2\,\omega$ camera was calibrated by adjusting the $1\,\omega$ calibration to account for increase camera chip sensitivity at 400 nm [105].

The calibration shots are plotted in Figure 4.2, where one count corresponds to approximatively 10^7 photons.

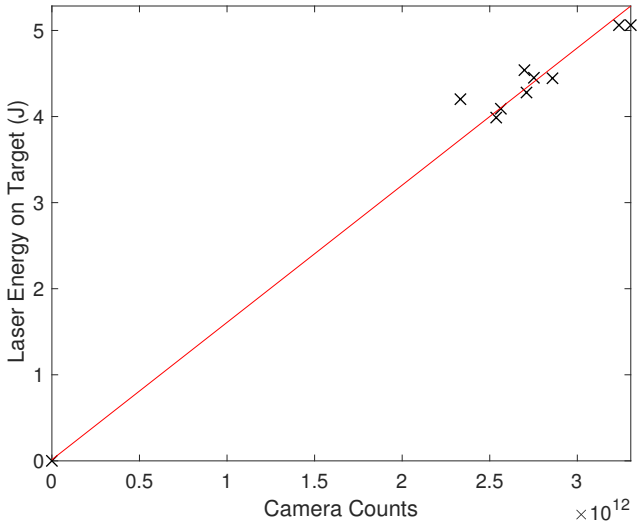


Figure 4.2: Calibration of the 1ω transmission camera. The equation of the line is $y = 1.6\times 10^{-12}\ \times$counts $+0.014$

4.3.2 Reflected Light Diagnostics

The reflected light was diagnosed by collecting the leakage though the penultimate dielectric turning mirror, as shown in Figure 4.1. Already collimated by the parabola, the light was telescoped down first using a 10 cm diameter lens, then a 2 inch diameter lens, before propagating onto a scatter screen in the near field. The screen was then imaged in the same manner as the transmission diagnostic, with two cameras with $1\,\omega$ and $2\,\omega$ interference filters of bandwidth 5 nm. The spectral transmission of the dielectric turning mirror was calibrated using a white light source and a spectrometer. Due to an inconclusive calibration, absolute values of reflected energy were not retrievable. However, relative measurements can still be used to identify experimental trends.

4.3.3 Transmitted FROG

A GRENOUILLE, a type of FROG described in section 3.2.1, was used to determine the temporal and spectral properties of the transmitted laser pulse. As shown in Figure 4.1, a 1 inch spherical pick-off mirror placed 37.5 cm behind the interaction region collimated a 20 mm diameter beam before redirecting it out of the chamber through a 2 mm thick fused silica window with total GVD of $72.3\,\mathrm{fs}^{-2}$. The GRENOUILLE used was a 8-20-USB Swamp Optics SHG-FROG with temporal sensitivity of 0.861 fs/pixel, spectral sensitivity of 0.0841 nm/pixel and a resolution of ≈ 8 fs. A calibration performed in the laser front end was used and the experimental set-up effects, such as the added GVD from transmission through optical elements, were taken into consideration during the analysis.

As FROGs have an ambiguity in time, an explicit direction for the temporal pulse shape and laser chirp was not available. However, by scanning one independent variable and looking at the Wigner transforms, or by exploiting the large asymmetry in temporal intensity and phase, one can retrieve the direction of time. This is further explained in section 4.6.

A small dynamic range, due to the second harmonic production, and a varying laser energy resulted in a large number of saturated or low signal shots being discarded from analysis. The discarded shots present no additional features and thus provide no indication of a secondary trend not shown by the accepted FROG traces. Only traces with valid signal levels, valid retrievals and retrieval error (See section 3.2.2) below 2% were included in the analysis. In order to increase accuracy, the retrieval algorithm was run 10 times on each FROG trace, with the range of values obtained used to calculate the overall error in the retrieved pulse length. Errors due to resolution and measurements were also calculated, but were found to be insignificant compared to the retrieval errors.

4.4 Experimental Results from the Transmission Screen

The PTFE screen was used to scatter the transmitted laser light for re-imaging, giving information on the spatial structure of the laser pulse as well as the amount of energy transmitted. Hence, the changes in spatial structure and the quantity of transmitted light will be reported on separately.

4.4.1 Transmitted Beam Spatial Profiles

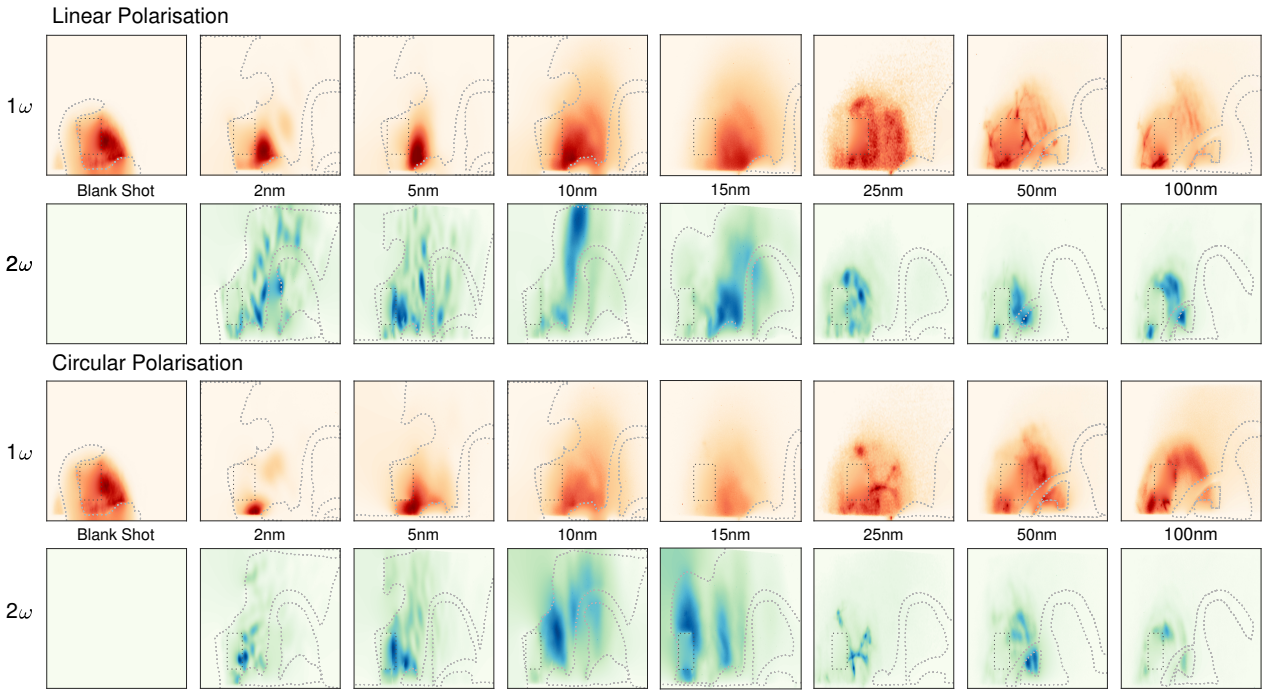


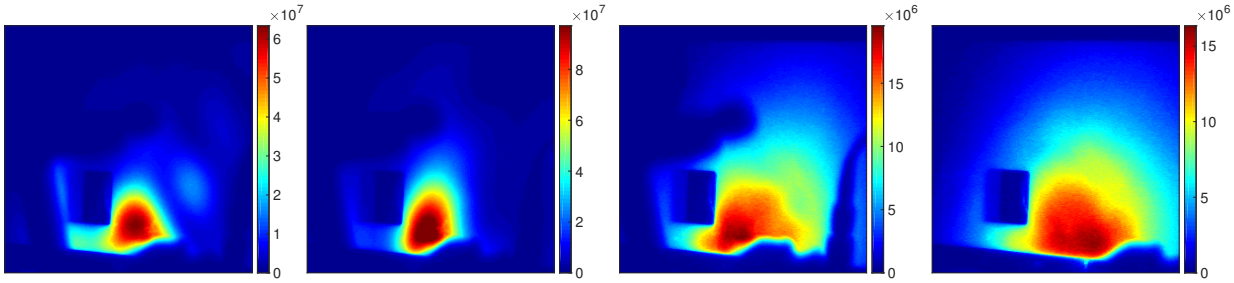
Figure 4.3: Raw images of the transmitted beam profile for different target thicknesses, harmonics and polarisations. The images are displayed on a linear colour scale such that the spatial profiles can be seen more clearly. The colour scales therefore do not account for the amount of filtering used. The spatial scale of each image is identical, and corresponds to a $60 \times 30\,\mathrm{cm}$ field of view.

Concentrating firstly on the variations of the spatial structure of the beam, Figure 4.3 shows images of the transmitted beam for the full range of target thickness, including a shot with no target, in both $1\,\omega$ and $2\,\omega$ light. The images, presented on a linear colour scale with their individual dynamic ranges maximised, have been rotated and modified to compensate for the cameras viewing angle. Additionally, non linear interpolation was used to compensate for partial obstruction in the field of view by other experimental diagnostics. There areas are

delineated by the dashed silver lines and correspond to the pick-off mirror for the transmitted FROG and an imaging lens.

By observing the spatial structures for increasing target thickness, the primary observation to be made is the difference in spatial structures shown between the thinner targets of thickness range 2 - 15 nm and the thicker targets above 25 nm. In the first harmonic, the thinner targets show a distinct region of higher irradiation with a smooth spatial profile that varies radially. In comparison, the thicker targets show significantly modulated radiation within the laser cone in addition to a weak background. In the second harmonic, strong spatial modulations are seen over the whole PTFE screen for the thinner targets, whereas the modulated radiation is confined to the laser cone angle for thicker targets.

To enable direct comparisons, the counts of the raw images were adjusted to account for filtering, and are shown in Figure 4.4. Here, the spatial profiles of targets irradiated by a linearly polarised laser pulse are shown for thicknesses 2 - 15 nm and for the first harmonic. A clear trend of increasing spatial area of irradiation with a decrease in maximum intensity (as can be seen through the varying colour bars) is visible for increasing target thickness. For circular polarisation, a similar behaviour is observed, as seen in Figure 4.3, with the spatial beam profile increasing in divergence for increasing target thickness. By contrast, the spatial profile of the second harmonic light emitted from targets in the thickness range 2 - 15 nm shows little variation over target thickness, with consistent strong modulations over the whole scatter screen.

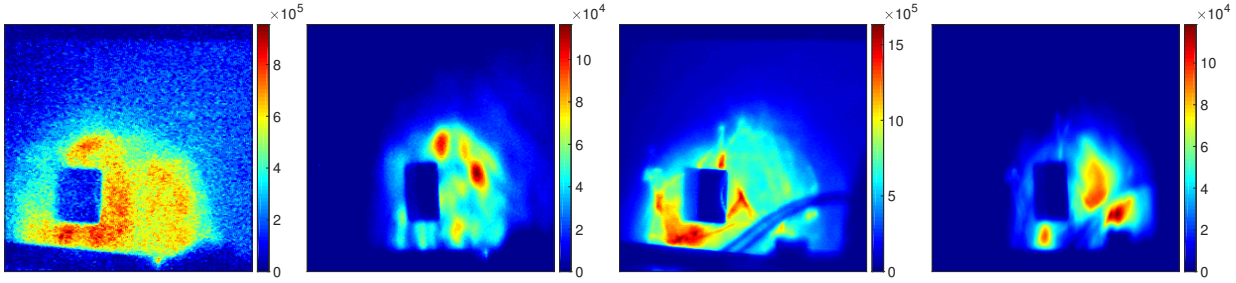


(a) 2 nm (b) 5 nm (c) 10 nm (d) 15 nm

Figure 4.4: The spatial profiles in the first harmonic of the thinner targets irradiated by a linearly polarised laser pulse. Figures shown on a varying linear colour scale.

For targets of thickness 25 nm and above, the spatial beam profile of the transmitted light,

as shown in Figure 4.5a and Figure 4.5c, changes significantly in both structure and intensity from those seen in Figure 4.4. For both harmonics shown in Figure 4.5 a significant decrease in intensity by over an order of magnitude is seen in the transmitted light as compared to thinner targets. For the first harmonic, the radiation is located in the cone of the laser, with strong spatial modulations therein. The second harmonic sees a similar shift with spatial modulations more circular in shape. No correlation between first and second harmonic spatial profile can be seen.



(a) 25 nm 1 ω (b) 25 nm 2 ω (c) 50 nm 1 ω (d) 50 nm 2 ω

Figure 4.5: The spatial profiles in the first and second harmonic of the thicker targets irradiated by a linearly polarised laser pulse. Figures shown on a linear colour scale.

4.4.2 Energy Transmitted

In addition to providing spatial information on the dynamics of the interaction, the scatter screen is able to provide quantitative results on the transmitted energy. Figure 4.6 gives the percentage of on-target laser energy transmitted through the plasma as a function of target thickness. Note both axes are logarithmic and the errors represent the standard deviation in the transmitted energy values obtained for each different data shot. The errors in measurement were found to be negligible compared to the fluctuation in results. For the target thicknesses where only one shot was taken, the error bars are not visible on these axes.

Looking first at the fundamental laser frequency, the amount of transmitted light for thinner targets ($\leq$15 nm) is almost an order of magnitude greater than for thicker targets ($\geq$25 nm) for both laser polarisations. The trends are not linear, with a distinct change in transmission around 25 nm and little variation between 10 - 15 nm. The two polarisations follow different

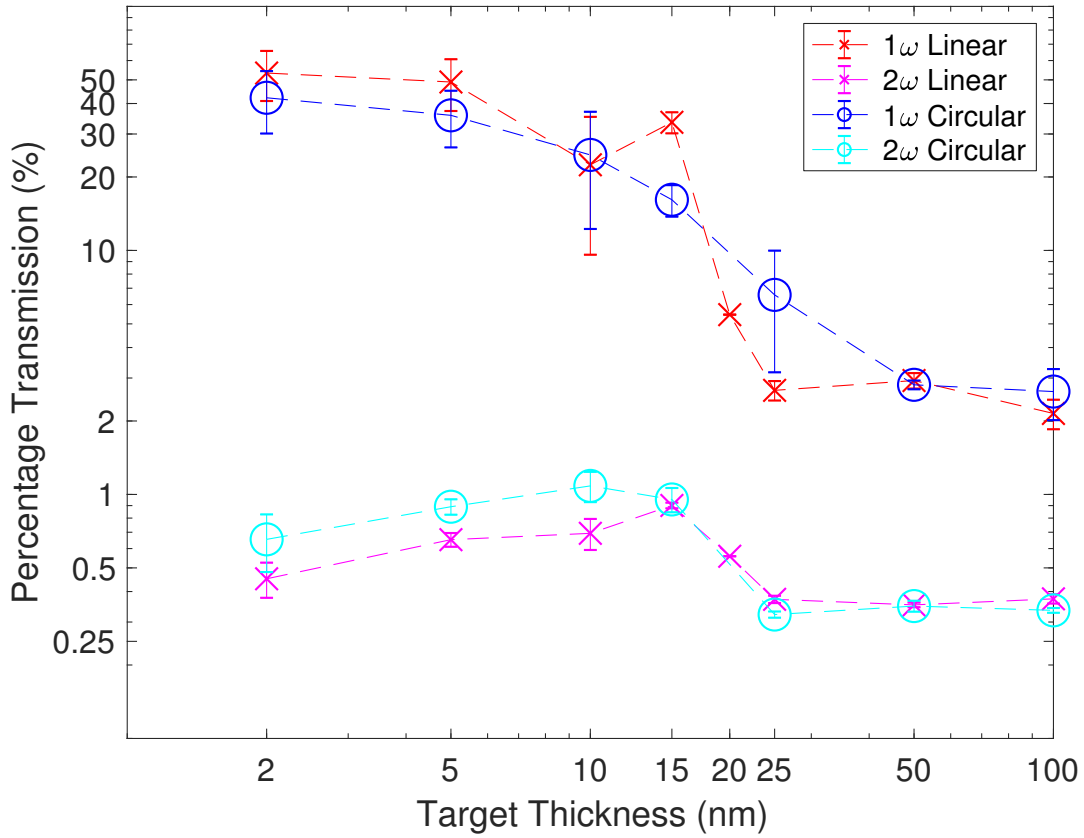


Figure 4.6: The mean transmitted energy for linear and circular polarisations as a function of target thickness

trends, with the circular polarisation following a smooth trend and linear polarisation experiencing a much stronger and almost step like change around the same range of target thickness as the $1\,\omega$ circular. For thinner targets, a linearly polarised laser pulse produces more $1\,\omega$ transmission. Interestingly this is not the case for all target thicknesses as a cross over between polarisations can be seen for targets $\geq 50\,\text{nm}$. However, due to the limited range of target thicknesses, this trend would need to be confirmed with thicker ($>100\,\text{nm}$) targets.

The second harmonic light differs from the first harmonic as it must be produced in the plasma and propagate in the forward direction. With this in mind, it is clear to see it follows a different trend with target thickness, though interestingly maintaining the step like change in transmission around 15 - 25 nm. Only a small percentage of the laser energy on target is converted into second harmonic, with production peaking at 10 - 15 nm. For thinner targets, circular polarisation produces a greater amount of second harmonic light, whereas for thicker

targets, little difference between polarisations exist. Interesting to note is the offset in peak second harmonic production between polarisations. For circular polarisation the peak in second harmonic production is seen at thinner targets (10 nm) compared to linear polarisation (15 nm).

4.4.3 Discussion and Summary of Transmitted Light

Drawing on the experimental results presented above, the following conclusions about the physics occurring during the laser plasma interactions can be made.

For the thinnest targets of 2 nm and 5 nm, the target width is of the order of the skin depth, and hence the laser pulse is able to propagate as an evanescent wave to the back surface, rapidly heating the electrons in the focal region and throughout the full depth of the target. Due to the combined effect of relativistic hot electrons and target expansion on the rear surface from thermal pressure, the plasma density decreases below the relativistic critical density and becomes transparent. The remainder of the laser pulse is then guided through the relativistically underdense plasma. Thus a large amount of laser energy is transmitted, as shown in Figure 4.6, with a low divergence, high intensity beam, as seen in Figure 4.3. Second harmonic radiation is produced in the strong density and intensity gradients occurring in the underdense channel, and the laser pulse diffracts upon exit with a divergence inversely dependent on the guided spot radius.

Similar effects occur for targets in the range 10 - 15 nm. However due to the increased target width a larger amount of laser energy is necessary to make the target go relativistically transparent. Thus, as target thickness increases, smaller spatial regions of the target are able to achieve transparency, corresponding to the highest regions of intensity of the focal spot. This effect is also temporally delayed, leading to less time-integrated energy transmitted, and explaining the reduction in transmitted energy seen in Figure 4.6. With a large part of the target remaining opaque, the transmitted laser pulse experiences a decreasing pinhole size for increasing target thickness. This causes the transmitted beam to diffract more strongly upon exiting, as seen in Figure 4.3. Thus, the size of the guided laser spot is inversely proportional to the target thickness, with thinner targets having a larger guided spot radius. The resultant

spatial profile is smooth, with fewer small sized features, in continuation of the trend seen for the 2-5 nm targets.

Second harmonic radiation is again produced in the relativistically underdense channel, with higher densities, gradients and intensities leading to an increased efficiency of $2\,\omega$ production. Thus for thin targets in the range of 2 - 15 nm, the targets experience relativistic transparency at varying times during the laser pulse, with the quantity of laser energy coupled to and transmitted through the target proportional to its thickness.

For 25 nm, both the first and second harmonic spatial profiles change significantly implying different plasma conditions and thus a change in the interaction dynamics. The radiation is strictly confined to the laser cone angle and shows spatial modulations. This differs from the smooth beams produced through diffraction and thus, combined with the change in trend seen for thinner targets, implies a change in plasma conditions. For the thickest targets of 50 and 100 nm, a similar spatial profile to the 25 nm can be seen but with a decreased amount of "transmitted" energy. This quantity differs little between both target thicknesses, supporting the theory of no direct laser transmission. Thus, as the thicker targets no longer follow the previous trend of decreasing amount of transmitted laser light due to a temporal delay in transparency, the radiation must originate from a secondary source of radiation on the targets rear surface. A radiation source that emits in both harmonics, in the forward direction and in the laser cone is Coherent Transition Radiation (CTR), as described in Section 2.5.3. CTR arises from hot electrons escaping the rear surface of solid targets, and has been observed experimentally before [106]. The electrons escaping the target cause dipoles in the formation zone on the rear surface to radiate, as explained in Section 2.5.3. The frequency of electron bunches accelerated on the front surface determines the frequency of emitted light [84], with $1\,\omega$ produced by electrons accelerated through resonance or vacuum heating, and $2\,\omega$ light emitted from $\mathrm{J} \times \mathrm{B}$ heating. The electrons are produced by a non-idealistic focal spot on the target's front surface, and are expected to travel through the overdense plasma in filaments [107] [108]. As no direct studies of such effects for targets in the $<$100 nm and $<$50 fs pulse length range have been conducted, the exact cause of filamentation could not be determined (resistive filamentation [109], Weibel instability [110]). However, filaments the same order of

magnitude as the focal spot are expected [111]. Thus, electron filamentation causing a localised increase in CTR emission could explain the localised hot-spots seen experimentally in Figure 4.5.

Additionally, the strength of CTR radiation is inversely proportional to target thickness and dependent on the fast electron temperature and the scale length at the rear of the target [112]. Bellei *et al* concluded that thicker targets result in more electron straggling so less coherence at the rear surface, with an exponential relationship between emitted CRT power and target thickness, for a constant electron energy [84]. Thus, for different polarisations, a balance between factors described above must be obtained, with the quantity of radiation produced for a 25 nm target expected to be greater than for the 50 - 100 nm targets. Both of these arguments are in agreement with the results presented in Figure 4.6.

To conclude, for thin targets the high percentage of transmission coupled with a smooth spatial profile points towards the target going relativistically transparent at early times during the laser pulse and a pinhole forming. At 25 nm, the spatial profile changes and the quantity of transmitted light greatly decreases implying the target remains relativistically overdense for the duration of the interaction. For these thicker targets radiation is likely to be emitted from the target's rear surface, with the possible source being CTR.

4.5 Experimental Results from the Reflection Analysis

A similar set up using two cameras and interference filters was used to diagnose the near field of the back reflected light through the leakage of a turning mirror (See set-up diagram 4.1).

4.5.1 Reflected Beam Spatial Profiles

Concentrating firstly on the variations of the spatial structure on the near field of the beam, Figure 4.7 shows raw images of the reflected beam for increasing target thickness in both $1\,\omega$

and 2ω light. Note the consistent circular beam shape from clipping due to a sub-aperture lens, thus only the spatial features inside the beam will be analysed.

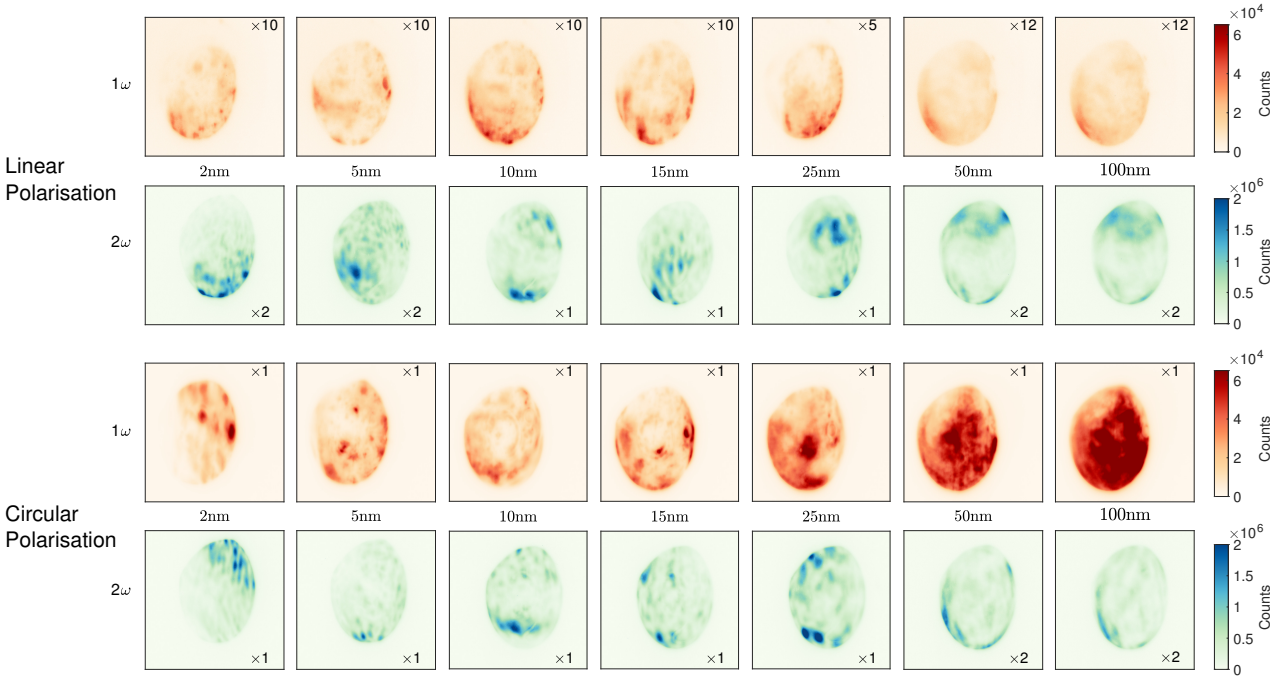


Figure 4.7: Raw images of the reflected beam profile for different target thicknesses, harmonics and polarisations. Note the circular shape comes from using a sub-aperture lens and, in order to put every image on the same colour scale, the respective intensities have been multiplied by the shown factor.

The most striking difference in reflected beam spatial profiles occurs between the two polarisations, with reflectivity being much higher for a circularly polarised laser pulse than for linear polarisation. The reflectivity of the fundamental laser wavelength increases with increasing target thickness for both incident polarisation states. In comparison, the second harmonic trend is different; the reflectivity of both polarisations remains almost constant, with a small visible increase around 10 - 15 nm.

Increased reflection can be seen around the outside of the beam profiles, which corresponds to an increase in absorption in the centre. In particular, the beam profiles of thinner targets show local areas of increased reflectivity, with high frequency components. In comparison, the spatial modulations become smoother, and hence of lower spatial frequency, for increasing target thickness in both harmonics.

4.5.2 Energy Reflected

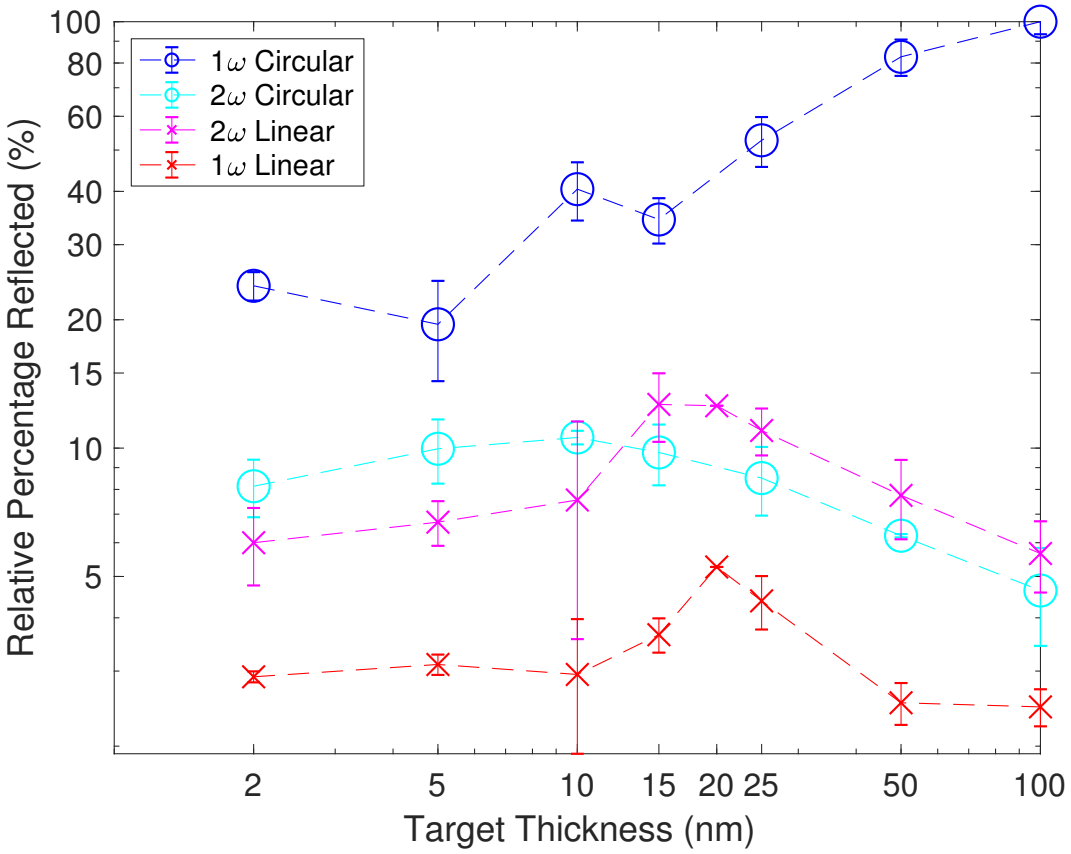


Figure 4.8: The relative reflected energy for linear and circular polarisations as a function of target thickness.

Figure 4.8 shows a relative measurement of back reflected light for both first and second harmonic in linear and circular polarisation. As no absolute measure of reflected energy was possible, the plot has been normalised to the magnitude of $1\,\omega$ reflected light for the 100 nm target. Again, the errors shown are the standard deviation in the transmitted energy values obtained for each different data shot as the errors in measurement were found to be negligible compared to the fluctuation in these results.

The plot shows clearly that, for the laser's fundamental harmonic, circular polarisation causes the target to be substantially more reflective than linear polarisation, with reflectivity dropping as the target becomes thinner. Interestingly, the trend for a linearly polarised laser pulse is different, with a gentle increase in reflectivity around 20 nm. The second harmonic is also unusual, with the circularly polarised light reflected back more strongly than linearly polarised

light for thinner targets, and the cross over between polarisations occurring around 15 nm. The 2ω production for both polarisations peak at the same target thickness in reflection as in transmission, with significant decreases at the extremities of the thickness range.

4.5.3 Discussion and Summary of the Reflected Light

The reflection diagnostic provides additional information on the dynamics of the interaction and, coupled with the transmission data, provides a greater insight into the physical processes occurring during the interaction.

Starting with the first harmonic and with linear polarisation, for increasing target thickness the quantity of transmitted light decreases whereas the reflectivity of the target remains within the same order of magnitude. Thus, this implies that the energy coupled into the plasma increases for thicker targets (≥ 25 nm). By comparison, for circularly polarised light and for increasing target thickness, the transmitted energy decreases however reflectivity increases. This can be explained through less target heating, as the $\mathrm{J} \times \mathrm{B}$ heating mechanism is heavily suppressed and thus the target remains overdense for a longer period of time, with a steeper density gradient and a lower temperature plasma. Hence, less energy is coupled into the thicker targets for circular than for linear, making circular polarisation attractive to those pursuing radiation pressure acceleration.

As in transmission, the second harmonic must be produced in the plasma, and in this case propagate in the backwards direction. The main method of second harmonic generation (SHG) in overdense plasmas and in the backwards direction is thought to be through the relativistic oscillating mirror method, as described in Section 2.5.2. In this case, the targets front surface oscillates at multiples of the laser frequency, causing high harmonic generation. The quantity of second harmonic light depends on the density scale length of the target, and the temporal duration the target remains overdense. As such, one would therefore expect the quantity of second harmonic light to increase from 2 nm targets until the target remains continuously overdense. This is indeed what is seen in Figure 4.8. Once the target becomes thick enough to remain overdense for the duration of the laser pulse (≥ 25 nm), the efficiency of 2ω production

is expected to depend on the density scale length only. Interestingly, Figure 4.8 shows a clear decrease in efficiency of second harmonic production on the front surface with increasing target thickness. This may indicate that for thicker targets ($\geq 25\,\mathrm{nm}$), the density scale length is too short for efficient harmonic generation. For both transmission and reflection, the peak $2\,\omega$ production for circularly polarised light is offset to thinner targets in comparison to linearly polarised light. Knowing that the target experiences less heating for circularly polarised light, due to suppressed $\mathrm{J} \times \mathrm{B}$ heating, it can be concluded that the production of $2\,\omega$ radiation depends significantly on density scale length, and thus also on plasma temperature [113].

Finally, in both harmonics, a homogeneous spatial structure implies a more stable target in the focal plane of the laser. As target thickness decreases, higher frequency spatial modulations are introduced into the spatial structure, showing varying regions of increased absorption and hence decreased reflectivity. Thinner targets remain over dense for the shortest of periods, hence they are more susceptible to spatial variations in intensity, accentuated by the quality of the laser focal spot, which will significantly affect the laser-plasma interaction and the target expansion.

4.6 Experimental Results from the FROG

FROGs are an interesting diagnostic to run on thin foil experiments as, by comparing the incident laser pulse to the transmitted pulse, the effect of the plasma on the laser pulse's spectral and temporal properties can be inferred. In particular for this experiment, where the target thicknesses lie in the range of relativistic transparency, a strong variation in transmitted pulse length is expected due to plasma shuttering, where the plasma transitions from an opaque medium to a relativistically transparent one, effectively acting as a shutter [55]. A strong effect in the spectral domain is also expected, with significant blue shifting seen for pulses propagating through an underdense plasma [104].

Note in this experiment only one FROG was used. Therefore the direction of time and hence the sign of chirp is not directly given by the diagnostic. However, as an asymmetric temporal

envelope is expected due to the optical shuttering, the sharp rising edge can be identified, thus directing the pulse in time. Additionally, a parameter scan over target thickness was conducted, and by observing the Wigner transforms of each pulse, their relative orientation in time was deduced. Finally, the results will be compared to simulations in Chapter 5 to confirm these methods and the analysis.

FROG traces for different target thicknesses are shown in Figure 4.9 with the raw experimental image shown in the upper left corner and the corresponding retrieved FROG traces show in the upper right. In all images, the axis of time is horizontal and the vertical axis is frequency. All traces are symmetric, showing a good spatial profile of the incoming beam. The images are shown normalised to their peak intensity. The temporal and spectral properties of the transmitted pulse are shown in the lower left and right corners respectively, with the intensity plotted in blue and phase in red.

Figure 4.9 shows a clear distinction between the thinner targets of less than 15 nm and thicker targets of ≥ 15 nm. For thinner targets, the transmitted pulses are longer and have a time dependent temporal and spectral phase, shown through a quadratic phase plot, denoting a chirped transmitted laser pulse. For thicker targets, shorter pulses with flat temporal and spectral phases are seen, indicating that they are transform limited, i.e. have no change in frequency over time.

To aid comparison, Figure 4.10a plots the temporal envelope of the transmitted pulse for different target thicknesses. Each pulse has been normalised to it's respective peak intensity in order to better visualise the pulse compression. For thinner targets, the transmitted pulses are significantly asymmetric, with a distinct rising edge and temporal features before and after the rising edge. As the target thickness increases, the pulses become more narrow and more symmetric. The spectral envelopes of the transmitted pulses are plotted in Figure 4.10b with the pulses showing a similar trend as that seen temporally. For thinner targets, the pulses have a significant short wavelength tail, and as target thickness increases this disappears and the pulses become quasi-symmetric.

As a measure of quantitative comparison, the retrieved temporal full-width-half-maximum pulse

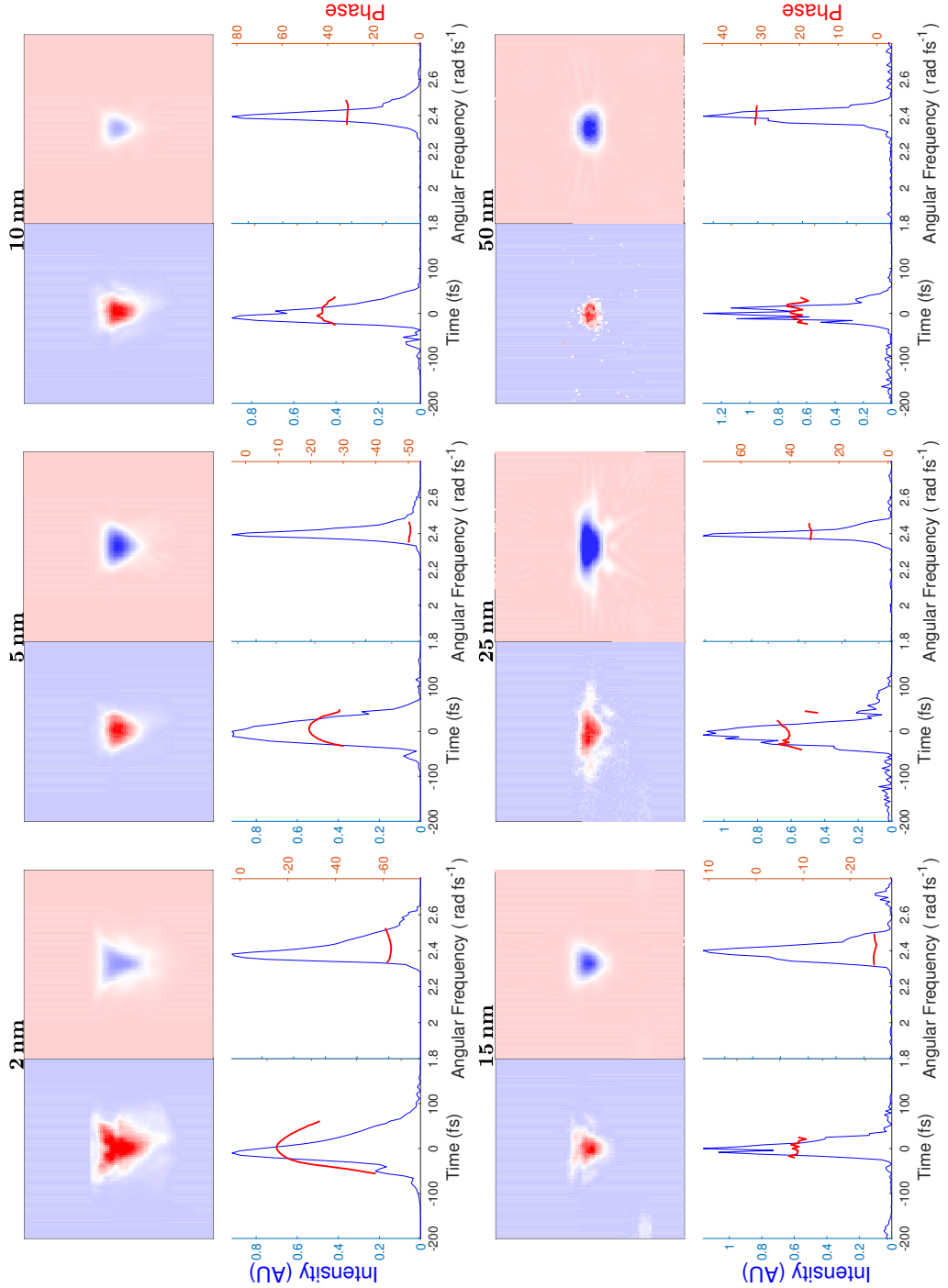
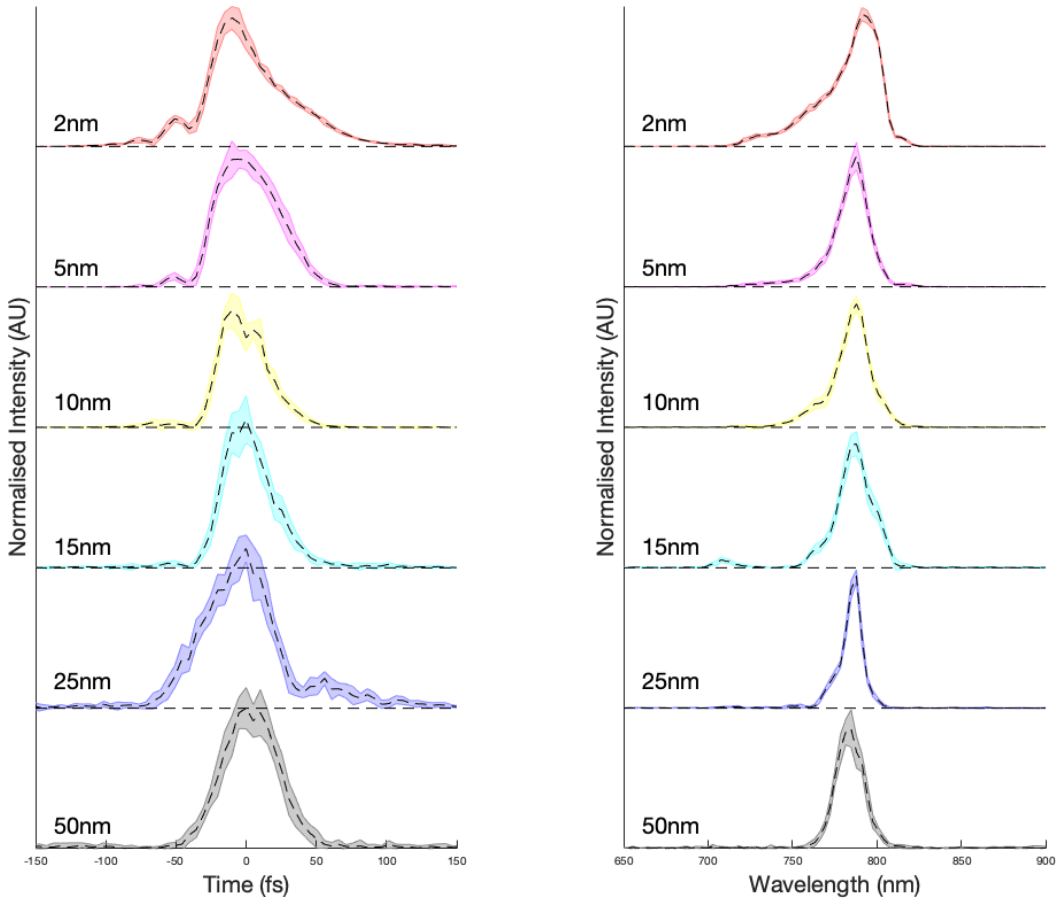


Figure 4.9: The experimental FROG traces obtained for different target thicknesses. For each target thickness, the raw data is shown in the upper left quadrant, and the corresponding retrieved trace shown in the upper right. In these images, the time axis is horizontal, and frequency axis vertical. The lower left quadrant shows the intensity of the temporal envelope, plotted in blue, and the temporal phase, plotted in red. The lower right quadrant shows the spectral intensity and phase, plotted with the same convention. All traces are for linearly polarised shots, except for the 2 nm case which is circularly polarised. Note, for the upper quadrant images, no temporal or spectral scale is given to avoid confusion.



(a) Temporal Envelope (b) Spectral Envelope

Figure 4.10: The temporal and spectral envelope of the transmitted pulse for varying target thickness. The shaded error bars correspond to the range of values obtained from each retrieval, with the median plotted in a black dashed line.

lengths of the data set is plotted against target thickness in Figure 4.11. Linear polarised laser shots are represented by crosses and circular polarised shots by circles. The mean retrieved pulse lengths are plotted with red and blue curves and the standard deviation of the fluctuations in the data set are shown through the error bars. Figure 4.11 shows a clear trend of decreasing pulse length with increasing target thickness, with a small difference between linear and circularly polarised laser pulses. A significant variation in the retrieved pulse lengths can be seen, highlighting the fluctuations in experimental conditions. All pulse lengths are shorter than the incident pulse length, measured pre-interaction to be $\sim 48\,\mathrm{fs}$. For target above 15 nm, only one FROG trace for circularly polarised light was measured.

To analyse the effect of propagation through an underdense plasma of varying refractive index, the temporal chirp of the transmitted pulse was plotted against target thickness, as shown in

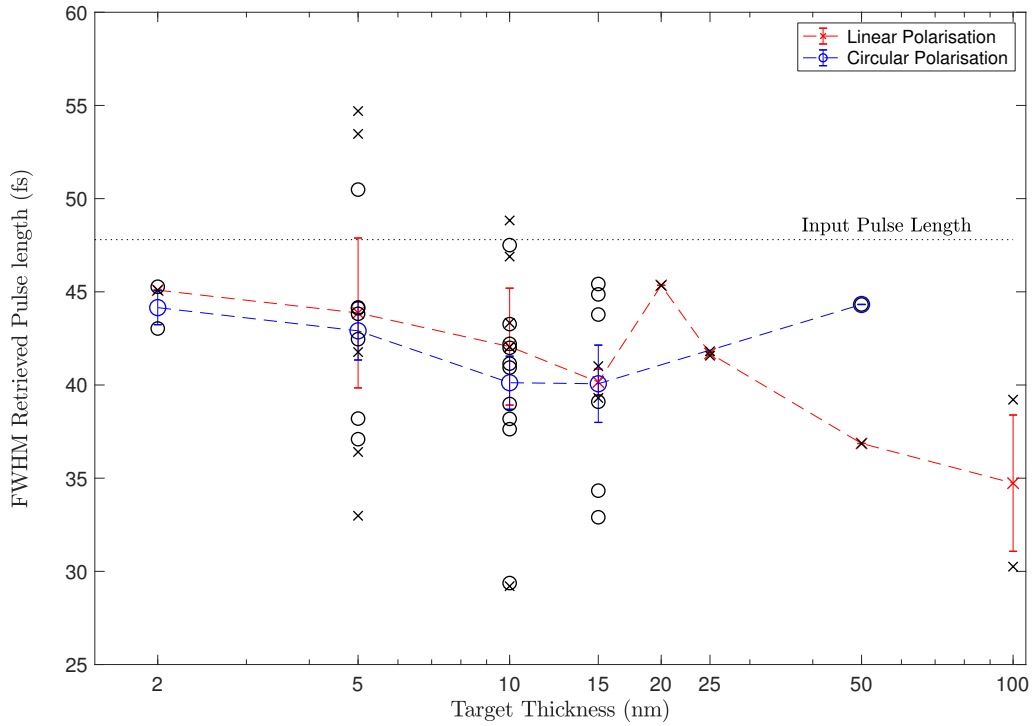


Figure 4.11: The mean FWHM retrieved pulse length with target thickness for each polarisation. For reference, the input pulse length is plotted as a black dotted line. Individual linearly polarised shots are shown with crosses, circular polarisation shown with circles.

Figure 4.12. The individual values of chirp are plotted in crossed and circles for linearly and circularly polarised laser pulses respectively, and the mean absolute value of chirp is plotted in the coloured trend lines. Here, the mean absolute value of chirp, multiplied by -1 to maintain the correct sign, is used to remove any errors produced when manually flipping the pulse in time. From the increased pulse lengths shown in Figure 4.11 and the broadened frequency spectrum in Figure 4.10b, the pulse is expected to be chirped for thinner targets, with the thicker targets remaining near transform limited.

This is indeed what is observed, with thicker targets having almost no chirp and targets ≤ 25 nm having a significant amount of chirp. Both polarisations follow a similar linear increasing trend, until the target thickness approaches the threshold between transparency and opacity. In the region of 15 - 25nm, linear polarisation sees an decrease in chirp whereas circular polarisation respects the existing trend line. Both polarisations tend towards similar values once beyond the threshold, with similar results for the 50 nm target. A lack of data points prevents a statistically

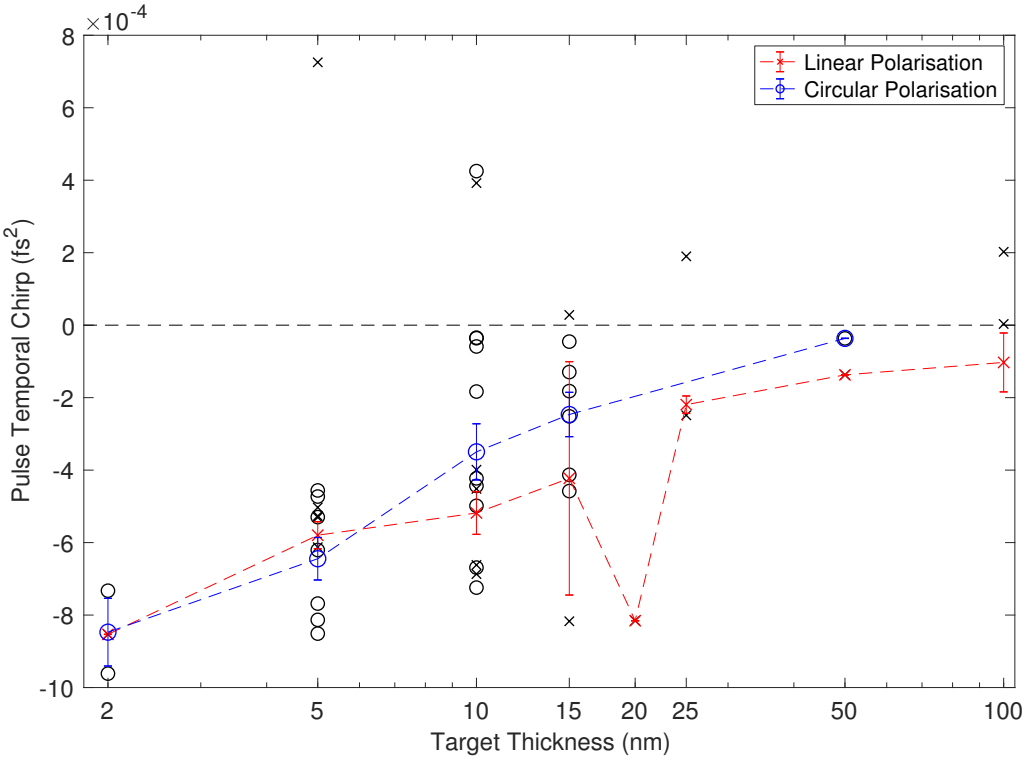


Figure 4.12: The mean chirp of the transmitted pulse against target thickness. Individual linearly polarised shots are shown with crosses, circular polarisation shown with circles.

significant result to be inferred from the region of 20 - 25 nm targets.

While the temporal chirp gives information on the pulse as a whole, it is a scalar and hence gives only an overview on the pulse evolution during the interaction. The instantaneous frequency, defined as the first derivative of the temporal phase, is of particular interest for intense femtosecond pulses as they will be predominantly affected by non-linear effects. In particular, the temporal phase gives information on effects such as self-phase modulation, photon acceleration and plasma shuttering. By taking the first derivative of the temporal phase at each timestep, the instantaneous frequency as a function of time is plotted in Figure 4.13. For each target thickness, the phase values for intensities above $1/e^2$ of the maximum are considered. Note the time axis is arbitrarily centred at the maximum intensity value, and thus is only a relative measurement.

For thinner targets, like 2 or 5 nm, the instantaneous frequency remains positive for a significant duration of time before becoming significantly negative. The magnitude of the instantaneous frequency decreases for increasing target thickness, with 2 nm targets seeing a frequency range

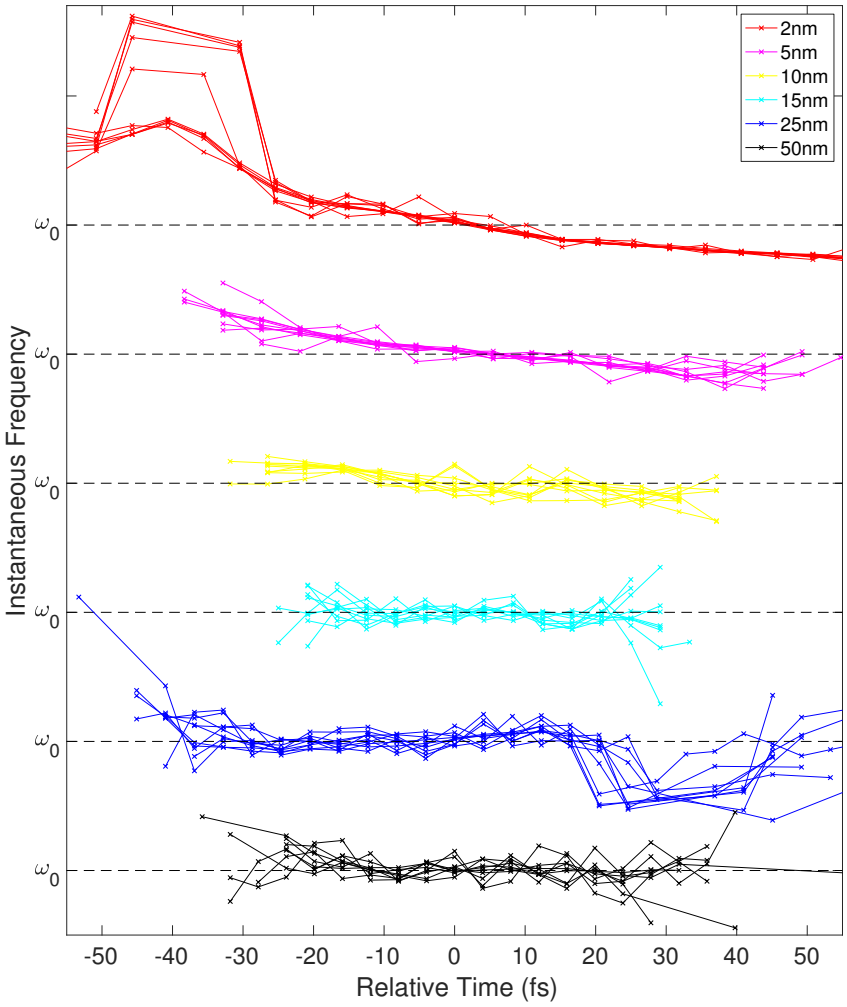


Figure 4.13: The instantaneous frequency with target thickness for each pulse shown in Figure 4.10. For each target thickness, the multiple data lines corresponds to a FROG algorithm retrieval.

of ± 0.8 rad compared to ± 0.2 rad for a 10 nm target. For the 2 nm target, features are seen at early times that are due to low intensity wings of the main pulse. A time varying instantaneous frequency indicates a chirped laser pulse, which occurs when a pulse experiences a time varying refractive index. A decreasing instantaneous frequency indicates a negatively chirped pulse, in agreement with Figure 4.12, where the wavelength increases in time. This results in a red-shifted pulse. Pulse shortening due to increasing target thickness is also visible through the temporal shortening of the plotted results. For thicker targets, the instantaneous frequency of the pulse remains constant at zero for the duration of the laser pulse, implying a flat temporal

and spectral phase. This in turn indicates that the laser pulse has experienced no non-linear effects and has no chirp.

4.6.1 Discussion and Summary of FROG Results

By measuring the temporal and spectral properties of the transmitted laser pulse, more information on the interaction dynamics was obtained, as well as reinforcement to previous arguments. The decreasing pulse length for increasing target thickness, as shown in Figure 4.11, supports the idea of optical shuttering, or temporal delay in transparency, argued above. Linear polarisation was measured to transmit pulses for 5% longer than for circular polarisation, in agreement with the results of the transmission screen stating enhanced energy absorption due to $J \times B$ heating. The transmitted pulses are seen to have significant chirp, which decreases with target thickness, as shown in Figure 4.13. At early times, the instantaneous frequency is positive indicating a decrease in wavelength with time, or blue-shifting of the spectrum through self-phase modulation. This can occur in the target as the density increases either through ionisation or though target compression [89]. At later times, the pulse is seen to experience negative instantaneous frequency, so increasing wavelength with time. This translates as a red-shift in the spectrum, and implies the pulse is transmitting through a medium of decreasing electron density such as a target thermally expanding. For thinner targets that go transparent in the duration of the laser pulse, Figure 4.13 shows the initial target compression due to radiation pressure, then the subsequent expansion due to thermal pressure. The spectral shifts are supported by Figure 4.10b which plots the spectral envelope for various target thicknesses.

For thicker targets, only FROG traces from linear polarisation are obtained, implying a dependence on target heating and thus electron temperature. The spectral and temporal envelope of the pulses are symmetric, with retrieved pulse lengths significantly shorter than for thinner targets. Figure 4.13 shows no change in instantaneous frequency with time, indicating that the pulses originating from thicker targets are unchirped and transform limited. Thus, all factors point towards the radiation originating from the rear surface and not from a transmitted laser pulse, with qualities expected from radiation originating from CTR [84].

Finally, Figure 4.13 shows an interesting trend of decreasing rate of plasma expansion for increasing target thickness, indicated through the gradient of the instantaneous frequency. Thinner targets produce more hot electrons, causing a rapid decrease in target density due to the high plasma temperatures. For thicker targets (15 nm), transparency occurs later on in the laser pulse, and hence during transmission the target sees a lower intensity. A lower laser intensity results in weaker non linear effects on the pulse, resulting in less spectral red-shift at later times.

4.7 Conclusion

To conclude on the results of the diagnostics as a whole, a close correlation in the behaviour of the diagnostics can be seen. The thinner targets experience relativistic transparency, as indicated by a significant amount of transmitted light, shown in Figure 4.6. As the target thickness increases, the onset of transparency is delayed in time thus the quantity of transmitted light decreases, as shown in Figure 4.6. As the targets remain overdense for longer, the reflectivity is greater for circular polarisation at a given target thickness, as shown in Figure 4.8. The FROG results support this theory, with the transmitted pulse lengths decreasing with increasing target thickness, as shown in Figure 4.11. Additionally, thinner targets experience more spectral blue shift from self-phase modulation, as shown in Figure 4.10b, suggesting more of the laser pulse propagates through underdense plasma. Accordingly, this effect translates into an increased amount of chirp for thinner targets, as shown in Figure 4.12. A linear decrease in chirp is seen for pulses propagating through underdense plasma, indicating a time varying refractive index, and thus decreasing electron density, through the plasma.

Upon reaching a target thickness of 25 nm, the spatial profiles of the transmitted pulses change, as shown in Figure 4.3, implying a change in plasma conditions. The quantity of reflected light drops for linear polarisation, with the quantity of transmitted light reducing by an order of magnitude. The temporal and spectral envelope, obtained from the FROG, become more symmetric as well as shorter in time compared to thinner targets. This results in little to no

temporal chirp seen, as shown in Figure 4.12. No added chirp, or GVD, implies no transmission through a medium of varying refractive index and thus the radiation emitted from a 25 nm target can be concluded to not originate from a transmitted laser pulse. This is supported by Figure 4.13, where the instantaneous frequency remains zero for the duration of the pulse.

As the quantity of transmitted light differs little for 50 and 100 nm targets, the trend of decreasing amount of transmitted light for increasing target thickness is broken. The target is no longer considered to go relativistically transparent, as shown in the change of spatial profiles in Figure 4.3. The reflectivity of circularly polarised 1ω light sees a large increase with target thickness where as that of linear polarisation sees a decrease, shown in Figure 4.8. The transmitted FROG traces are significantly shorter in time, almost perfectly transform limited and have very symmetric temporal and spectral envelopes. For 50 and 100 nm targets only FROG traces are recorded for linear polarisation, with one exception for circular polarisation. Thus the evidence points towards this secondary source of radiation being coherent transition radiation arising from the propagation of hot electrons through the target. The spatial modulations in the transmitted beam profiles could then be explained by the inhomogeneous spatial distribution of the electrons that travel through the target as filaments [114] [115]. The suppression of $\mathrm{J} \times \mathrm{B}$ heating for circular polarisation would also explain the lack of FROG traces obtained for circular polarisation.

CTR radiation would be expected to produce transform limited pulses, with bandwidth or range of frequencies inversely proportional to the number of electron bunches produced [84]. This is a result of interference as only radiation at resonant frequencies will interfere constructively; the off resonance frequencies emit incoherently and thus experience destructive interference that becomes stronger as the number of interfering fields increases. Thus, the FROG gives a temporal measurement of the heating mechanism creating the high energy electron bunches and an indication of the electron bunch structure produced.

Secondly, by using both linearly and circularly polarised laser pulse, a study on heating mechanisms could be conducted. For circular polarisation, $\mathrm{J} \times \mathrm{B}$ heating is heavily suppressed as the drift velocity of the electron from the ponderomotive force scales as a constant and not like

$v_{drift} = 1/2\, a_0^2\, c$ as it does for linear polarisation. By comparing the $1\,\omega$ transmission curves in Figure 4.6, the effect of $\mathrm{J} \times \mathrm{B}$ heating can be seen to increase the transmission by over 10%. This can be understood by enhanced electron heating, leading to a higher temperature plasma and hence greater thermal pressure. This in turn results in a faster rate of plasma expansion, and thus longer temporal duration of the transmitted pulse. This is supported by the results in Figure 4.11 where linear polarisation is shown to have longer transmitted pulse lengths than circular polarisation. Differences in the temporal offset of transparency due to differences in target heating are especially visible in the reflectivity plot, shown in Figure 4.8, where circular polarisation is a factor of ~ 20 times more reflected than linear polarisation.

Finally, by comparing both transmission and reflection curves for the laser fundamental wavelength in linear polarisation it can be concluded that the target absorbs a factor of ~ 50 times more incident laser energy than for circular polarisation, as it is neither transmitted or reflected nor changed into second harmonic. Thus, these targets will achieve higher temperature plasmas with more hot electrons, in turn explaining the strong CTR signals detected by the FROG.

To conclude, this chapter presents an overview of the plasma dynamics occurring in targets on the transition between relativistic transparency. Simulations of this experiment are presented in Chapter 5 to further the understanding of these interactions.

Chapter 5

Transmission through Thin Foils: Simulations

In order to gain a more detailed understanding of the experimental results presented in Chapter 4, 2D3V particle-in-cell (PIC) simulations were performed using EPOCH [94] with parameters matching the experimental conditions. The simulation results were then processed in a similar manner to the experimental ones in order to make comparable graphs and measurements. The experimental conclusions are verified and complimented by the additional insight provided by the simulations, and are presented below.

The simulation parameters are summarised in Table 5.1, where the x direction is taken to be the laser propagation direction, y is the transverse direction and the linearly polarised laser pulse was initialised in the plane of the simulation. The target thickness range matched that used experimentally, and the number of particles per cell was adjusted for each thickness in order to find a compromise between resolution and the simulation run time limit on the supercomputer. The number of particles per cell ranged from 300 to 20, where one macroparticle corresponded to 3.6×10^9 and 24×10^9 particles respectively. The target was initialised at a temperature of 200 eV, and a resolution of 0.6 nm was chosen such that the cold skin depth $l_s = 5$ nm was sufficiently resolved.

Simulation size in x	3 µm
Simulation size in y	10 µm
Number of cells in x	5000
Number of cells in y	5000
Target front surface position	1 µm
Laser pulse length FWHM	48 fs
Laser focal spot size FWHM	3 µm
Peak a_0	17.5
Time of peak intensity at target	44 fs
Electron density, n_e/n_{crit}	685
Initial electron temperature	200 eV

Table 5.1: List of simulation parameters

5.1 Electron Density

Firstly, to gain a general overview of the simulations, snapshots of the electron density for different target thicknesses are plotted for different polarisations in Figure 5.1 and Figure 5.2. As the simulation progresses, the plasma dynamics evolve differently for different target thicknesses.

Starting with linear polarisation and the 5 nm target in Figure 5.1, rapid electron heating and target expansion is seen at early timesteps. A larger electron cloud is present on the target rear surface than on the front surface as the former is not affected by the radiation pressure of the laser. At $t = 27$ fs and within the focus spot, the electron density is shown to have dropped from an initial density of $685\, n_{crit}$ to $\sim 20\, n_{crit}$ showing strong plasma expansion. This density lies above the relativistic critical density of $11\, n_{crit}$ and thus the target remains opaque. A slab of electrons can be seen to be accelerated in the backward direction at $x = -300$ nm with transverse features of ~ 150 nm in size. For the subsequent timestep (32 fs), the electron density in the focal spot region has further decreased to $\sim 10\, n_{crit}$ which now sits below the relativistic critical density of the timestep (for $t = 32$ fs $n_{crit}^{rel} = 13\, n_{crit}$). Thus, the target is relativistically underdense and the laser is able to penetrate the target. At the centre of the interaction region, the target is seen to have been displaced in the positive x direction by

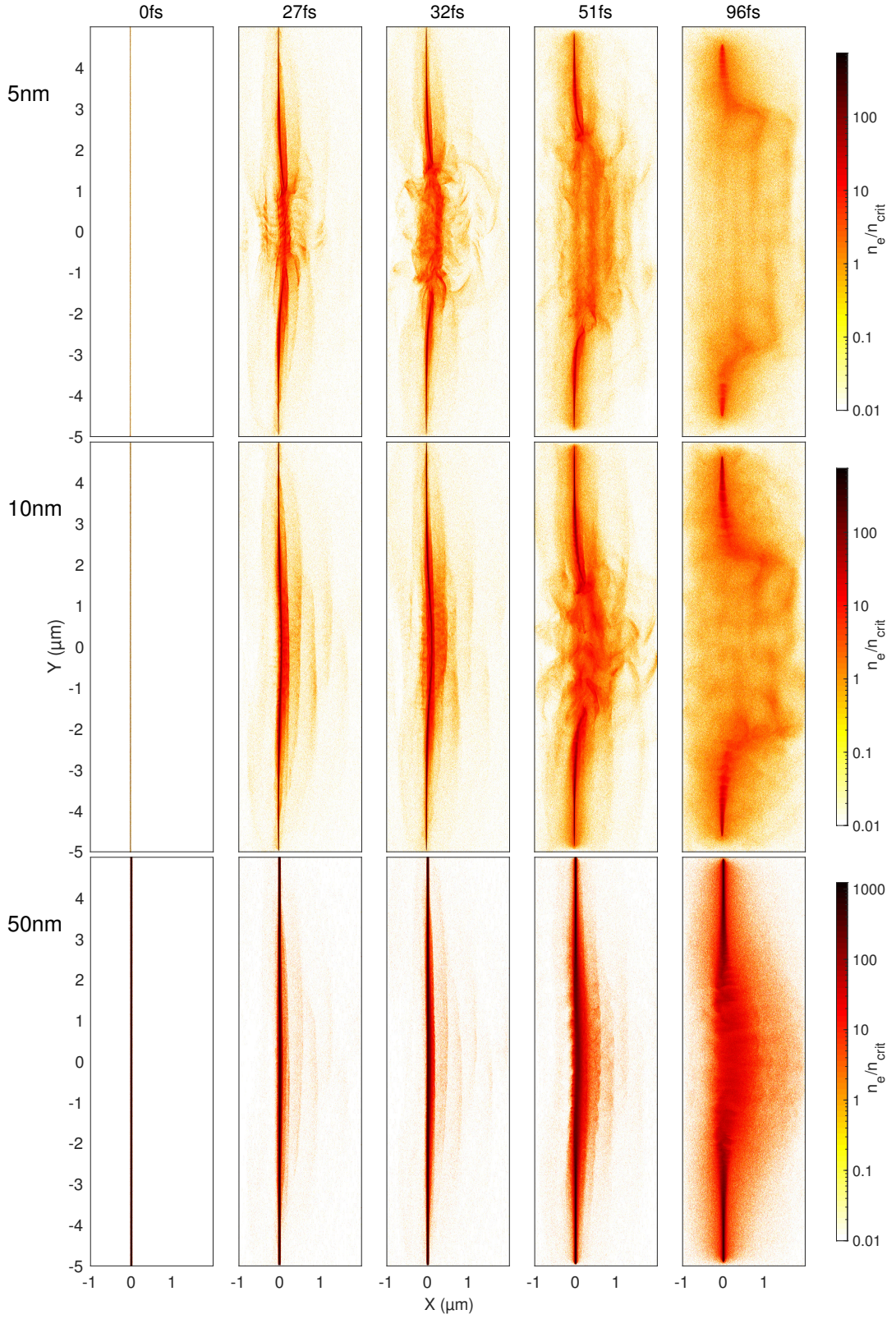


Figure 5.1: Snapshots of the electron density in the simulation box as a function of simulation time, for a 5, 10 and 50 nm target irradiated by a linearly polarised laser pulse.

$\sim 300\,\text{nm}$ and is surrounded by similarly perturbed electron clouds.

At 51 fs, the target remains relativistically underdense and the electron density distribution in the focus spot shows periodic, longitudinal structures at intervals of 400 nm. This can be associated with electrons being accelerated in the laser field by the $J \times B$ force, bunched at twice the laser frequency. In the final timestep (95 fs), the target has expanded further, forming a diffuse electron cloud. A slight periodic pattern symmetric around $y = 0$ can be seen, possibly indicative of the figure-of-8 motion that electrons plot when subjected to the ponderomotive force.

For the 10 nm target, the early timesteps of Figure 5.1 show a target thermally expanding into the vacuum. As with the 5 nm target, the expansion on the front surface is less significant than on the back surface due to the radiation pressure of the laser. Electron bunches of high density ($\sim 1\,n_{crit}$) and small spatial separation ($\sim 400\,\text{nm}$) are accelerated in collimated beams in the forward x direction. This periodic structure corresponds to electron bunches accelerated at twice the laser frequency by the $J \times B$ force. At 32 fs, the target critical surface is shifted in the forward direction. This indicates a slight target buckling meaning the target is no longer normal to the incident radiation. Thus, additional heating mechanisms such as resonant or vacuum heating are able to contribute to the interaction and to the significant changes in plasma conditions seen at the subsequent timestep.

At 51 fs, the electron density in the focal spot has significantly decreased to $\sim 8\,n_{crit}$, thus transitioning to below the relativistic critical density limit (for $t = 51\,\text{fs}$ $n_{crit}^{rel} = 15\,n_{crit}$). More plasma expansion can be seen along with strong spatial instabilities, both longitudinally and transversely, ranging from a few ten to hundreds of nanometres. In the final timestep (95 fs), the target has gone classically underdense, with a diffuse electron cloud remaining. The target material located outside of the focal spot, or at positions of $\mid y \mid > 3\,\mu\text{m}$, also experiences some heating due to the transverse motion of the electrons. This occurs as the electrons in the focal spot are subject to the ponderomotive force, as explained in Section 2.2.6, and thus experience transverse acceleration as well as longitudinal.

For the 50 nm target, less front and rear surface expansion can be seen at early times compared

to the 10 nm target, showing a slower rate of target heating (This will be quantified shortly in Figure 5.4). Electron bunches of lower energy spread than the 10 nm target are accelerated in the forward direction at twice the laser frequency by the $J \times B$ heating mechanism. Their density is similar to the 10 nm target at $\sim 1\, n_{crit}$. This is shown by the single colour electron bunches seen in Figure 5.1. However, it is not until after the peak of the laser pulse (which occurs at 44 fs) that micron scale plasma expansion is seen, with a significant change in density for the bulk of the target. Due to the larger volume of target to heat and greater target mass, little displacement of the critical surface is seen. In the final timestep, the electron density drops to around $\sim 30\, \mathrm{n_{crit}}$, a value that lies above the relativistic critical density. Thus, the target remains overdense for the duration of the laser-plasma interaction. Target material outside of the focal spot also experiences some secondary heating.

Thus, for targets irradiated by a linearly polarised laser pulse, strong target heating and expansion occurs, in particular for thinner targets. Multiple electron bunches are accelerated off the rear surface for all target thicknesses, with the 5 nm and 10 nm targets going relativistically underdense during the laser pulse. In order to compare plasma conditions for different polarisations, a similar figure was produced showing the target evolution in the case of a circularly polarised laser pulse.

For a 5 nm target irradiated by a circularly polarised laser pulse, the initial timesteps in Figure 5.2 shows a slight target buckling in the centre of the focus spot and very little electron heating on the target rear surface. The faint electron cloud differs greatly from the significantly expanded target seen in Figure 5.1 for linear polarisation. Indeed, the target density remains at $\sim 120\, n_{crit}$, in comparison to the $\sim 20\, n_{crit}$ found for linear polarisation. No target expansion is seen on the target front surface at 27 fs or at 32 fs. This is due to the radiation pressure of the laser being dominant over the thermal pressure of the plasma, shown by a target displacement of 250 nm in the forward x direction for the 32 fs timestep. After the peak of the pulse and at $t = 51$ fs, the target buckling is much more obvious with a forward displacement of $\sim 1\, \mu$m. The electron density in the focal spot has dropped to $\sim 2\, n_{crit}$, and thus is relativistically transparent to the laser pulse. The rapid drop in electron density is due to target buckling, which causes a non-normal angle of incidence and enables other heating mechanisms to contribute to

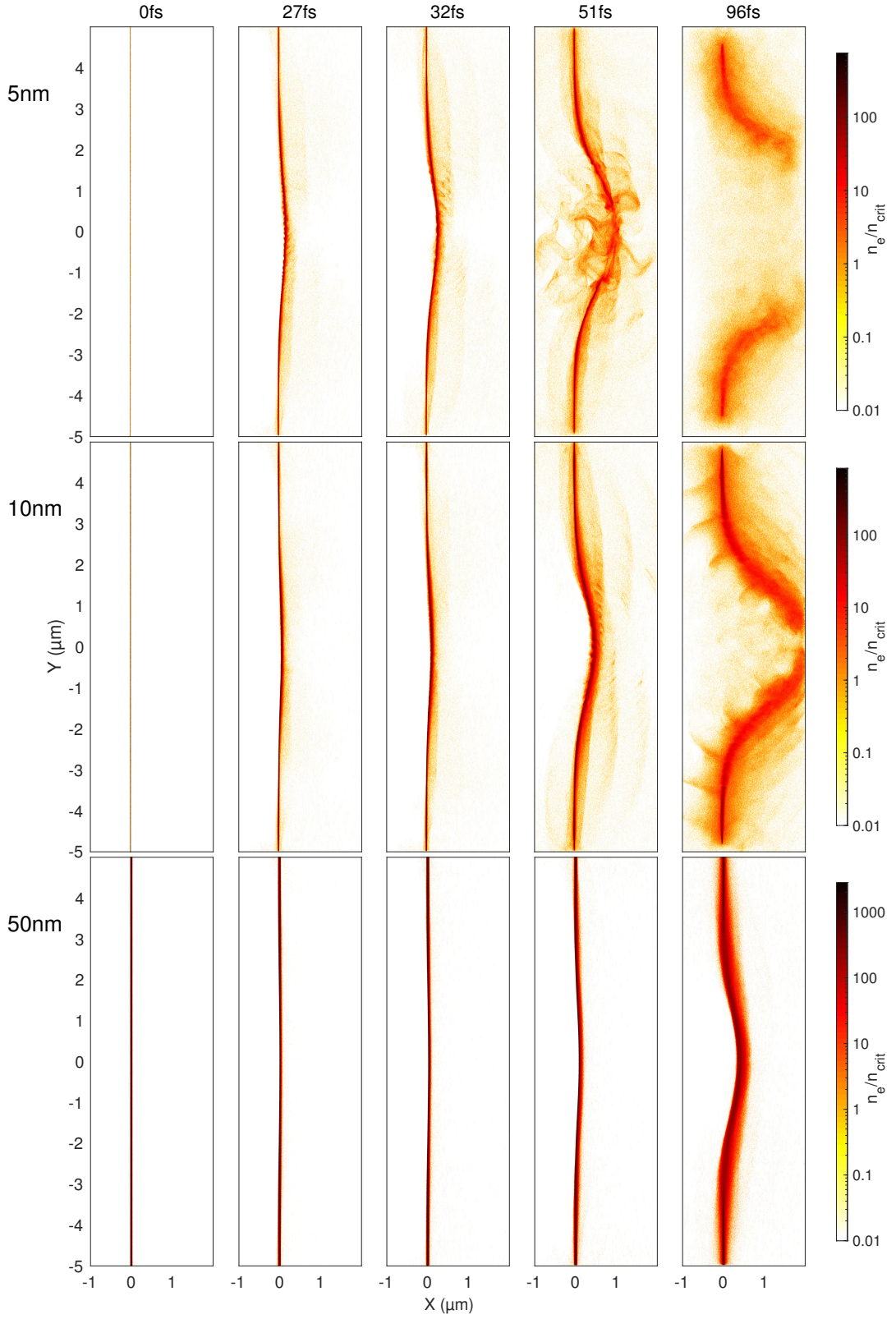


Figure 5.2: Snapshots of the electron density in the simulation box as a function of simulation time, for a 5, 10 and 50 nm target irradiated by a circularly polarised laser pulse.

the interaction. In comparison, for linear polarisation the transition to relativistic transparency occurred around 32 fs. As the laser pulse can penetrate the target, more substantial electron heating is finally seen, with electrons accelerated in the forward and backward direction. At the final timestep of 96 fs the centre of the target has blown out and left the simulation box.

For a 10 nm target irradiated by a circularly polarised laser pulse, the early timesteps in Figure 5.2 shows significantly less target heating than for linear polarisation, with only a slight target expansion on the rear surface. As the laser intensity increases, the target front surface slowly buckles due to the radiation pressure, however no electron bunches are accelerated. This is due to the suppression of the oscillating $J \times B$ acceleration mechanism for circular polarisation. Again, in comparison to linear polarisation, the density stands at $\sim 300\, n_{crit}$ and $\sim 200\, n_{crit}$ instead of $\sim 150\, n_{crit}$ and $\sim 70\, n_{crit}$ for the respective timesteps of 27 fs and 32 fs. Additionally, as the target remains normal to the incident radiation, vacuum and resonant heating do not occur. This leads to a lower thermal pressure of the plasma, which is therefore more buckled by the radiation pressure than for linear polarisation.

At 51 fs, the target shows some considerable buckling, as the critical surface has shifted $\sim$ 500 nm in the forward direction due to radiation pressure. With a target surface no longer normal to the incident radiation, it experiences stronger heating, as shown by the accelerated electron bunches in the forward direction. This also causes the target to expand. At the final timestep, the target front surface has been displaced by 1.5 µm and the electron density has dropped by an approximate factor of ten to $\sim 8\, n_{crit}$. While this value is above the relativistic critical density at this timestep (for $t = 96$ fs, $n_{crit}^{rel} = 1.7\, n_{crit}$) a clear hole in the centre of the target can be seen, indicating transmission of any remaining laser radiation. The late timestep also shows the development of transverse instabilities on the front surface that occur at intervals of approximately $\lambda_0 = 800$ nm. The late time target evolution differs strongly in comparison to linear polarisation as the target remains approximately intact, with a density of around $8\, n_{crit}$. Radiation is transmitted to the rear surface through a 500 nm hole in the target, as opposed to through a low density plasma as seen for linear polarisation.

For the 50 nm target a similar trend occurs. Very little plasma heating and expansion is seen

for the first few timesteps, despite the critical surface shifting by $\sim 50\,\text{nm}$ at 51 fs. In contrast to the 10 nm target, no electron bunches or plasma expansion are seen. Finally at 96 fs, the critical surface is seen to have shifted by $\sim 300\,\text{nm}$ in the forward direction. Very little target expansion is seen, in particular on the target front surface at $\mid y \mid \geq 1\,\mu\text{m}$ where the radiation pressure is highest. In comparison, for linear polarisation numerous electron bunches were accelerated off the rear surface and a more substantial density decrease was seen.

Thus, Figures 5.1 and 5.2 give a good overview of the interaction dynamics occurring for different thickness targets irradiated by a linear or circular polarised light. For each polarisation, the targets experience decreasing amounts of plasma expansion for increasing thickness with spatial instabilities developing in underdense plasma. Between polarisations, large differences in target heating are expected for the same target thickness, as linear polarisation causes significantly greater plasma expansion with more accelerated electron bunches. In comparison, for circular polarisation the interaction is primarily dominated by the radiation pressure of the laser pulse. This is shown by the displacement of the target's critical surface in the forward direction and reduced amount of electron heating and acceleration. The comparison therefore highlights the effect of the $J \times B$ heating mechanism which is a constant force for circular polarisation and an oscillating force of higher magnitude for linear polarisation. Finally, it also gives an indication of the effect of incidence angle on energy absorption as, for circular polarisation, electron bunches are only visible when the target and laser pulse are no longer normal.

In order to make a more quantitative comparison between target thicknesses and polarisations and to further understand the changes in target heating, the electron kinetic energy distribution function was plotted with respect to time in Figure 5.3. In the figures, time increases vertically down the y axis, and the electron energy is the forward and backward direction is plotted on the x axis. Electrons accelerated in the backward direction are shown to the left hand side of zero energy, those accelerated in the forward direction are shown to the right. The time evolution of the laser intensity is also given as a benchmark in units of $\gamma = \sqrt{1 + a_0^2}$.

Figure 5.3 compliments Figures 5.1 and 5.2 by quantitatively plotting the electron distribution

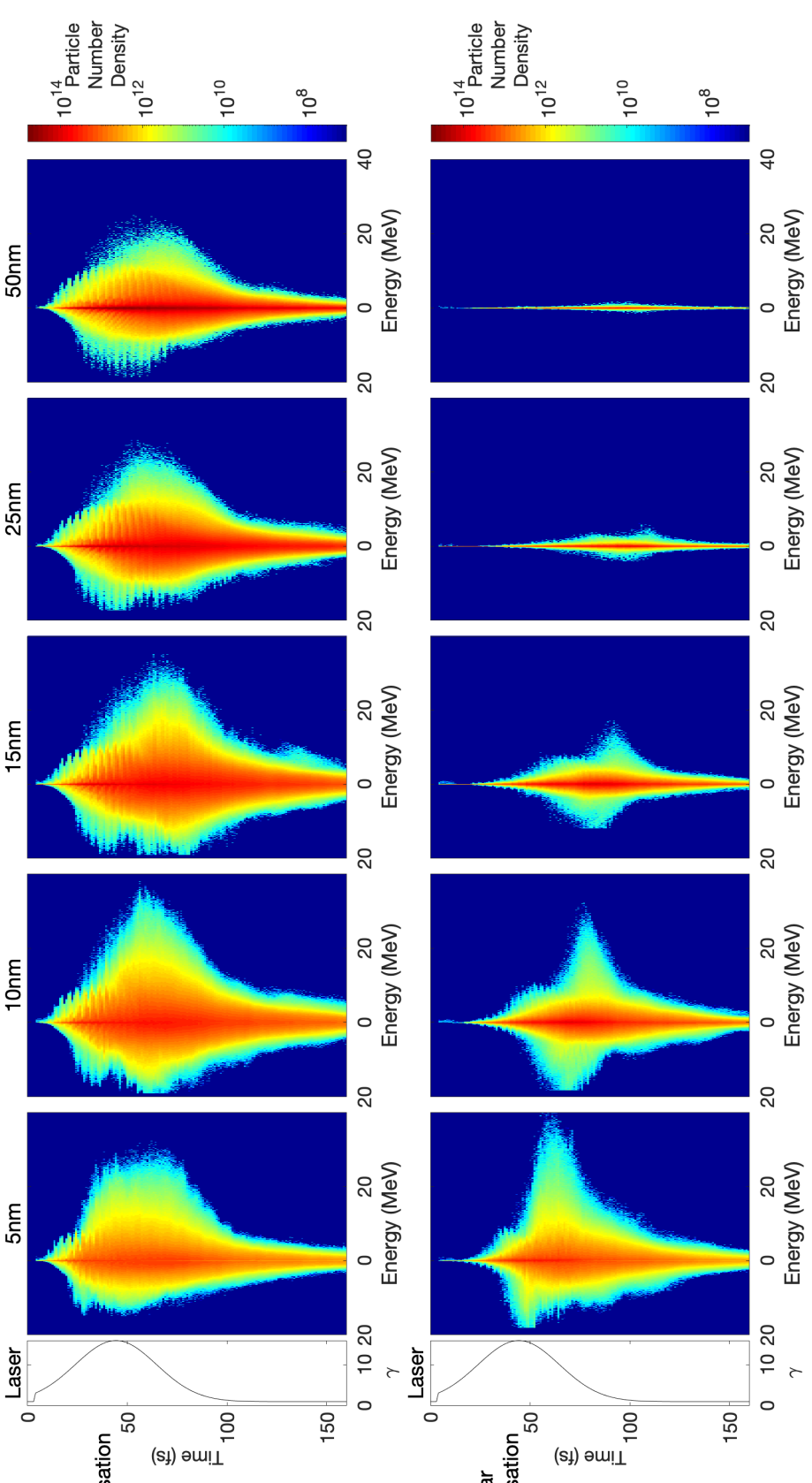


Figure 5.3: Electron energy distribution as a function of target thickness for targets irradiated by a linearly or circularly polarised laser pulse. Electrons accelerated in the backward direction are shown to the left hand side of zero energy, those accelerated in the forward direction are shown to the right.

function with time. Upon primary analysis, Figure 5.3 highlights the differences between polarisations, with linear polarisation experiencing a 75% variation in maximum electron energies over target thickness. In comparison, circular polarisation experiences a strong decrease in electron energies, with electrons from 50 nm targets reaching energies around 10% those of a 5 nm target. The differences between polarisations is less visible for thinner targets, as despite variations in the temporal evolution of the electron distribution, little difference in maximum electron energies are measured (maximum circular polarisation electron energy accounts for $\sim 75\%$ of that for linear polarisation). This is due to the target thickness being approximately the skin depth (5 nm), with the similarities between polarisations rapidly diverging as target thickness increases.

Additionally, Figure 5.3 gives information on the front and rear surface dynamics. For example, by examining the 5 nm target irradiated by a linearly polarised laser pulse, the electron distribution is shown to be initially cold. The electron energy distribution expands symmetrically as the laser's rising edge interacts with the target. However, as the laser intensity increases around 20 fs, the electron distribution function becomes asymmetric with a temporary, preferential acceleration in the backward direction. This originates from electrons accelerated off the target's front surface, creating a strong electrostatic sheath on the front surface. At 25 fs, the electrons accelerated in the forward direction see a strong increase in energy and particle number, while simultaneously the electrons accelerated in the backward direction see a drop in particle number and energy. For the remaining duration of the laser pulse, or until $t = 100$ fs, the energy distribution remains asymmetric. The electrons accelerated in the backward direction experience a quasi-linear decrease in energy and particle number with time as the plasma expands and cools, and the particles leave the simulation box. In comparison, the electrons accelerated in the forward direction experience an exponential decrease.

The trend of increasing electron energy in the backward direction followed by a sudden increase in the electron energies of the forward direction is mirrored in the 10 nm and 15 nm targets for both linear and circular polarisations. Particularly visible in circular polarisation due to the narrower electron energy spread, the effect of sudden increase in hot electron temperature is offset by approximately 20 fs for increasing target thickness. The effect is also offset between

polarisations, with circular polarisation experiencing the reversal of preferred electron acceleration direction up to 25 fs later than linear polarisation. A possible cause for the change in preferred electron acceleration direction could be due to the target transitioning from an overdense plasma, where electrons are accelerated by a sheath on the front surface, to a relativistically underdense plasma, where the electrons are accelerated by the laser field. The temporal delay between polarisations and target thicknesses is attributed to the differences in target heating and expansion, as seen in Figure 5.1 and Figure 5.2.

For the thicker targets of 25 nm and 50 nm, the electron energy distribution is more symmetric between the forward and backward accelerated electrons implying no transition in to transparency. For linear polarisation, the maximum electron energy obtained in the forward direction is around 75% of that for thinner targets. For circular polarisation, a factor of approximately 10 decrease in electron energies is measured between the thin and thicker targets.

The distribution of the electron energy gives an indication of the plasma dynamics on the front and rear surface, as well as providing a quantitative measure of the hot electron temperature and it's evolution in time. By assuming a two temperature distribution, hot and cold, of the electron population, the temperature evolution of the hot electrons was plotted in Figure 5.4.

Initially, before the arrival of the laser pulse, the target is solid and cold. The temperature evolution of the plasma is gaussian in shape and follows the ponderomotive potential, with an approximately linear increase in temperature for all target thicknesses and polarisations. Comparing the rate of target heating between polarisations shows that for linear polarisation and thinner targets of 2 and 5 nm, the rate of target heating is steep, corresponding to approximately 34 $\mathrm{keV\,fs^{-1}}$. As target thickness increases above 10 nm, the rate of heating decreases to 21 $\mathrm{keV\,fs^{-1}}$. Circular polarisation experiences a wider range of electron temperatures, as could be expected from the range of electron energies seen in Figure 5.3. For thinner targets, the heating matches the rate of heating of thicker targets irradiated by a linearly polarised laser pulse, notably 21 $\mathrm{keV\,fs^{-1}}$. For the thickest targets, the rate decreases to 1.5 $\mathrm{keV\,fs^{-1}}$, a factor of 14 lower than for linear polarisation. From Figure 5.1 and 5.3, linear polarisation is shown to heat more electrons and to higher temperatures than circular polarisation. Thus, the differ-

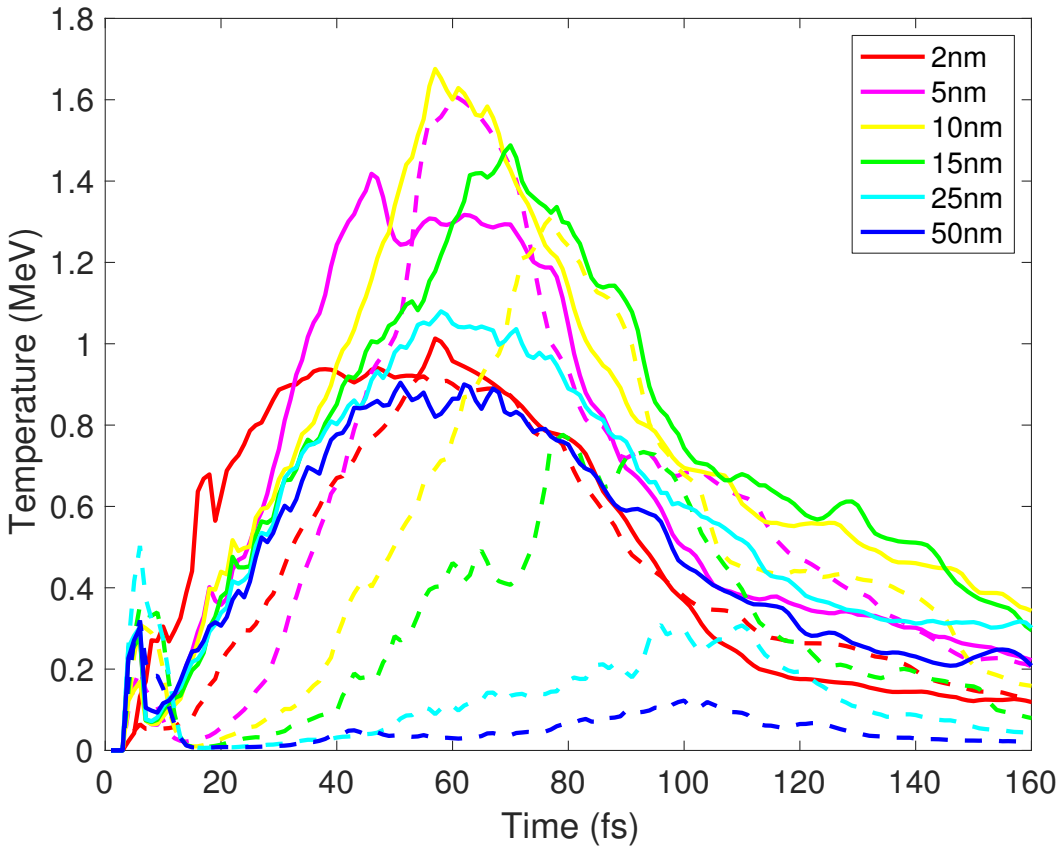


Figure 5.4: Temperature of the hot electron population with time for all targets and polarisations. Interactions occurring with a linearly polarised laser pulse are shown in a continuous line; those with a circularly polarised pulse with a dashed line. Note the peak of the laser pulse occurs at 44 fs.

ences in rate of heating can be attributed to the J × B heating mechanism that is suppressed for circular polarisation.

For linear polarisation and the targets in the range of $5 - 15$ nm, the maximum temperature is reached at 35 fs, with the subsequent peaks occurring ~ 10 fs later for increasing target thickness. However this trend is reversed when the target thickness reaches 25 nm and above, where the peak electron temperature is found at ~ 60 fs. Comparatively, for circular polarisation, the peak plasma temperature for a 5 nm target occurs at 54 fs, 10 fs after the peak of the laser pulse. The maximum of each subsequent target thickness occurs ~ 15 fs later than the previous.

For both polarisations therefore, the respective highest electron temperatures is seen at later times for increasing target thickness. This can be explained from the plasma dynamics seen in Figures 5.1 and 5.2. Concentrating on linear polarisation and the 5 nm target, as the electrons

are accelerated by the laser, they gain energy and increase the temperature of the plasma. The plasma therefore expands outwards and the density decreases. When the density drops below the relativistic critical density, the laser pulse is transmitted and the electron acceleration, or target heating, mechanism changes. The time when the target is shown to go relativistically transparent in Figure 5.1 corresponds closely to the time where the backward accelerated electrons experience a sudden increase in energy in Figure 5.3. It also corresponds to the time where the maximum plasma temperature is attained in Figure 5.4. This is true for all targets in the range $5 - 15\,\text{nm}$ irradiated by a linearly polarised laser pulse. Thus, this points to a strong correlation between plasma temperature and target heating time, where strong electron heating occurs while the target remains overdense. However, when the density drops below the relativistic critical density and the laser is able to transmit through the target, a peak in electron heating followed by decreasing electron energies is seen.

For circular polarisation, a similar behaviour is seen where the maximum electron temperature for each target thickness is offset temporally for increasing target thickness and for targets $\leq 15\,\text{nm}$. This may be due to the heatings dependence on target buckling, thus ensuring a non-normal angle of incidence that enables resonant vacuum heating to heat the target. Again, when the density drops below the relativistic critical density the laser is able to transmit, leading to a peak in electron energies followed by much lower rates of target heating [116].

While the peak plasma temperature shifts in time for increasing target thickness, the magnitude of the peak value varies for different polarisations and target thicknesses. For linear polarisation, the maximum plasma temperature is attained for a 10 nm target, whereas for a circularly polarised laser pulse the maximum plasma temperature is attained for a 5 nm target. The maximum values are 1.7 MeV and 1.5 MeV respectively. This shows that to maximise the plasma temperature, an optimum target thickness exists. For targets above the optimum thickness, the greater target mass means a larger number of electrons to heat and hence higher temperatures are not reached. Due to the higher rates of target heating for linear polarisation, a thicker target is needed to maximise the plasma temperature in comparison to circular polarisation.

For thicker targets ($\geq 25\,\mathrm{nm}$), those irradiated by a linearly polarised pulse experience similar rates of target heating as the thinner targets, and reach plasma temperatures of around 0.9 MeV. This value decreases by 10% as the target thickness doubles to 50 nm. For circular polarisation however, a strong decrease in plasma temperature can be seen, on par with the electron energies presented in Figure 5.3. The maximum temperatures achieved rapidly reach a fraction of that of thinner targets, dropping from 1.3 MeV for a 10 nm target to 0.1 MeV for a 50 nm target. This can be explained through the dependence on target buckling, as if the target remains normal to the incident radiation heating mechanisms such as vacuum heating (in an ideal case, such as those in a simulation) are unable to operate. Thus, until the radiation pressure of the laser is able to distort the front surface, the target experiences little heating. Thus, as target thickness increases, the mass needed to be displaced increases, causing both a temporal delay in heating and, due to the finite length of the laser pulse, a lower intensity interacting once buckled. Additionally, both polarisations see a small peak in electron temperature at early times. This may be due to a small population of hot electrons, created from a high contrast laser pulse hitting a steep density gradient. As the density gradient increases, the hot electron population merges with the heating bulk of the plasma.

Finally, as the 2 nm target lies under the plasma skin depth, similar interactions are expected for both linear and circular polarised light. Indeed, that is shown in Figure 5.3, where a maximum temperature of 0.9 MeV is seen for both polarisations, despite circular polarisation achieving those temperatures at a later time of 54 fs.

In order to quantify the change in plasma conditions, the variation of electron density in the focal spot region over time was plotted in Figure 5.5 for the range of experimental target thicknesses. The electron density was calculated by taking the averaged maximum electron density over the FWHM of the laser focal spot region and target thickness. The black dashed line represents the relativistic critical density, calculated by multiplying the critical density, n_{crit}, by the gamma factor, γ of the laser pulse at that time step, i.e. $n_{crit}^{rel} = \gamma n_{crit}$. A target is considered to have gone relativistically underdense when the corresponding curve has dropped below the black dashed line. Thus, the remaining intense part of the laser pulse is transmitted.

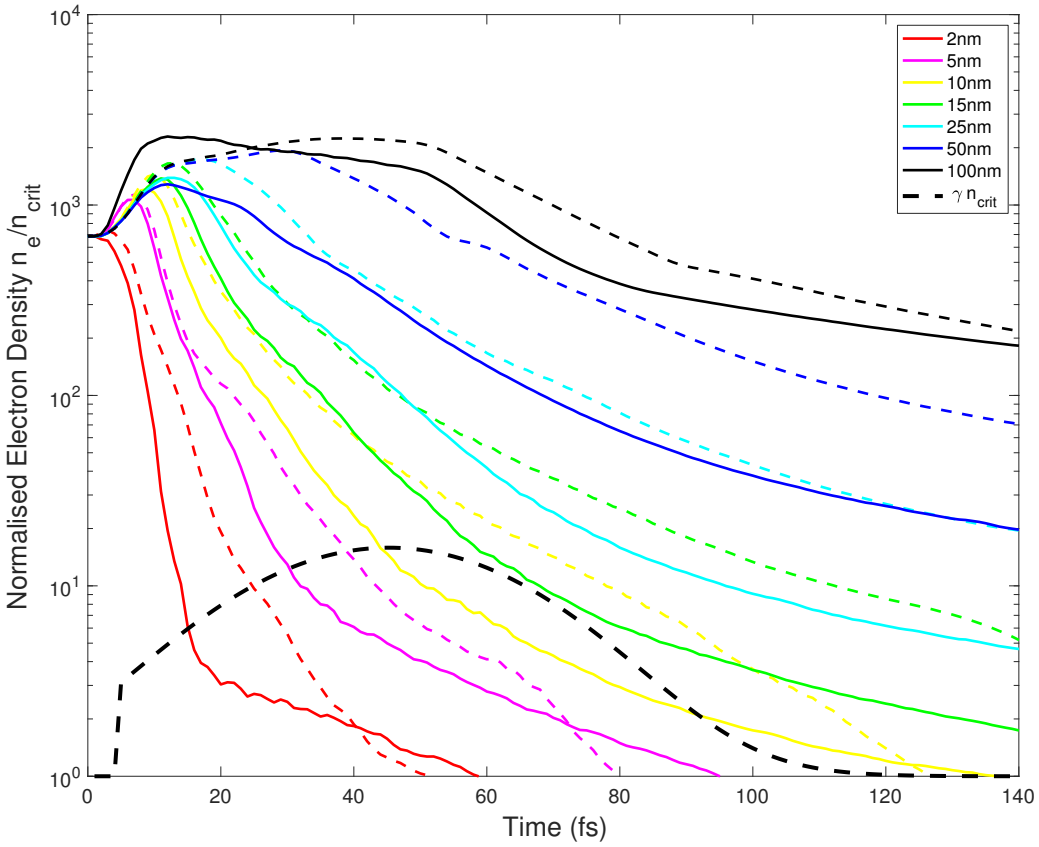


Figure 5.5: The electron density in the focal spot region as a function of simulation time for different target thicknesses. Interactions occurring with a linearly polarised pulse are shown in a continuous line; those occurring with a circularly polarised pulse are shown in a coloured dashed line.

As shown in Figure 5.5, there is a direct correlation between target thickness and the time taken for the electron density in the focal spot to drop below the relativistic critical density. For targets of 15 nm or above, the electron density is not measured to drop below the relativistic critical density. Differences between polarisations are clearly visible, with linear polarisation causing the electron density to drop more rapidly than circular polarisation. Initially, the targets experience a compression on the front surface, shown by an increase of electron density at early times. This occurs for all bar the 2 nm target due to it's thickness being less than the plasma skin depth ($l_s = 5\,\text{nm}$). The compression is caused by the radiation pressure of the laser exceeding the thermal pressure of the target. Linear and circular polarisation experience different amounts of target compression, with circular polarisation being compressed for a much longer period of time due to less target heating. After a couple of femtoseconds, the thermal

pressure of the plasma comes to dominate due to increasing electron temperature, as shown in Figure 5.4, and the target re-expands.

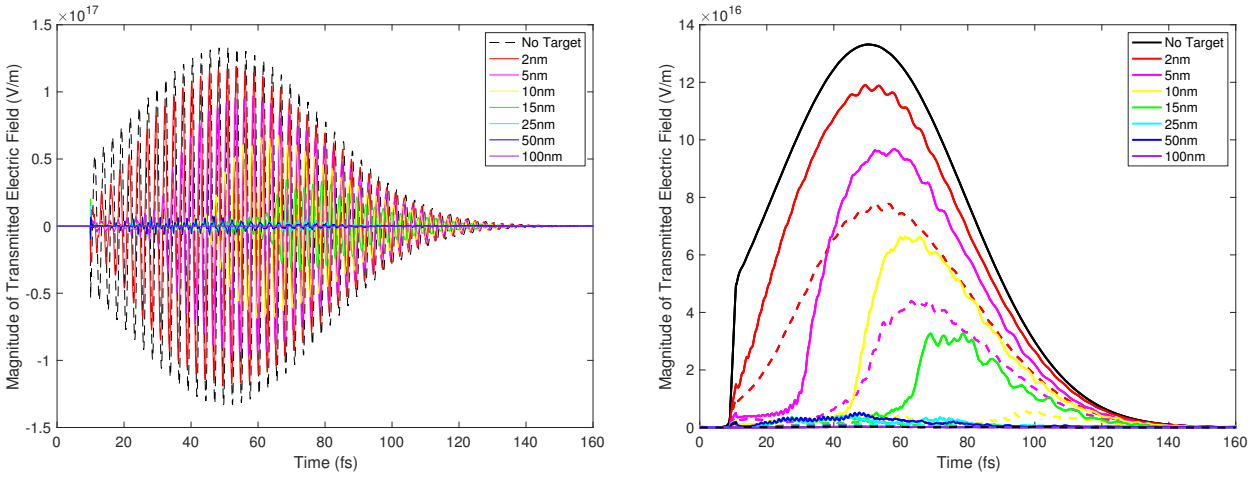
Again, a different trend is seen for thinner targets ($\leq$ 10 nm) compared to thicker ones ($\geq$ 15 nm), with thin targets experiencing a rapid exponential drop in electron density until the latter drops below the relativistic critical density. Then, targets irradiated by a linearly polarised laser pulse experience a significant change in the rate of density decrease, with the rate becoming much weaker. In comparison, targets irradiated by a circularly polarised laser pulse experience a more subtle change in expansion rate. For thicker targets, after initial compression due to radiation pressure, the rate of decay is exponential with a weak gradient that remains approximately constant for the duration of the laser-plasma interaction.

For targets that drop below the relativistic critical density limit, the transition happens $\sim$10 fs earlier when irradiated by a linearly polarised pulse than circularly polarised pulse. This is in agreement with the results from Figure 5.3 and is due to the different heating mechanisms applicable in each case. Additionally, note that for the case of the 10 nm target irradiated by a circularly polarised laser pulse, discrepancies between the results portrayed in Figure 5.2 and 5.5 are seen. Figure 5.5 measures the target as remaining overdense for the duration of the laser pulse, whereas in Figure 5.2 a clear hole in the target is seen. This is due to the averaging of the electron density over the focal spot region that does not take into account small spatial variations in electron density.

5.2 Transmitted Electric Field

The quantity of transmitted light for varying target thickness was measured and is plotted in Figure 5.6a, as was measured experimentally in Section 4.4.

Figure 5.6a shows the transmitted electric field against time for varying target thickness and laser polarisations. The electric field is sampled at the rear of the simulation box, far from the laser-plasma interaction, and the electric field of a simulation performed with no target is also plotted for comparison (i.e 100% transmission). Figure 5.6a shows the oscillating transmitted



(a) Transmitted Electric Field (b) Transmitted Electric Field Envelope

Figure 5.6: Plots showing the transmitted electric field as a function of simulation time for different target thickness's. The transmitted electric field of a linearly polarised laser pulse is shown in (a). In (b), the envelope of the transmitted pulse is plotted for both linearly (continuous lines) and circular (dashed lines) polarised pulses.

electric field for various target thicknesses irradiated by a linearly polarised laser pulse. As the target thickness increases the quantity of transmitted light decreases, and the onset of transparency shifts later in time. The rising edge of the transmitted pulse becomes steeper, until it becomes almost step like for 15 nm. Beyond this thickness, radiation of much lower magnitude is still seen, with a periodically oscillating electric field occurring at early times around 40 fs for the 50 nm target irradiated by a linearly polarised pulse.

Figure 5.6b shows the pulse envelope for both circular and linear polarisation, allowing for a comparison to be done. For all cases, targets irradiated by a linearly polarised laser pulse transmit a larger quantity of incident radiation, shown by a higher peak transmission, and at earlier times than for circular polarisations. This confirms a large difference in plasma conditions between the two polarisations, mirroring the results seen experimentally and the trend in electron energies seen in Figure 5.3.

Thus, Figure 5.6 confirms the theory of optical shuttering presented in Section 4.4, where the plasma acts as a shutter, becoming relativistically underdense at a time proportional to its thickness [117]. The rising edge of the laser pulse is reflected or absorbed until the plasma becomes transparent, when the remainder of the truncated laser pulse is transmitted. Exper-

imentally, this coincides with a change of spatial profile of the transmitted light and a change in trend of the transmitted energy. Therefore it can be concluded that these results indicate a change in plasma conditions between 15 and 25 nm targets, with the latter remaining overdense.

Both Figure 5.5 and 5.6 show the target transitioning from an overdense to underdense medium. In order to check the validity of the conclusions drawn above, and to further understand the limitations of the simulations, the time taken for the target to reach transparency was plotted in Figure 5.7. This was calculated by measuring the time between the laser being incident on the target and the density dropping below the critical density. These values where sampled from two different sources: firstly from Figure 5.5, where the time for the electron density in the focal spot to drop below the relativistic critical density was sampled from the plotted data. This was calculated for both polarisations and all target thickness. Then using the data in Figure 5.6b, the time for the transmitted electric field to rise to 10% of the input electric field was calculated. This value was taken arbitrarily, but proved a good benchmark when visually comparing to Figure 5.6b.

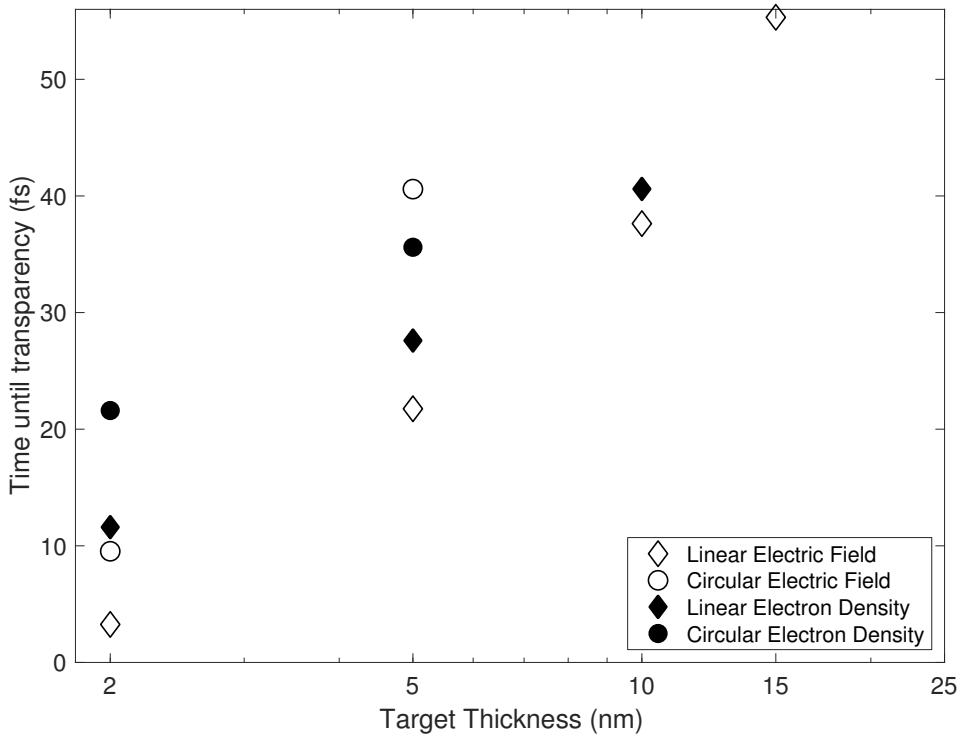


Figure 5.7: Time taken for targets to become transparent as measured from the electron density results (filled markers) and the transmitted electric field results (empty markers).

Figure 5.7 plots the time that targets remain overdense for against increasing target thickness as calculated through the two different methods. As expected, targets irradiated by a linearly polarised pulse reach transparency faster than those with circular polarisation for both measurement methods. For 2 nm, the target is thinner than the skin depth, and hence according to the transmitted electric field radiation is transmitted almost instantaneously. According to the electron density however, it takes around 12 fs for the target to drop below the relativistic critical density. The electron density shown in Figure 5.5 was calculated by taking the maximum density in the focal spot region. While this may be a good approximation for the general evolution of the density in the focal spot region as a whole, it does not account for spatial variations therein. Thus, it is possible that parts of the focal spot region go underdense earlier on in the simulation, transmitting the radiation seen in Figure 5.6b. For the remaining target thicknesses the results converge, with a close agreement for the 10 nm target. Figure 5.7 shows a linear increase in temporal delay in transparency with target thickness. This is in agreement with the linear decrease in transmitted energy shown for experimental results in Figure 4.6 for targets in the range of $2 - 15$ nm.

Finally, in order to quantitatively compare the simulations to the experimental results shown in the previous chapter in Figure 4.6, the relative magnitude of transmitted energy in the simulations is plotted in Figure 5.8. The results are normalised to the transmission of a null shot (no target).

Figure 5.8 shows multiple 10's of percent transmission for the thinner targets, which rapidly drops to a few percent for thicker targets. Interactions occurring with linearly polarised pulses show an almost factor of 2 higher transmission than for circularly polarised pulses, with the difference particularly obvious for thinner targets. A direct correlation between electron density, shown in Figure 5.1 and transmitted energy is seen, with targets going relativistically underdense transmitting large amounts of energy, whereas as much as $\sim 5\%$ radiation is measured beyond those remaining overdense. This result is important as it confirms a significant amount of radiation is measured beyond the critical surface, with a magnitude that is approximately constant over the overdense target thickness range.

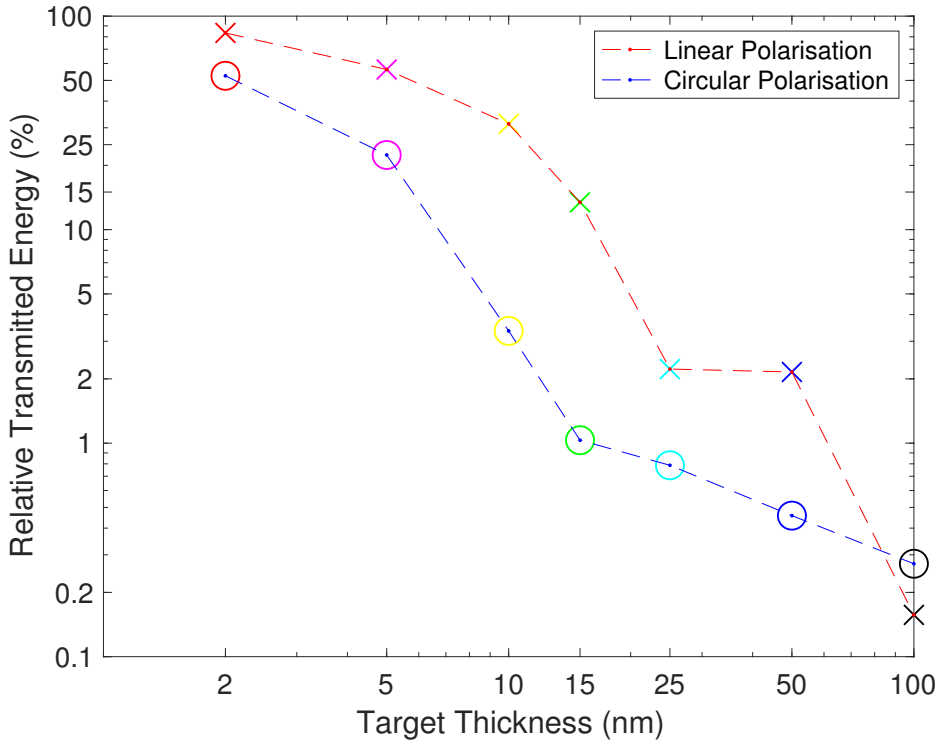


Figure 5.8: Transmitted energy with target thickness as sampled at the rear of the simulation box and normalised to the energy of the incident laser pulse

Comparing these results to those found experimentally in Figure 4.6, similar, albeit slightly smoother, trends are seen. Both results from the simulation and the experiment are plotted in Figure 5.9 to aid comparison. As a general overview, both experimental and simulation results show a similar trend with variations in qualitative results. For linear polarisation, a large quantitative difference is seen for thinner targets, with simulations predicting a transmission of around 90% compared to 55% for the experimental results. The qualitative differences reduce rapidly as the target thickness increases, and both experimental and simulation results show a steep decrease in transmission around 25 nm. This is in agreement with the experimental results, presented in Chapter 4, where it was concluded that targets below 25 nm go relativistically transparent in the duration of the laser pulse. For circular polarisation, a better quantitative agreement is found for the 2 nm target, however while both curves follow a similar trend, the quantitative results diverge for increasing target thickness.

The two main sources of error between the experimental and simulation results are the idealised conditions occurring in simulations, with the laser pulse being a perfect gaussian, and

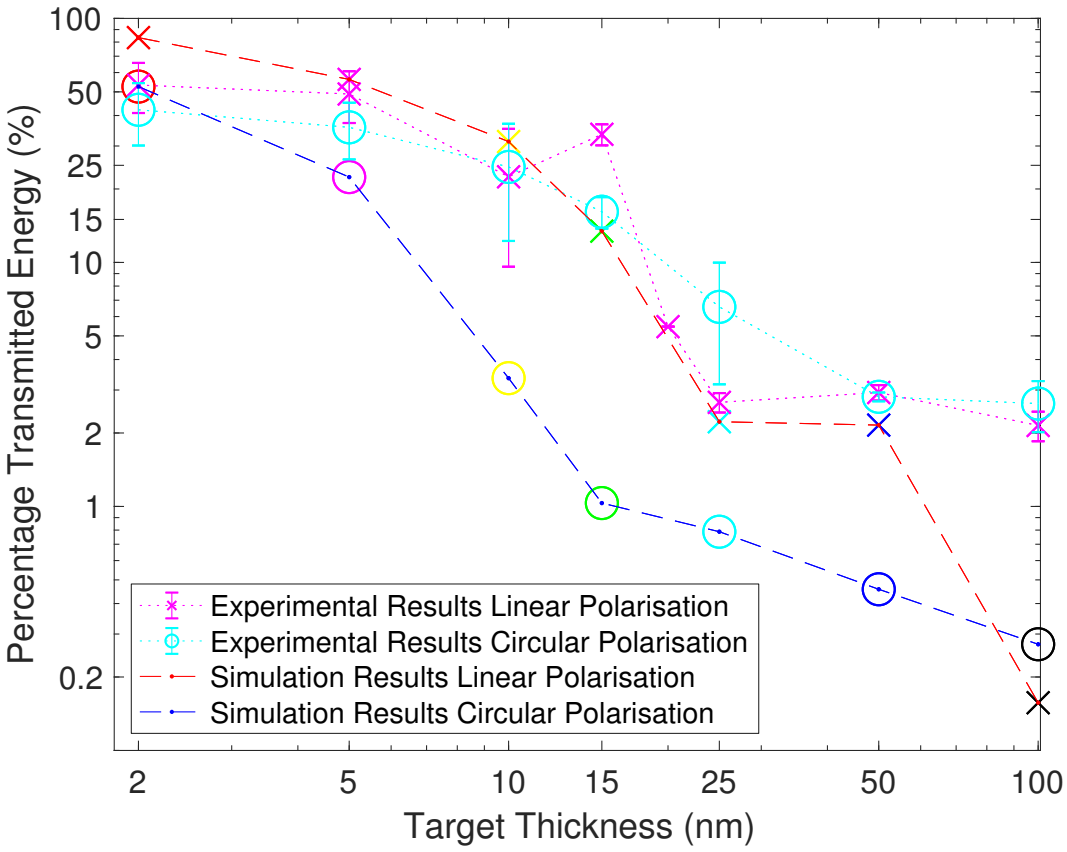


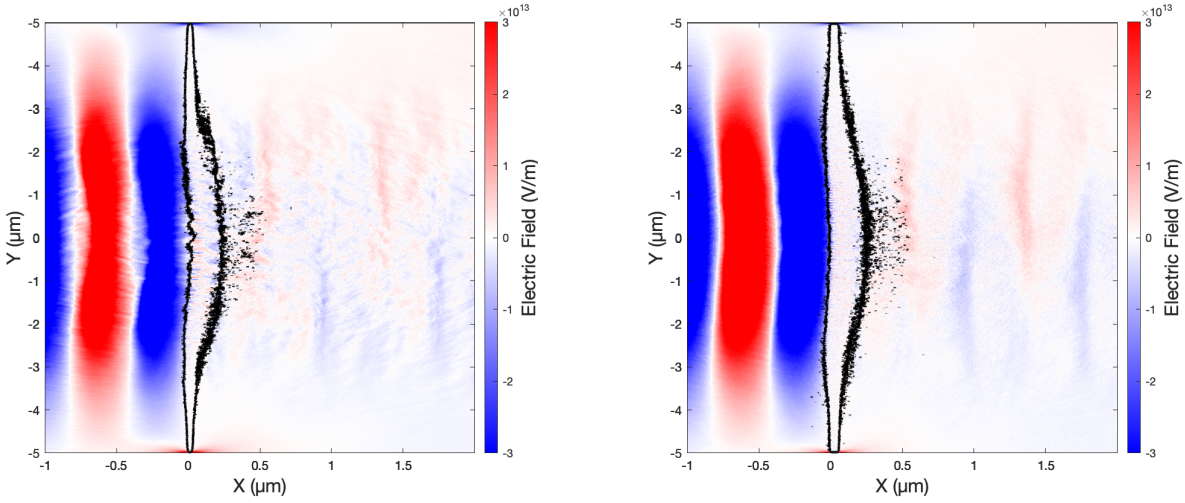
Figure 5.9: The quantity of transmitted 1ω light in both the simulations and the experiment.

the spatial distribution of energy in the focus spot during the experiment. As described in section 4.2.1, only 24.5% of the energy was located inside of the full-width-half-maximum. If the focal spot is not perfect, the quantity of laser light in the focal spot, and hence maximum intensity achieved, may be affected. Thus, the intensity used in the simulations was adjusted to accurately represent these experimental conditions. A secondary source of error may be the presence of contaminants on the targets front and rear surface. These contaminants are collected from the general environment and may arise from handling or vacuum chamber sources. Hydrocarbon contamination was accounted for in the simulations by including hydrogen into the bulk of the target, to the concentration measured experimentally before insertion into the vacuum chamber. In the simulations, the electric field was sampled around 2 µm from the target rear surface. Hence all forward scattered light was also sampled. While the amount of scattered light for laser-plasma interactions involving a thin target and intensities above $10^{18}\,\mathrm{W\,cm^{-2}}$ has been shown to be below 1% [96], this will nevertheless contribute to the small differences be-

tween the final results. To conclude, while the limitations of the simulations are visible in the quantitative analysis, they accurately reflect the trends in the interaction dynamics of interest.

5.3 Transition Radiation

An unexpected outcome of the experiment was the measurement of coherent light beyond the rear surface of an overdense target. Thus, simulations were used to further understand the origins of this radiation and confirm it's origin. Figure 5.10 show the electric field in the simulation box overlayed with the electron density for timestep $t = 45\,\text{fs}$ and two target thicknesses. The oscillating electric field is represented in red and blue, with the contour of the relativistic critical electron density shown in black.



(a) 25 nm target (b) 50 nm target

Figure 5.10: The transverse $\hat{y}$ electric field in the simulation box overlapped with the contour of relativistic electron critical density for a 25 nm target (a) and a 50 nm target (b) at timestep 45 fs and a linearly polarised laser pulse

In Figure 5.10, both targets remain opaque to the laser, as seen by the uninterrupted contour lines, with radiation seen beyond the target's rear surface. This radiation is more pronounced for the case of the 50 nm target and is located in the focal spot region ($y = \pm 3\,\mu\text{m}$) of the simulation box. For both targets, it is seen to have a periodic structure with linear polarisation in the vertically direction. This is consistent with the radial polarisation property of transition

radiation that is dependent on observation angle, as described in Section 2.5.3. Thus, the coherence and the spatial distribution of the radiation is in strong agreement with the electric field expected from transition radiation.

Transition radiation occurs due to fast electrons escaping the target's rear surface and causing the dipoles in the formation zone to oscillate. Thus, by observing the longitudinal momentum of electrons with respect to their $\hat{x}$ or longitudinal position in the simulation box, a confirmation of the bunched acceleration can be obtained.

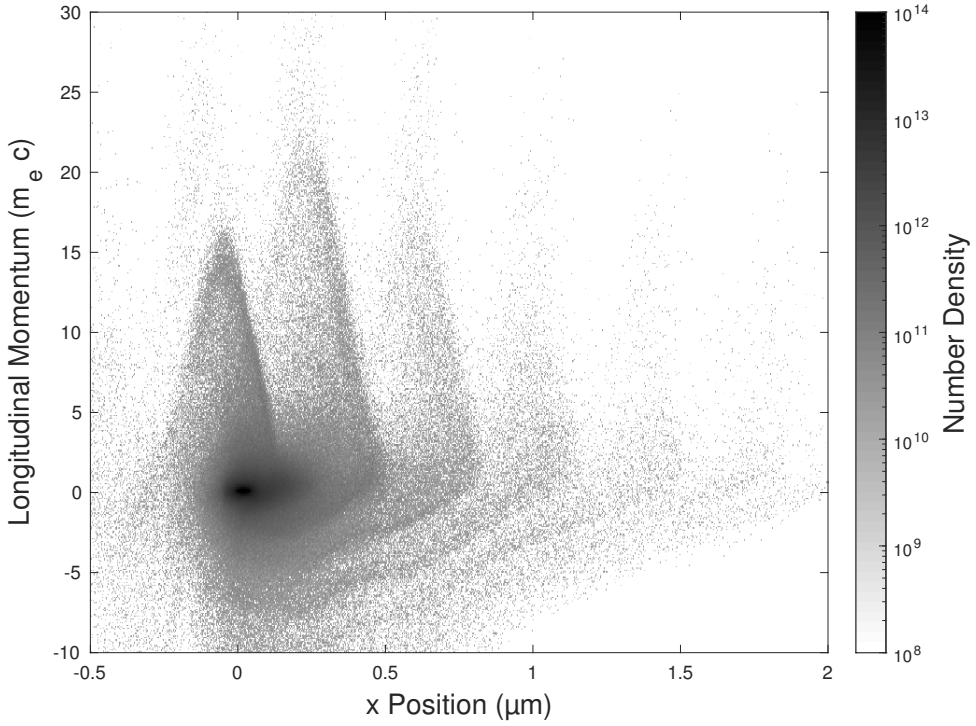


Figure 5.11: Electron longitudinal momentum against position in $\hat{x}$ for a 25 nm target irradiated by a linearly polarised laser pulse at timestep of 57 fs.

Figure 5.11 shows electrons accelerating in bunches in the forward direction, with peaks separated by 400 nm corresponding to an acceleration frequency of twice the laser frequency. While this figure could be further improved by increasing the number of particles in the simulation box, and thus giving more precise information on the energy spread of the electrons, it confirms that the electrons are accelerated in bunches to the rear surface with little straggling. This indicates that a strong coherent signal could be produced at multiples of the laser frequency, which in turn could be detected by a FROG. Therefore, all experimental and simulation evidence

strongly supports the identification of the radiation as coherent transition radiation.

5.4 FROG traces from Simulations

As FROG traces are notoriously difficult to collect, a sanity check was done by comparing the Wigner transforms (see Section 3.2.4) of the FROG traces found experimentally with those obtained through simulations. This is shown in Figure 5.12, where the experimentally retrieved Wigner transforms are presented above their simulation counterpart. Included above is the Wigner transforms of the input laser pulse. Here the temporal axis is in the $\hat{x}$ direction and the spectral axis in the $\hat{y}$ direction.

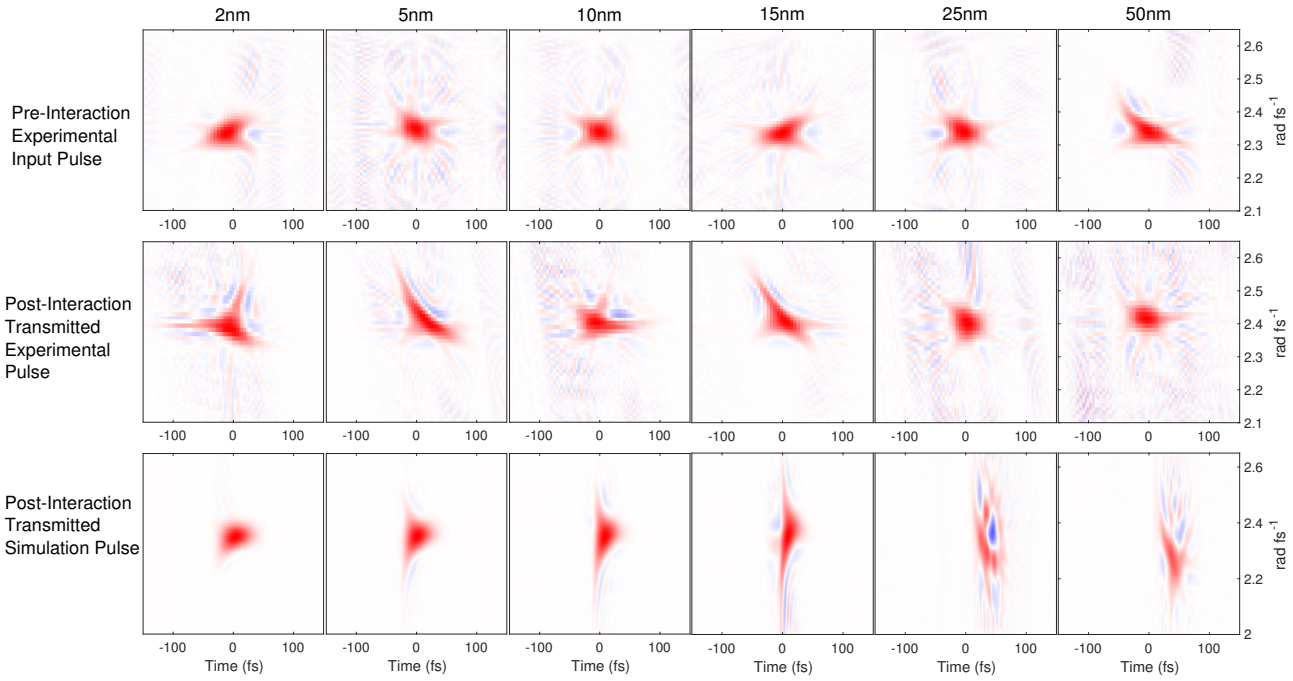


Figure 5.12: Comparing the Wigner transforms from experimental and simulation transmitted light. All laser pulses are linearly polarised except the 2 nm case which is circularly polarised.

Wigner transforms allow for the temporal and spectral properties of a pulse to be expressed in one image, thus facilitating the comparisons. Figure 5.12 shows a big difference between simulation and experimentally retrieved pulses. The experimental pulses have a smaller bandwidth and a variable amount of linear or higher order chirp, whereas the simulation results show a

large bandwidth and very little to no chirp. While the two sets of traces have differences, the causes of which will be discussed shortly, they do present similar trends.

The experimental results, discussed in detail in Section 4.6, showed decreasing pulse length for increasing target thickness, and a significant amount of chirp for targets less than 25 nm. In Figure 5.12 and looking at the experimental traces, these results are represented by a decrease in temporal width of the pulse for increasing target thickness. Note the 2 nm trace is slightly shorter than the successive ones due to it being from a circularly polarised laser pulse. The level of chirp is represented by the angle of the Wigner trace, where a variation in chirp is represented by the change in angle. The increased bandwidth shown in Figure 4.10b can be seen in the high intensity tails of the Wigner transforms, and are particularly noticeable in the 5 nm target. The Wigner transform allows for the spectral shifts to be located in time, with a clear blue shift at early times before a red shift at later times. A clear change in trend is seen when moving to targets of thickness 25 nm and above, as the experimental trace loses its chirp and becomes more circular with higher order elements.

For thinner targets, the simulation results show a very round Wigner transform, with a large increase in bandwidth at early times. A decrease in temporal duration of the transmitted pulse is seen with increasing target thickness, as well as a large increase of early-time spectral bandwidth. The early time spectral bandwidth increases with target thickness, implying a steep rising edge to the transmitted pulse. For the 15 nm target, a very large bandwidth at early times is seen implying an almost step-like shape of the transmitted field. This is seen in Figure 5.6a and further confirmed when looking at the fall in electron density plotted in Figure 5.5. Again, a change in trend is seen for targets of 25 nm and beyond, as the Wigner transforms become more circular with more prominent higher order terms. This is in direct agreement with the experimental Wigners seen above.

Overall, the simulation Wigner transforms show a larger than expected bandwidth, as calculated by the time-bandwidth product [118]. This could be partially due to the lack of flexibility in the EPOCH PIC code, as to initialise a laser pulse only the pulse duration and central wavelength can be specified. A ramp-up time allows some control of the temporal profile however no

external control of the spectral bandwidth is possible. Measuring the bandwidth of a null shot in the simulation gave a FWHM value of $\sim 60\,\text{nm}$. In comparison, measuring the spectral bandwidth of the laser pulse used experimentally (as measured in the experimental front end), a value of $\sim 24\,\text{nm}$ was obtained. The larger than expected bandwidth in simulations does not prevent the pulse from experiencing chirp, however it may obscure the chirp from being visible in the Wigner transforms.

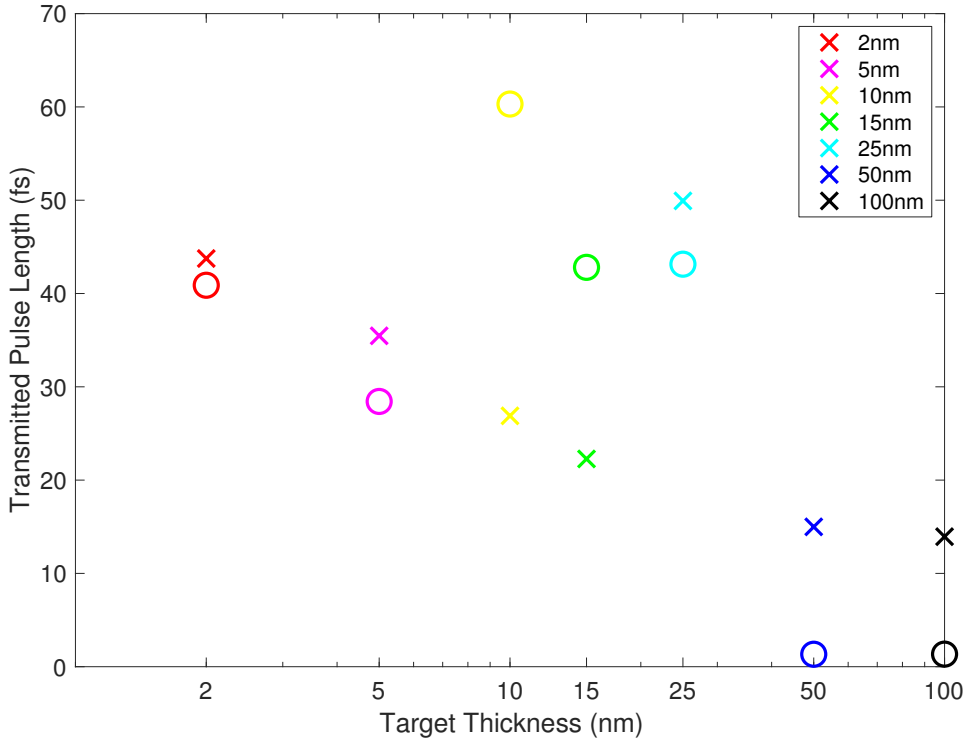


Figure 5.13: The FWHM pulse length of the transmitted intensity envelope as seen in simulations. Linearly polarised pulses are shown using crosses; circularly polarised pulses are shown using circles.

Finally, in order to compare the simulation results with the experimental ones, the temporal FWHM pulse length was plotted against target thickness in Figure 5.13. The overall trend of decreasing pulse length with increasing target thickness is in agreement with previous measurements. However erroneous results were measured for targets in the 10 - 25 nm region. This is due to significant structure in the transmitted electric field such that a numerical calculation does not accurately reflect the occurring physics. It is also important to note that the emitted radiation must be coherent to produce a FROG trace. Looking closely at Figure 5.6a, radiation for the 50 nm target can be initially seen to be coherent, or at least oscillating in a periodic

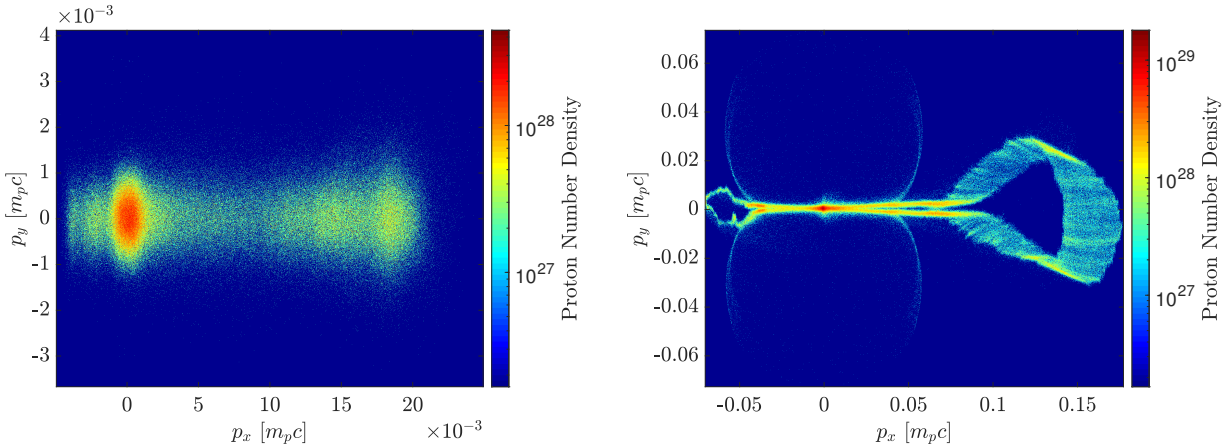
fashion. This periodicity soon diffuses leaving a pedestal of high intensity but incoherent light. Thus, the FWHM pulse length shown in Figure 5.13 is not an accurate representation of the same physical phenomena shown in Figure 4.11 for targets between 10 - 25 nm, as it includes a contribution from the high intensity incoherent radiation too.

5.5 Particle Diagnostic

As stated previously in Chapter 4, the primary aim of the experimental campaign was to explore ion acceleration from targets in the range of $2 - 100\,\text{nm}$ using a $\sim 5\,\text{J}$, 48 fs high contrast laser pulse. In these conditions two acceleration mechanisms occur: radiation pressure acceleration and relativistic transparency. From Chapter 4, strongly varying plasma conditions were seen over the target thickness scan, where targets $\leq 15\,\text{nm}$ were inferred to have gone relativistically transparent. From this, one can conclude that relativistic transparency acceleration occurred during the laser pulse. However, the dominant ion acceleration mechanism for each target thickness is unknown. As all acceleration regimes produce different ion spectra and occur under different plasma conditions, by looking at the evolution of particles in the simulation box, further information on the plasma dynamics can be inferred.

The ion phase space plots the longitudinal momentum against the transverse momentum for all particles in the simulation box at a given timestep. As ions are heavier than electrons, their motion is less affected by small spatial variations and more representative of the general plasma trends.

Figure 5.14a represents the proton phase space at $t = 12\,\text{fs}$, where the majority of the target is stationary, shown through a high particle density at $p_x \approx p_y \approx 0$. A much lower density quasi monoenergetic feature is shown in the positive p_x direction, around $p_x = 18 \times 10^{-3}\, m_p c$. This indicates the acceleration of a slab of material in the forward direction with a limited range of momentum in the y direction, corresponding to ion energies of around 0.8 MeV. Ions accelerated in the forward direction with no transverse acceleration originate from the centre of the focal spot due to the lack of transverse fields seen through symmetry. While the mo-



(a) Timestep: 12 fs

(b) Timestep: 44 fs

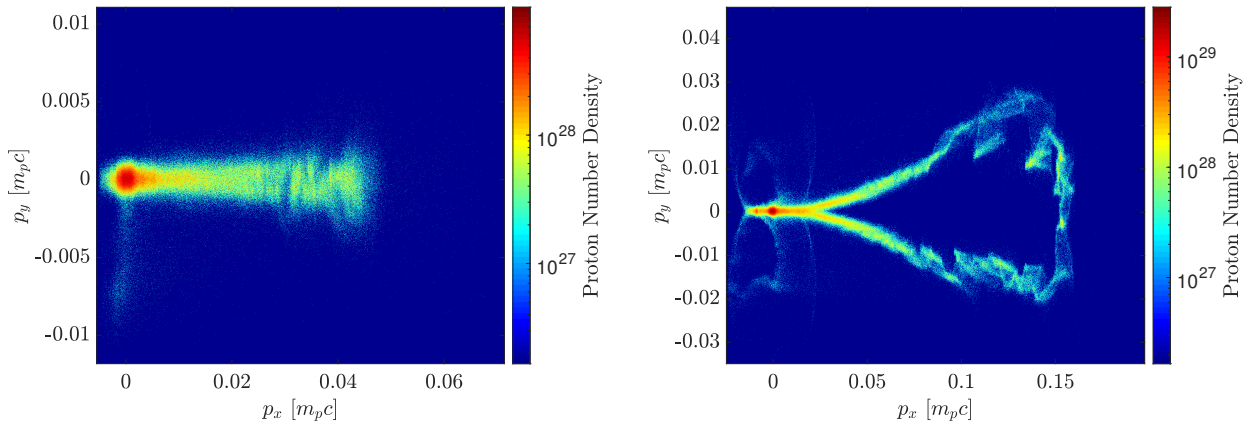
Figure 5.14: Proton momentum phase space at two different timesteps for a 5 nm target irradiated by a linearly polarised laser pulse.

noenergetic feature points towards radiation pressure acceleration occurring at the early stages of the interaction, a range of lower energy ions are seen accelerated along the laser axis. As efficient radiation pressure depends on the accelerated plasma slab to remain cold and hence overdense for the duration of the laser pulse, the ion energy spread implies gradual heating of the accelerated target slab causing it's eventual disintegration through transparency at later times. This suggests strong target heating at early times, as seen in Figure 5.4.

At the peak of the laser pulse (44 fs), the target has evolved to form a ring-like structure at higher energies, connected to the cold bulk of the target by two parallel streams of lower energy particles, shown in Figure 5.14b. A similar behaviour is mirrored in the backward direction but at lower energies, showing the backward accelerated ions interacting in the laser field. The streams of low energy particles have a narrow energy spread, and have transverse velocities of around 20% of their longitudinal values. This indicates that these ions have been accelerated by a similar field, and have substantially increased their transverse momentum compared to the $t = 12$ fs timestep. At values of $p_x > 85 \times 10^{-3} m_p c$, a ring like feature in the forward direction is seen, showing particles experiencing significant transverse acceleration, with values up to 25% of the longitudinal momentum. A low particle density is seen on the laser axis of $p_y = 0$, both from the bulk of the target up until higher values of p_x. Thus, few particles are being accelerated along the laser axis, implying a decreasing density in the areas of highest intensity and the end of the radiation pressure phase of acceleration.

Figure 5.14b points strongly to the target having transitioned to below the relativistic critical density. The low energy particles are deduced to have originated from the outskirts of the focal spot, as the transverse accelerating gradients are strongly proportional to the particles displacement from the regions of highest intensity. For the higher energy particles, initially accelerated as a slab of material in Figure 5.14a, the strong increase in transverse acceleration indicates the presence of strong transverse fields. This would occur if the laser transmits through the target and pushes the electrons out due to the ponderomotive force. Finally, the non-zero values of transverse momentum occurring for particles of all energies indicates a decreasing density along the laser axis, further supporting the hypothesis.

Thus, for the 5 nm target irradiated by a linearly polarised laser pulse, radiation pressure acceleration occurs at early times until significant target heating causes the accelerated slab to become transparent. The high energy particles then gain significant transverse momentum but no further longitudinal momentum, forming a ring like structure that diagnoses the targets transition into transparency. This also indicates the end of the rapid heating phase, as the ions leave the laser axis and hence no longer directly feel the fields of the laser pulse. Thus, similar conclusions to those taken from optical diagnostics can be drawn from the proton phase space. A similar figure is reproduced for a 5 nm target irradiated by a circularly polarised laser pulse, shown below in Figure 5.15.



(a) Timestep: 25 fs (b) Timestep: 44 fs

Figure 5.15: Proton momentum phase space at various timesteps for a 5 nm target irradiated by a circularly polarised laser pulse.

From Figure 5.2, the 5 nm target is shown to be significantly affected by the radiation pressure of the laser, with strong target buckling in the focal spot. At earlier timesteps, the proton momentum phase space of a 5 nm target irradiated by a circularly polarised laser pulse resembles that of linear polarisation, with a monoenergetic feature of almost identical energy in the forward direction. At $t = 25$ fs, the momentum phase space is shown by Figure 5.15a. Almost no backward acceleration of ions is seen, with a high density of low energy ions propagating forward at half the energy of their linear counterparts. The low energy, forward moving particles are shown to have little transverse momentum, whereas the particles with higher values of p_x show higher p_y values and longitudinal modulations. The high energy ions are those found at the highest accelerating gradients, which for radiation pressure and relativistic transparency can be found at the highest value of a_0 at the centre of the focal spot. Thus, high energy ions demonstrating a large amount of transverse momentum could indicate a transverse migration of the centre of the focal spot and be an indication of the target transitioning into transparency. Indeed, when observing the subsequent timesteps, the ring like structure is slowly seen to emerge over a timescale of $\sim$18 fs.

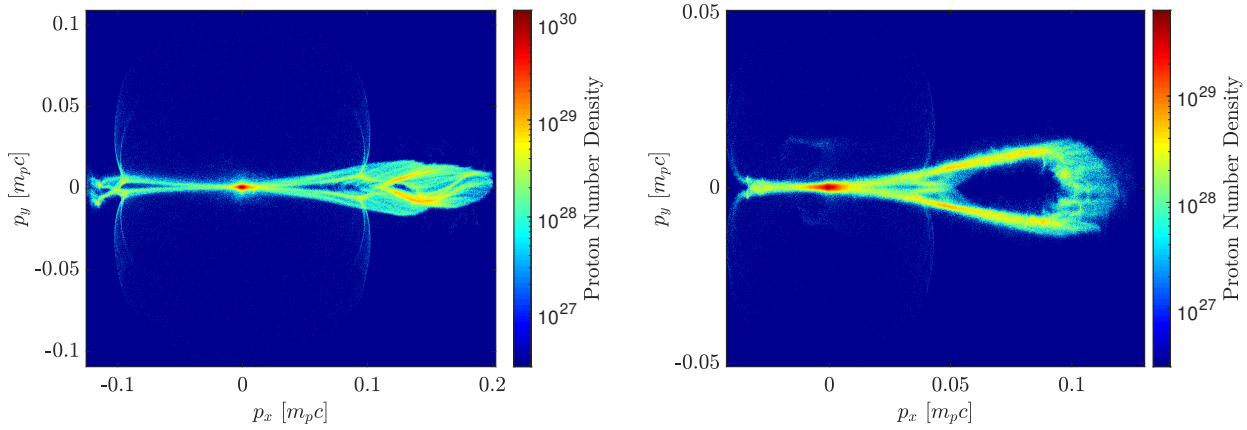
At the peak of the laser pulse, the ring like structure is seen as shown in Figure 5.15b. More triangular in shape, all particles that have experienced some heating have gained transverse momentum, with the quantity having an almost linear relationship to the magnitude of forward momentum. This indicates a stable target with heating proportional to the particle's position in the focal spot. For high values of p_x, small groups of particles with various amounts of transverse energies are seen, surrounded by a low particle density on axis. This all points towards a significant variation in conditions in the centre of the focal spot, which would amount to spatial modulations. Similar values of p_x and p_y are achieved at the peak of the laser pulse compared to linear polarisation, indicating similar maximum ion energies. Additionally, a small monoenergetic ion bunch is shown to have been accelerated backwards along the laser axis, indicating a potential sheath field on the target's front surface.

Thus, for the 5 nm target irradiated by a circularly polarised laser pulse, radiation pressure acceleration occurs at early times producing ions of energy a factor of two lower than for linear polarisation. Strong transverse acceleration of the high p_x momentum particles occurs at

later times for circular polarisation compared to linear polarisation, however both polarisations achieve similar ion energies at the peak of the laser pulse (by 44 fs). This indicates that circular polarisation experiences a delayed but faster rate of target heating compared to linear polarisation. This is in agreement with the rate of electron heating shown in Figure 5.4, where circular polarisation heats electrons to a higher temperature than for linear polarisation for a 5 nm target. Additionally, circular polarisation is shown to have a higher number of ions moving in a longitudinal direction, showing a higher flux of forward accelerated ions.

Similar figures have been made for the 15 nm where the final stages of laser acceleration are looked at in detail. In Figure 5.14 it was concluded that a strong increase of transverse momentum for the high energy particles was a sign of onset of transparency. Figure 5.16a shows the ion phase space at $t = 66$ fs for a 15 nm target irradiated by a linearly polarised laser pulse. In the forward direction, two different distributions of ions are seen: those with longitudinal momentum below $0.1\, m_p c$ and those above. For the lower energy population, the particles are shown to have a range of transverse momenta with very few particles accelerated along the laser axis. These ions are taken to originate from the regions of lower a_0 or smaller accelerating gradient and hence the outer edges of the focal spot. For higher energies, a population of $10^{30}\,\mathrm{m}^{-3}$ protons are seen to be oscillating in the transverse direction on top of a background of density two orders of magnitude lower. This indicates that although the density on axis remains high, the ions are affected by the electric field of the laser. Thus, strong heating of the overdense, forward accelerating plasma slab is occurring, with a decrease into transparency expected at later times. Indeed, when observing the transmitted electric field in Figure 5.6b, an increase in radiation is detected as $t = 66$ fs and beyond.

For the case of circular polarisation, shown in Figure 5.16b, a similar effect is seen to occur but at later times. Again, the triangular ring-like structure is seen ranging from the cold target to the hot accelerated particles. A particle density of around $10^{28}\,\mathrm{m}^{-3}$ protons are seen on-axis, with strong modulations in the transverse energy direction. This implies an irregular transverse force is being applied to the higher energy particles, which could be understood as the beginning of transparency. The lower energy spread particles that extend down to the cold bulk of the target are of higher density than the linear polarisation equivalent. This implies more particles



(a) Timestep: 66 fs
Polarisation: Linear

(b) Timestep: 72 fs
Polarisation: Circular

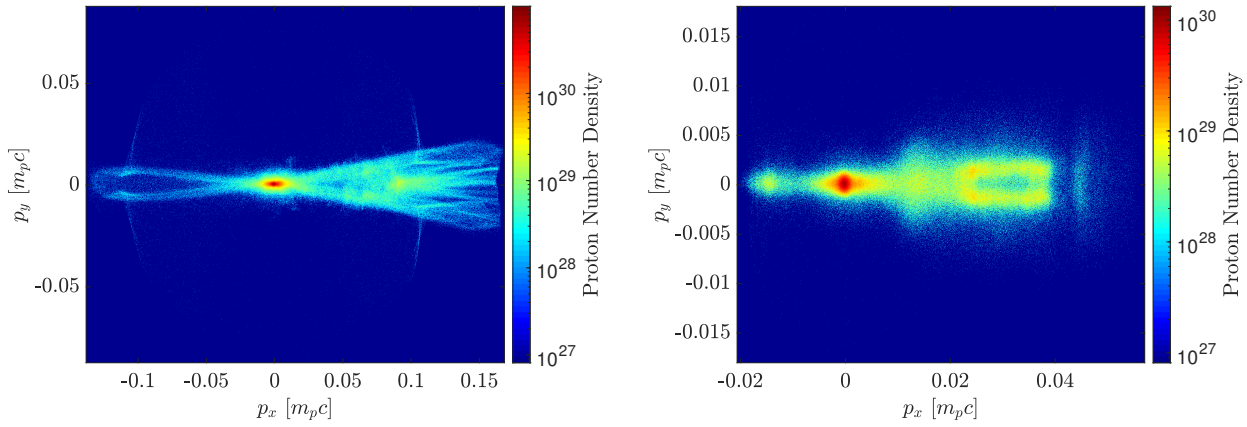
Figure 5.16: Momentum phase space at various timesteps for a 15 nm target irradiated by different polarisations

are accelerated in the transverse direction, leading to target buckling. This is indeed what is seen in Figure 5.2.

Thus, for a thickness of 15 nm, the target is shown to begin it's transition into transparency at the later stages of the laser pulse, possibly implying an efficient radiation pressure acceleration up to the peak of the pulse. For circular polarisation, severe target buckling is seen through the large number of particles accelerated transversely with a low energy spread. Particle energies for circular polarisation reach half the energies attained by linear polarisation but at much higher densities, indicating much lower target heating. Acceleration in the backward direction is also seen for both polarisations, indicating the presence of a sheath field on the front surface.

Finally, the phase space for a 50 nm target is shown for both polarisations to indicate the differences with thinner targets. Figure 5.17 shows the momentum phase space of the protons at the end of the laser pulse for a target irradiated by a linearly polarised laser pulse. A strong increase in particle density at $p_x = p_y = 0$ is seen, corresponding to $n_p = 9 \times 10^{30}$ particles, indicating that a large portion of the target remains stationary and cold. In the forward direction, a population density of around 5×10^{28} protons per cell is seen with few features below $p_x = 0.1\, m_p c$. Particle energies $\sim 75\%$ of the 15 nm target are seen, with longitudinal filaments seen at $p_x > 0.1\, m_p c$. The thermal spectrum of the ion energies, as well as the large particle number at cold temperatures points towards sheath acceleration being the dominant

acceleration mechanism for this target.



(a) Timestep: 90 fs
Polarisation: Linear

(b) Timestep: 90 fs
Polarisation: Circular

Figure 5.17: Momentum phase space at various timesteps for a 50 nm targets irradiated by different polarisations.

For a 50 nm target irradiated by a circularly polarised laser pulse, the proton phase space looks considerably different. The target is overall cooler than it's linear counterpart, as confirmed in Figure 5.4, and reflected in the momentum axis scales in Figure 5.17b that extend to around 40% of the former. In the backward direction, a small mono-energetic feature is seen with particle per cell densities of high 10^{28}. In the forward direction a constant thermal spread of particles is seen along the laser axis, with an increase in particle number between $0.02 < p_x < 0.04\, m_pc$. This features is formed from the first particles accelerated at the beginning of the laser pulse. The hard cut-off at $p_x = 0.04\, m_pc$ is due to particles leaving the simulation box.

Thus, for the 50 nm a very different ion phase space is seen compared to thinner targets. A predominantly thermal spectrum indicates sheath acceleration occurs for the majority of the laser pulse, with a small amount of radiation pressure at early times. A factor of 3 difference in magnitude of momentum is seen, showing that circular polarisation accelerates protons to much lower energies.

Finally, in order to check the validity of the simulation results, the maximum proton energy from the simulations are plotted against the maximum proton energy found experimentally in Figure 5.18. All ion energies were measured on the laser axis.

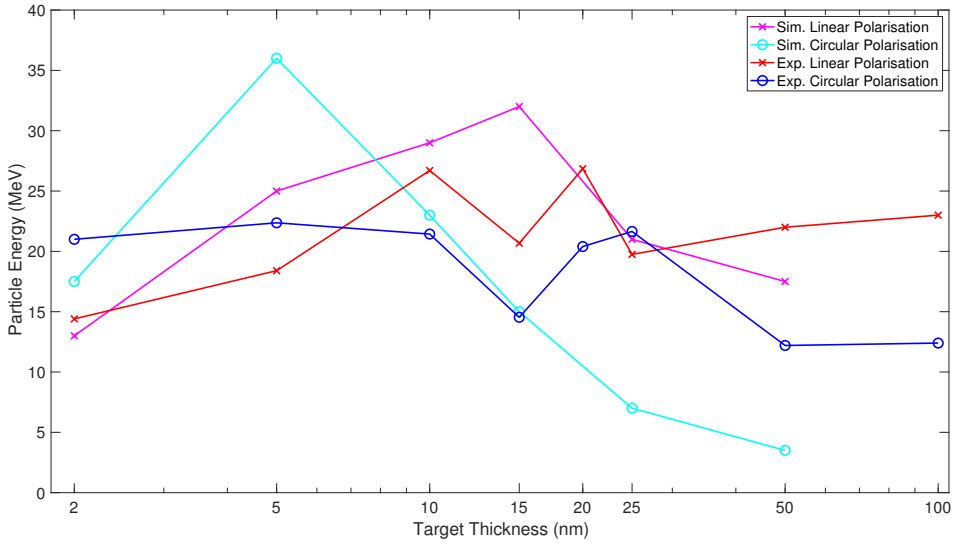


Figure 5.18: Maximum proton energy on-axis found experimentally and through simulations for linear and circularly polarised light. Experimental data provided by Aodhan McIlvenny, Queen's University Belfast.

For simulations, the energy curves follow a rise then decrease over the target thickness range. Circular polarisation sees a peak at 5 nm, whereas linear polarisation sees a peak at 15 nm. These curves, offset in target thickness, are due to different heating mechanisms causing different rates of target heating, as seen in Figure 5.4. Thus, in order to prevent the target going transparent, thicker targets are needed for more efficient proton acceleration than when using linear polarisation. A cross over between polarisations is seen between 5 and 10 nm targets, where circular polarisation produces higher energy ions for thinner targets, but the ion energies rapidly drop off for thicker targets due to the low levels of target heating, shown in Figures 5.4 and 5.3.

Experimentally, the proton energies for linear polarisation follow a different trend where a gradual increase over target thickness is seen, with a local minimum at 15 nm before dropping slightly for thicker targets. As the 2 nm target is thinner than the cold plasma skin depth, the laser field is able to penetrate and volumetrically heat the target, leading to a strong plasma expansion and a rapid decrease in electron density, as shown in Figure 5.5. Thus, the laser interacts with an overdense plasma for approximately 12 fs or 22 fs depending on polarisation, as shown in Figure 5.7, leading to low energy protons. A cross over between polarisations is again seen between 5 and 10 nm, where circular polarisation sees a plateau of the proton

energies until a target thickness of 25 nm, excluding the local minimum. In comparison, linear polarisation sees an almost doubling of proton energies, again excluding the local minimum. The decrease in proton energies for the 15 nm target for both polarisations may be due to the maximum proton energies being accelerated off axis, as seen in 3D simulations by Yin et al [119]. Subsequently, the proton energies gradually increase for linear polarisation and decrease for circular polarisation as relativistic transparency no longer occurs.

Overall a reasonable agreement between experimental and simulations results are seen, with a factor of 18% and 36% overestimation of maximum ion energies for linear and circular polarisation respectively. For the 2 nm target, the simulations underestimate the proton energies achieved by approximately 20% for both polarisations. This may be due to the lack of spatial resolution in the simulation, as a cell size of 0.6 nm was used as a compromise between run time and resolution. Thus, the target was made up of 3 cells in the longitudinal direction allowing for poor precision in the resolving of longitudinal features and leading to a less accurate representation of the plasma dynamics occurring. For the subsequent target thicknesses, simulations initialised with linear polarisation produced higher ion energies than those found experimentally which could be due to target pre-expansion from a prepulse in the case of the latter [22]. For the case of thicker targets, the prepulse may have a positive effect on the ion energies as it increases the front surface density scale length, leading to increased target heating. This would explain why for a 50 nm target the experimental energy exceeds the simulation energy.

For circular polarisation, the simulation energies obtained have relatively poor accuracy, although the approximate trend is somewhat followed. For the 2 nm target, the proton energy is underestimated by the simulations, again possibly due to the lack of resolution. For the subsequent target thickness a vastly overestimated value is found. This may be due to prepulses in the experimental conditions, as explained above. For the 5 nm and 10 nm target a very accurate measure of ion energies is obtained, however the reverse is true for the subsequent two target thicknesses. Simulations showed that target heating was strongly dependant on the laser's angle of incidence, thus if the experimental conditions entailed a deformation of the front surface either through heating with the prepulse or target surface defects, significantly higher plasma temperatures could be achieved.

5.6 Summary

In order to gain a greater insight into the experimental conditions observed in Chapter 4, simulations were run in 2D3V using the particle in cell code EPOCH. The simulation results were analysed in the same manner as the experimental results in order to further understand the trends and phenomenology of the laser plasma interaction. While some variations in quantitative results were seen between the experimental and simulation results, overall the simulations provided an accurate representation of the occurring physics and helped provide additional insight into the plasma dynamics.

The experimental results indicated that targets thinner than 25 nm became transparent during the laser-plasma interaction, with the onset of transparency shifting to later times as target thickness increased. This observation was equally visible in the simulation results, both by looking at the transmitted electric field and the evolution of the electron density in the focal spot. The concept of optical shuttering was also supported, with a decreasing temporal duration of the transmitted pulse for increasing target thickness. This effect was linked to changes in the target's front surface in Figure 5.1 and 5.2 and the electron temperature in Figure 5.4, both effects which were also strongly correlated.

When observing the quantity of transmitted light for targets of thickness 25 nm or above, the experimental results pointed to a secondary source of radiation due to a stark change in spatial profile and a quasi-constant quantity of transmitted light over the remaining target thicknesses. Following from the experimental results of the FROG, this secondary source of radiation was concluded to have originated from coherent transition radiation, emitted at both the fundamental and twice the laser's frequency. This was further confirmed in simulations, as the target was proven to have remained overdense for the duration of the laser pulse, with radiation located beyond the rear surface of an overdense plasma. The phase space of the electrons showed that the electrons were accelerated in bunches separated by 400 nm indicating an acceleration from the $J \times B$ heating, generating an oscillating electric field. Thus, the simulations confirmed the conditions necessary to produce coherent transition radiation were present during the interaction, as calculated in Section 2.5.3.

The FROG results were synthesized by taking the Wigner transform of the experimental and simulation transmitted pulses. While the limitations of the simulation set-up meant the results did not match perfectly, both set of results provided the same qualitative information on the interaction dynamics. The results correctly represented the optical shuttering effect, seen in the experimental results, by showing increasing spectral bandwidth for decreasing temporal bandwidth pulses. Both results predicted a change in plasma conditions for targets of thickness 25 nm and above, where a transmitted pulse of limited temporal and spectral bandwidth was seen.

Finally, an insight into the ion motion was presented by plotting the momentum phase space of the protons for various target thicknesses and polarisations. An initial acceleration phase through radiation pressure was seen for most targets, with the dominant acceleration mechanism being relativistic transparency for thinner targets. Above 15 nm, sheath acceleration was primarily responsible for the acceleration of ions, with reasonably faithful proton energies obtained compared to those found experimentally.

Thus, Chapter 4 and Chapter 5 provide a comprehensive review of the effect of laser polarisation in the relativistic transparency regime. Chapter 5 provided an in-depth insight into the properties of the transmitted radiation, the electron motion and the ion acceleration mechanisms in play. It confirmed the concept of optical shuttering, with a decreasing temporal duration of the transmitted pulse for increasing target thickness in thinner targets, and the generation of coherent transition radiation for thicker targets.

Chapter 6

Reflected light from ultra-intense laser-plasma interactions

This chapter discusses the results from an experimental campaign undertaken on the J-KAREN-P laser in the Kansai Photon Science Institute research laboratory in Nara, Japan, during March and May 2018. The experiment was a collaboration between scientists from the Kansai Photon Science Institute (Japan), the Helmholtz Zentrum Dresden Rossendorf Institute (Germany) and Imperial College London (UK). First, the motivation for the experiment will be discussed, including a description of the experimental set-up and parameters used. The results of the reflection screen will then be presented, showing that the reflected near-field pattern can be used to give information on the front surface reflection and formation zones for the first and second harmonic respectively. Finally, the results are contextualised within the work of this thesis.

6.1 Motivation

The primary aim of the experiment was to conduct an in-depth study of sheath acceleration at intensities of $10^{21}\,\mathrm{W\,cm^{-2}}$ with an oblique angle of incidence for targets in the range of 50 nm - 2 µm. Thin targets were used to optimise the transfer of energy into the ions, in particular

protons, and explore the transition from sheath acceleration into the relativistic transparency regime. To do this, particle spectrometers were used to measure the proton and electron energies, and reflection and transmission screens were used to measure the quantity of absorbed energy. Targets with a front or back surface coating were used to increase laser absorption, and to test the spatial origins of the accelerated ions [120]. Finally, high Z material targets were used to calculate the strength of the rear sheath field by measuring the ionisation levels of the accelerated ions.

The results presented in this chapter are based on the investigation of energy coupling into a target and it's consequential effect on the plasma dynamics and particle acceleration. The aim was to obtain a numerical value for the quantity of absorbed light based on the quantity of reflected and transmitted radiation. However, due to a larger-than expected beam divergence of the reflected light [121], no absolute measurement of the reflected energy was obtainable. From the results presented in Chapter 4 and 5, energy coupling into a target was shown to have a strong influence on the plasma dynamics that occur. Indeed, for targets below a certain threshold the plasma was seen to transition from opaque to relativistically transparent, significantly changing the experimental conditions present and consequently also the particle acceleration mechanism [44]. Despite similar experimental conditions to those presented in previous chapters (800 nm wavelength laser with 10′s fs pulse length), a three fold increase in energy on target and an oblique angle of incidence meant vacuum heating should dominate throughout the interaction. This lead to an increase in target heating and due to significantly thicker targets, the experimental conditions remained at the intersection of relativistic transparency and sheath acceleration. Thus, as a measure of energy absorption was no longer possible, a study of the relative reflected energy and target's front surface was undertaken.

Previous research has explored the spatial properties of harmonic generation on the front surface of plasma mirrors. Kahaley et al [69] found varying divergence angles for harmonic generation produced through the CWE or ROM mechanisms (See Sections 2.5.1 and 2.5.2), where CWE experienced much greater divergence (up to 0.12 rad) compared to ROM (0.04 rad). Additionally, the divergence was shown to have an intensity dependence, where for $a_0 > 1$ the divergence of the harmonic generation was found to be determined by the curvature of the target's front

surface [122]. Finally, the quantity of energy in the second harmonic signal was found to be a good indicator of the absolute intensity of target [123]. Thus, by diagnosing the reflected light using a scatter screen, information on the relative reflected energy and harmonic generation mechanism could be obtained.

6.2 Experimental Set-Up

6.2.1 Laser

The Kansai Photon Science Institute (Japan) is home to the J-KAREN-P laser, a 30 fs, 30 J Ti:sapphire laser with a repetition rate of 0.1 Hz. Commissioned in 2018, it can reach intensities up to mid $10^{21}\,\mathrm{W\,cm^{-2}}$ with a contrast ratio of 10^{-12}. An average of $13\,\mathrm{J} \pm 2.2\,\mathrm{J}$ is delivered on target and focused down to a $1.5 \times 2.8\,\mu\mathrm{m}$ focal spot by a $f/1.4$ parabola, achieving a Strehl ratio of 0.9. Thus intensities of $3.3 \pm 0.3 \times 10^{21}\,\mathrm{W\,cm^{-2}}$ and a maximum a_0 of 39 ± 2 are achieved.

A summary of the laser parameters is given in table 6.1.

Parameters	Value
Mean Energy on target	$13 \pm 2.2\,\mathrm{J}$
Focal Spot Size	$\sim 2\,\mu\mathrm{m}$
Pulse Length	30 fs
Intensity at focus	$3.3 \pm 0.3 \times 10^{21}\,\mathrm{W\,cm^{-2}}$
a_0 at focus	39 ± 2

Table 6.1: List of experimental parameters used in the J-KAREN-P 2018 run.

6.2.2 Experimental Layout

Figure 6.1 shows the experimental set-up for the J-KAREN-P experiment in March and May 2018. The laser is focused by the $f/1.4$ parabola and incident on the target at an angle of 45°

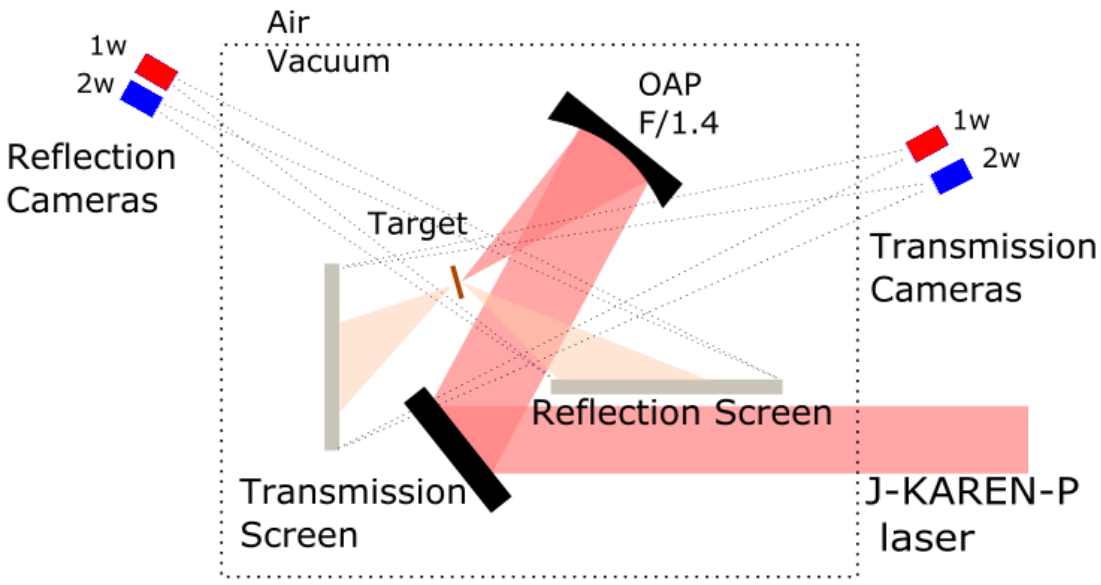


Figure 6.1: The experimental set-up

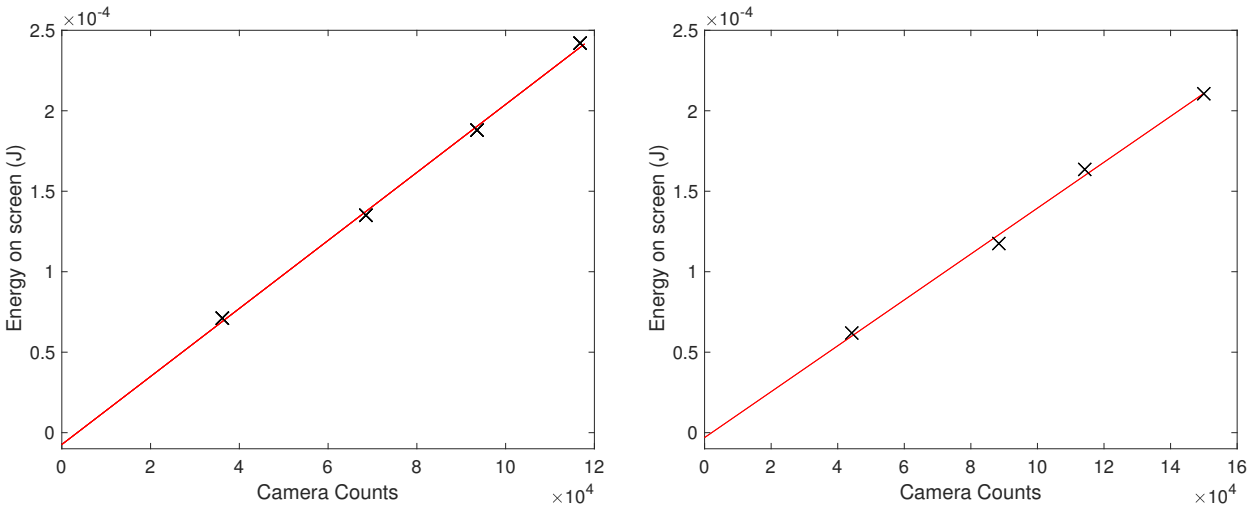
to the target. PTFE screens intercept the reflected and transmitted beams, allowing for the light to be imaged by cameras through 1ω and 2ω interference filters.

The targets used in this experiment were thin foils of silver in the range of 50 nm to 2 µm. All targets were shot at a 45° angle to avoid damage to the optics from back reflections.

6.2.3 Diagnostic: Reflection Screen

The reflected light was diagnosed by placing a scatter screen 36 cm wide and 18 cm high in the reflected beam and imaging it through a chamber window with two cameras. The cameras were equipped with interference filters for the first and second laser harmonic and thus give both spatial and quantitative information on the reflected beam in those harmonics.

The energy calibration of the cameras was done by picking off a known quantity of the laser's near field and redirecting it onto the reflection screen. During target shots, however, it was found that the reflected beam over filled the reflection screen due to plasma effects. Thus only a relative energy measurement was obtained. The calibration curves are given in Figure 6.2 for reference.



(a) Calibration of the 1ω reflection camera (b) Calibration of the 2ω reflection camera

Figure 6.2: Calibration curves of the reflection cameras.

6.3 Characterisation of the Reflected Beam

A PTFE reflection screen was placed in the reflected laser beam in order to obtain an image of the near field and gain information on the dynamics of the target's front surface. This is shown in Figure 6.3, where the spatial profile of the reflected beam for silver targets of thickness 300 nm and 500 nm at various focus positions of the main beam are given. For each position in the focus scan, the near field of the reflected laser beam is show on the left, with the respective far field shown on the right.

To calculate the far field, first the spatial image was modified to compensate for camera and intersection angle. The methodology is described in Section 3.4. The electric field pattern was then computed and the 2D fast Fourier transform of the resultant pattern was taken. To aid comparison, all comparable images are on the same colour bar, i.e. all far field images are on the same colour scale, with the $2\,\omega$ images requiring a 10 times multiplication in number of counts. Note the far field images have been cropped to see the region of interest and are presented on a logarithmic colour scale. For the focus scan, each target is moved by 30 µm in and out of focus. A shift of the target closer to the parabola corresponds to a negative distance, whereas shifting the target away from the parabola consists of a positive distance. The initial focus spot size can be approximated to $\sim 2\,\mu$m and thus a displacement of 30 µm results in a focus spot of $\sim$

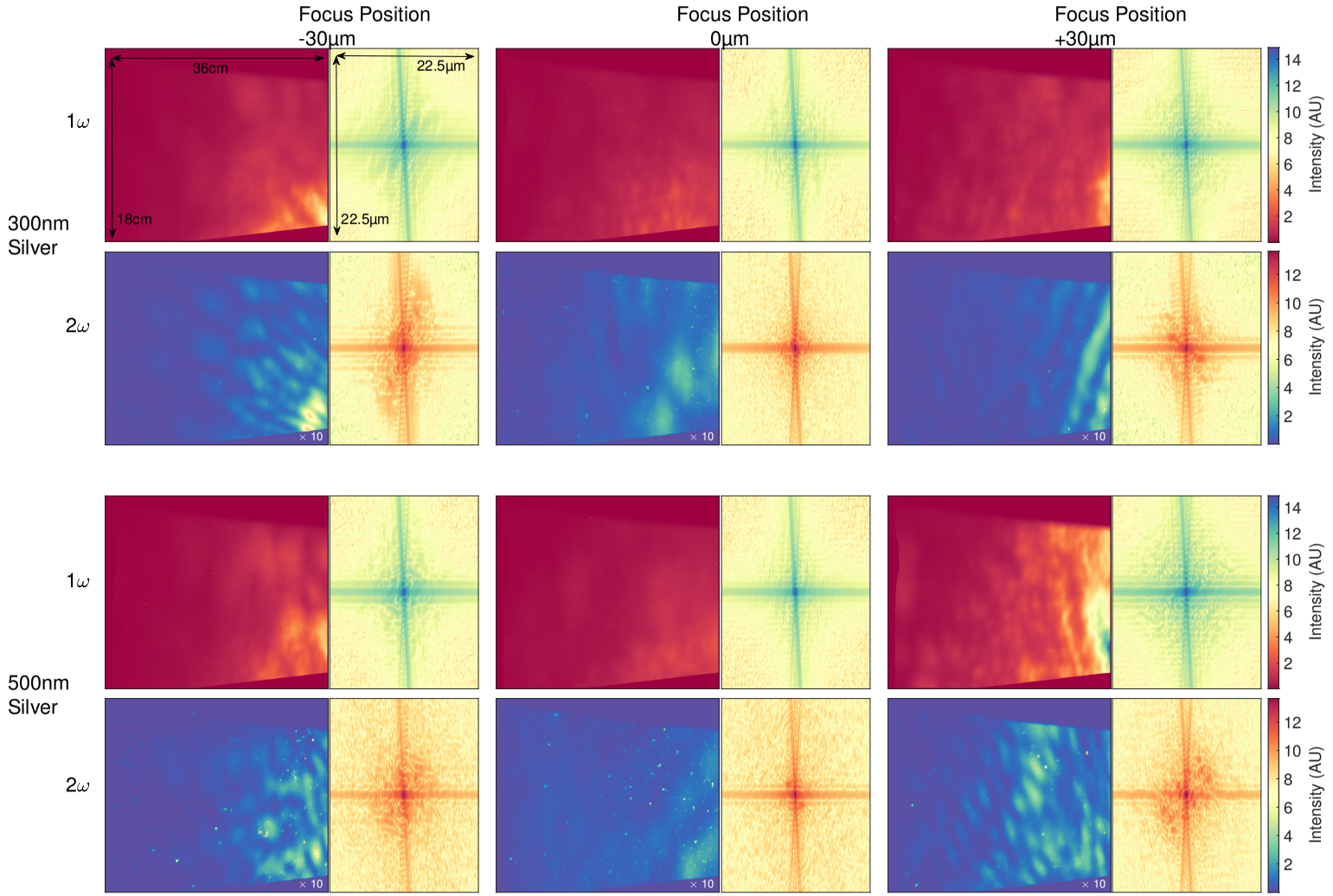


Figure 6.3: Normalised spatial beam profile for the reflected light for 1ω and 2ω light. For each focal position and laser harmonic the spatial beam pattern is shown on the left and the Fourier transform is shown on the right. The reflected spatial beam patterns are shown on a linear colour scale, with the cropped Fourier transform images shown on a logarithmic colour scale. Note the non rectangular shape of the reflection screen is due to a 45° angle between the reflected beam and the screen. The number on the lower right corner of the 2ω spatial images corresponds to the multiplication factor necessary to put all spatial images on the same colour scale.

21 µm.

For the laser near field, distinct spatial patterns can be seen for different target positions, laser harmonics and target thickness. For the first harmonic, the spatial patterns are more diffuse with larger features (∼8 cm) than for the second harmonic (∼3 cm). The latter shows a higher frequency of spatial features that are circular and small in size. The frequency of spatial structures increases out of focus for both harmonics, in a continuation of the in-focus features. The intensity patterns for all cases vary both vertically and horizontally, implying interference.

From optics, the distribution of the electric field of a laser beam in the near field is related to the field distribution at focus by the Fourier transform. Thus, by taking the Fourier transform of the amplitude of radiation in the near field, as seen on the reflection screen, and multiplying it by it's complex conjugate to get a measure of intensity, an image of the radiation region on the target's front surface could be formed. For the first harmonic, this region represents the reflection region, whereas for the second harmonic it represents the formation zone. For a target placed at focus, the far field in the first harmonic shows a high intensity spot corresponding to low spatial frequencies, as would be expected from a diffraction limited focal spot. When the target is moved out of focus, the halo of higher spatial frequencies increases in intensity. This is due to the higher frequency components of the focal spot being spread over a larger area and at lower intensities, resulting in more reflection. For the second harmonic this phenomena is more evident, with more higher spatial frequencies produced on targets outside of focus. As the Fourier transform here also corresponds to the laser far field in real-space, shifting out of focus in the first harmonic sees the energy of the laser pulse spread over an increased area. This causes lower overall intensity, as would be expected through geometry, and an increased area of reflection, as shown in Figure 6.3.

For the second harmonic, the reflection region is seen to be similar to the first harmonic region but with a much sharper intensity drop off at higher spatial frequencies. This might imply a intensity dependence on second harmonic generation, where for too low an intensity the density scale length is too sharp and the target is too cold to sustain the necessary surface oscillations. Additionally, the formation region of the second harmonic is shown to have an

angular dependence that varies between shots. This may be due to astigmatism in the laser beam or spatial variations on the plasma surface. Finally, the experimental trends were seen to be similar for both target thicknesses, confirming the validity of the results.

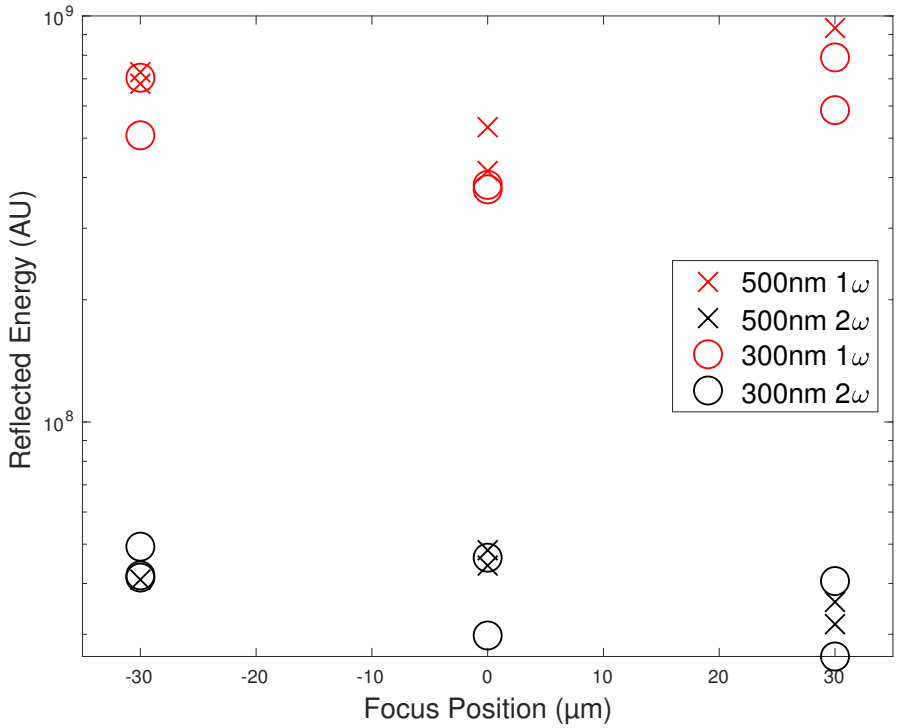


Figure 6.4: Quantity of reflected energy for 1ω and 2ω light at different focus positions. A positive displacement corresponds to a shift away from the parabola, and a negative displacement a shift towards the parabola.

The reflection screen was also used to provide a relative measure of the reflected energy, as shown in Figure 6.4. During the experiment, the reflected beam was seen to over fill the reflection screen due to the plasma front surface modifying the beam's divergence. Thus, an absolute measurement of the reflected energy could not be obtained. However, by assuming that the reflection screen captured the majority of the reflected beam and for each shot the beam divergence was the same, a relative measure of the reflected energy can be taken. Figure 6.4 plots the quantity of reflected light with respect to focus position for both harmonics and both target thicknesses. The first harmonic light is plotted in red, and the second harmonic light in black. The reflected energy corresponding to the 500 nm target is shown by crosses, whereas circles represent the reflected energy for the 300 nm target. Figure 6.4 shows an increased amount of first harmonic light reflected off targets placed out of focus. This is true for both target

thicknesses, and in both directions of displacement. The trend is slightly asymmetric, with a slight increase in reflection for targets moved in the positive direction away from parabola. Comparatively, the second harmonic shows only very subtle differences in reflected energy for targets moving in and out of focus. A slight decrease in reflected energy is seen for targets moved away from the parabola, with the remaining focus positions reflecting a quasi-constant value.

When a laser pulse is at focus, the intensity is at it's highest with steep radial intensity gradients. Thus it can be assumed that most of the laser energy is contained in a spatial area $\approx 4\,\mu m^2$. For shots out of focus, the focal spot increases by a factor of 10, and thus the intensity drops by a factor of 100. Absorption is heavily dependent on intensity, in particular for vacuum heating and for intensities $>10^{18}\,W\,cm^{-2}$ [60]. However, for the out of focus shots a larger area of the target is illuminated. Thus for the first harmonic, absorption is maximised at best focus, with an increase in reflectivity seen for out of focus positions, as shown in Figure 6.4.

Little difference in signal levels is seen for the second harmonic, implying the efficiency in production is quasi equal at both focal positions and for both different intensities. Indeed, second harmonic production at these intensities ($10^{19} - 10^{21}\,W\,cm^{-2}$) is dominated by the ROM model where the phase of the incoming photons is redistributed such that higher harmonic are produced [123]. Previous studies have shown that above an intensity of $10^{19}\,W\,cm^{-2}$ a constant amount of second harmonic radiation is produced as at higher intensities energy is deposited in higher order harmonics. The ROM mechanism depends heavily on the density scale length [69] [70] and the position of the critical surface. Therefore, for the case of the in-focus shots, buckling of the targets front surface may cause the created radiation to be emitted in a much larger solid angle, limiting the collection efficiency of the imaging system and thus the recorded intensity.

Finally, the relative measure of reflected energy was plotted for a range of silver target thicknesses in Figure 6.5. The first harmonic is represented by crosses and the second harmonic by circles. The shots taken 30 µm out of focus are shown in red. The quantity of reflected energy is seen to decrease for decreasing target thickness, in both the first and second harmonic.

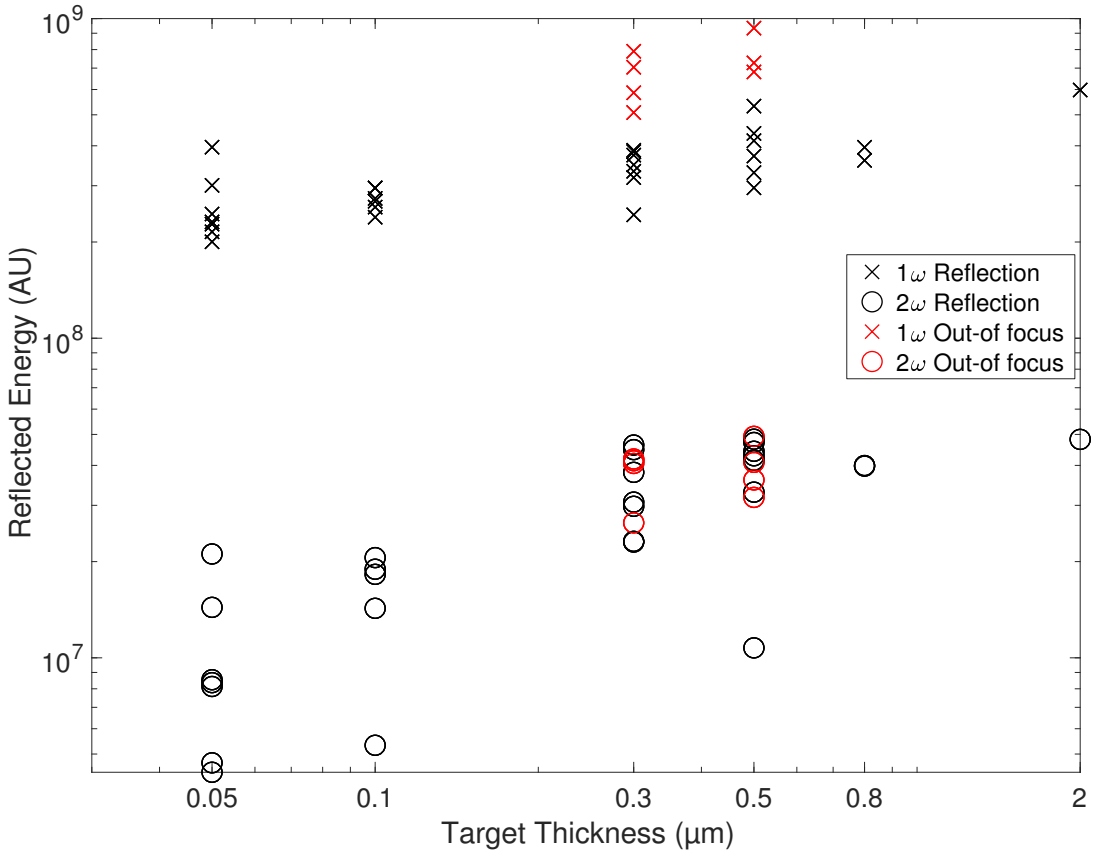


Figure 6.5: Reflected energy for a thickness scan where the first harmonic is shown by crosses and the second harmonic by circles. Each data point represents a laser shot. Shots taken with a target at focus are shown in black, with the out of focus shots included in red.

For this experiment, the target thicknesses were chosen such that they spanned the sheath acceleration and relativistic transparency regime. As studied in detail in Chapter 4 and Chapter 5, thinner targets transition into a relativistic transparent regime earlier on in the laser pulse, and hence reflect less energy due to both absorption or transmission. Despite the targets being thicker than those in the previous chapters (50 nm - 2 μm instead of 2 nm - 100 nm), the oblique angle of incidence meant similar experimental conditions were seen.

Figure 6.5 can therefore be considered as an indication of target heating, and a relative temporal measurement of it's transition into transparency. For thinner targets, less energy is reflected as it is absorbed or transmitted. As the target thickness increases, the quantity of reflected light increases and starts to plateau. This could be considered the transition region between targets that undergo transparency and those that stay fully opaque for the duration of the laser pulse.

Thus, for a known laser system and calibrated diagnostic, the quantity of reflected light could be used as an indication of transparency. This diagnostic could then also be used as a measure of the target's position with respect to focus by minimising the reflectivity.

Finally, a similar trend with a larger variation in magnitude is seen for the second harmonic. As $2\,\omega$ production depends on the motion of the critical surface, the quantity of second harmonic reflected is an indication of the oscillation of the plasma surface and potentially also the density scale length. This hypothesis remains to be proven in future works and through simulations.

6.4 Conclusion

Thus, to conclude, interesting spatial patterns were seen in the reflected beam with the frequency of spatial features increasing as the target was moved out of focus. Taking the Fourier transform of these spatial patterns allowed for information on the targets front surface to be obtained. A clear change in size of reflection or formation region was seen when moving the target in or out of focus, in agreement with the corresponding change in size of focus spot. A similar trend was seen in Figure 6.4, where the reflected energy was plotted against focus position. This showed a factor of 2 or more energy reflected whilst out of focus, in agreement with less energy absorbed for lower intensities on target. Finally, the quantity of reflected light was plotted for a range of target thicknesses, with the amount of reflected energy increasing for increasing target thicknesses, before plateauing out an order of magnitude higher at thicker targets. In future and after calibration, the reflection diagnostic could be used as a relative temporal measure of transparency, as well as give information on the positioning of the target with respect to the laser focus. The second harmonic radiation produced could also be used as an indication of the motion of the critical surface.

Chapter 7

Conclusion and Future Work

In the field of ion acceleration using solid density targets, understanding the temporal evolution of the plasma and it's properties is of critical importance when seeking to optimise the energy transfer from the laser to the particles. This thesis presented results from various experimental campaigns exploring the trends in transmitted and reflected light as an measure of target heating and it's density evolution with time. This chapter summarises the work presented in this thesis and suggests areas of future work.

7.1 Thin foils at normal incidence

Chapter 4 presented results from an experimental campaign run on the GEMINI laser at the Rutherford Appleton Laboratory, UK. Carbon targets in the range of 2 - 100 nm were shot at normal incidence by a laser of a_0= 12.5 and the reflected and transmitted energy and beam profile were observed. This allowed for a detailed analysis of target heating to be conducted, with variables including the target thickness, laser polarisation and laser harmonic.

By varying the target thickness, the limit of opacity for the given experimental parameters was found to be 25 nm. Targets below this were seen to go transparent during the laser-plasma interaction due to their thermal expansion and decreasing density. A linearly polarised pulse

was shown to heat targets more substantially than circular polarisation, as for targets <25 nm the transmitted pulse lengths were on average 5% longer for linear polarisation. This resulted in a 10% increase in transmission of $1\,\omega$ light. For thicker targets ≥25 nm, those irradiated by a linearly polarised pulse saw a factor of ~ 50 increase in energy absorption compared to circular polarisation, due to the latter's up-to 40 fold increase in reflectivity. This behaviour was attributed to the $\mathbf{J} \times \mathbf{B}$ heating mechanism which is heavily suppressed for circular polarisation, resulting in a colder and hence more reflective, laser-plasma interaction.

A study of the second harmonic generation was also completed, which saw production in both the forward and backward direction for all target thicknesses. Optimum $2\,\omega$ generation in both the front and back direction was seen for a 15 nm target.

A temporal measurement of the $1\,\omega$ transmitted light was taken using a FROG, allowing for a measurement of the transmitted electric field and phase. For increasing target thickness pulses of decreasing length from 46 - 40 fs were seen to transmit through the target. For thin targets and longer transmitted pulses, significant blue then red shifting of the pulse was seen due to the initial self-phase modulation then later transmission through the expanding target. Targets irradiated by a linearly polarised pulse were shown to transmits pulses 5% longer than for a circularly polarised pulse. For targets of thickness 25 nm or above, FROG traces were only measured when linear polarisation was used. This was due to the enhanced target heating causing relativistic electron bunches to be accelerated to the rear surface and generating coherent transition radiation.

Simulations of the above interactions were presented in Chapter 5 where more quantitative results of electron heating and density variation were obtained. The hypothesis of optical shuttering was confirmed when analysing the transmitted electric field, where targets of decreasing thickness were shown to transition below the relativistic critical density at earlier times. The density variations were shown to follow an exponential decrease with changing rate as the target transitioned into transparency. The density drop was shown to have strong correlations with the electron temperature, as the maximum hot electron temperature for each target thickness was shown to be reached at the point of transparency. A maximum hot electron temperature of

1.6 MeV was measured for a 10 nm target, with targets ≥25 nm reaching electron temperatures of ∼1 MeV. This confirmed the presence of relativistic electrons, and a plot of longitudinal momentum p_x against transverse momentum p_y confirmed their bunch structure, thus proving the occurrence of the coherent transition radiation as measured by the FROG.

Finally as a benchmark, the particle data from the simulations was compared to the experimental values of maximum proton energy for each target thickness. Similar trends for experimental and simulation results were seen for linear polarisation, where targets ≤ 15 nm showed enhanced proton energies. For circular polarisation, the behaviour shown in simulations differs from that seen experimentally, in particular for targets ≥25 nm, suggesting the polarisation used experimentally was not perfectly circular. Quantitatively, a factor of 18% and 36% overestimation of maximum ion energies was seen for linear and circular polarisation respectively. The accuracy of the predicted simulation ion energies dropped as target thickness decreased; for the 2 nm target, the simulations underestimated the proton energies achieved by approximately 20% for both polarisations. This was considered to be due to the lack of longitudinal resolution, where a cell size of 0.6 nm was used as compromise between run time, particle per cell number and resolution.

7.2 Thin foils at oblique incidence

Chapter 6 presented results from a similar experiment where targets of thickness 75 nm - 2 µm were irradiated by a laser pulse of $a_0 = 39$ at a 45° angle. Here, the reflected light was diagnosed as a function of target thickness and position in focus, and the resonant and vacuum heating mechanisms were deemed to be predominant. The reflectivity of targets observed through focus showed high spatial frequency components were preferentially reflected out of focus, with an increase in absorption at the highest intensities. For the second harmonic generation, a strong intensity dependence was shown due to the rapid cut off at higher frequencies. It was assumed that for too low values of I, the target did not experience sufficient heating to sustain the critical surface oscillations necessary for $2\,\omega$ production. As the Fourier transform also corresponded

to the far field in real space, an image of the target's front surface could be obtained. Finally a plot of reflectivity against target thickness showed reflectivity was directly correlated with target thickness for both laser harmonics. For the second harmonic however, no change in quantity of reflected energy was seen when shifting the target's focal position.

The reason behind this phenomenon remains to be investigated either through simulations, or through further experimental probing. By increasing the size of the reflection screen such that the whole beam is captured, the change in reflected beam divergence could be measured and would have no influence on the quantity of reflected light. This would allow for the trend to be confirmed and for the dominant second harmonic generation mechanism to be identified (See Section 2.5). Finally, by also considering the quantity of transmitted light, a measure of energy absorbed for each target thickness and focal position could be calculated.

7.3 Future Work

The work done in Chapters 4 and 5 have provided a comprehensive and quantitative description of plasma properties and it's evolution at the limit of opacity. Further study could be done by fully capturing the reflected beam and installing a reflected FROG. This would allow for the total amount of absorbed energy to be calculated, and measure the temporal evolution of the interaction. Thus, a more detailed experimental study on the rate of target heating could be done, gaining more information on the target's evolution and energy transfer mechanisms with time.

Chapter 4 presented a novel technique for measuring the temporal duration of the hot electron beam. A large amount of analysis and supporting simulations were required to prove the origin of the radiation as coherent transition radiation, however in future this could be done using polarimetry. As CTR is radially polarised, a simple Wollaston prism can be used to separate the transmitted beam into the two orthogonal polarisations, thus separating the laser pulse and the CTR. This new technique could be applied on a variety of experiments both using solid density targets, for ion acceleration or harmonic generation, or gas targets, for wakefield

generation.

7.4 Impact on the Field

The work presented in this thesis introduced a novel way of using an existing diagnostic to measure the temporal evolution of the electron beam in short-pulse laser plasma interactions. Already adopted by the field [124], it allows for a new temporal dimension to be added to the previously only time-integrated measurement of the electron beam. Gaining a better understanding of the rate of energy transfer to the electrons, by diagnosing the subsequently produced CTR, further information can be gleaned on its transfer to the ions. This information could possibility lead to further optimisation of the ion energies through better understanding of the interaction dynamics, and open-up the technology to more real-world applications.

Secondly, by comparing the temporal measurement of CTR to the produced electron and ion spectra and transmitted and reflected light, it may be possible to find a correlation such that the ion spectra can be inferred from the results of the optical diagnostics. If such a technique where possible, it would open up the field to many applications that require a non-destructive measurement of the delivered ion beam. Such measurements would therefore lower the barrier to the implementation of laser-driven ion beams.

Finally, from a purely research perspective, further understanding of the electron heating mechanisms under experimental conditions, this time on a temporal scale, could lead to an improved stability in the ion beams produced by identifying the important factors and how they can be controlled.

Bibliography

[1] IoP, "Case study: Lasers." [Online] https://www.iop.org/cs/page_43644.html, accessed 2019-06-13. 1

[2] D. Strickland and G. Mourou, "Compression of Amplified Chirped Optical Pulses *," *Opt. Commun.*, vol. 56, no. 3, pp. 219–221, 1985. 2

[3] T. Wangler, *RF Linear Accelerators*. John Wiley & Sons, 2 ed., 2008. 3

[4] S. P. Mangles, C. D. Murphy, Z. Najmudin, A. G. Thomas, J. L. Collier, A. E. Dangor, E. J. Divall, P. S. Foster, J. G. Gallacher, C. J. Hooker, D. A. Jaroszynski, A. J. Langley, W. B. Mori, P. A. Norreys, F. S. Tsung, R. Viskup, B. R. Walton, and K. Krushelnick, "Monoenergetic beams of relativistic electrons from intense laser-plasma interactions," *Nature*, vol. 431, no. 7008, pp. 535–538, 2004. 3

[5] P. Mason, M. Divoký, K. Ertel, J. Pilař, T. Butcher, M. Hanuš, S. Banerjee, J. Phillips, J. Smith, M. De Vido, A. Lucianetti, C. Hernandez-Gomez, C. Edwards, T. Mocek, and J. Collier, "Kilowatt average power 100 J-level diode pumped solid state laser," *Optica*, vol. 4, no. 4, p. 438, 2017. 3

[6] J. Nuckolls, L. Wood, A. Thiessen, and G. Zimmerman, "Laser compression of matter to super-high densities: Thermonuclear (CTR) applications," *Nature*, vol. 239, no. 5368, pp. 139–142, 1972. 4

[7] J. Lindl, "Development of the indirect-drive approach to inertial confinement fusion and the target physics basis for ignition and gain," *Phys. Plasmas*, vol. 2, no. 11, pp. 3933–4024, 1995. 4

[8] M. Tabak, J. Hammer, M. E. Glinsky, W. L. Kruer, S. C. Wilks, J. Woodworth, E. M. Campbell, M. D. Perry, and R. J. Mason, "Ignition and high gain with ultrapowerful lasers," *Phys. Plasmas*, vol. 1, no. 5, pp. 1626–1634, 1994. 4, 5

[9] S. Le Pape, L. F. Berzak Hopkins, L. Divol, A. Pak, E. L. Dewald, S. Bhandarkar, L. R. Bennedetti, T. Bunn, J. Biener, J. Crippen, D. Casey, D. Edgell, D. N. Fittinghoff, M. Gatu-Johnson, C. Goyon, S. Haan, R. Hatarik, M. Havre, D. D. Ho, N. Izumi, J. Jaquez, S. F. Khan, G. A. Kyrala, T. Ma, A. J. Mackinnon, A. G. Macphee, B. J. Macgowan, N. B. Meezan, J. Milovich, M. Millot, P. Michel, S. R. Nagel, A. Nikroo, P. Patel, J. Ralph, J. S. Ross, N. G. Rice, D. Strozzi, M. Stadermann, P. Volegov, C. Yeamans, C. Weber, C. Wild, D. Callahan, and O. A. Hurricane, "Fusion Energy Output Greater than the Kinetic Energy of an Imploding Shell at the National Ignition Facility," *Phys. Rev. Lett.*, vol. 120, no. 24, p. 245003, 2018. 4

[10] M. Roth, T. E. Cowan, M. H. Key, S. P. Hatchett, C. Brown, W. Fountain, J. Johnson, D. M. Pennington, R. A. Snavely, S. C. Wilks, K. Yasuike, H. Ruhl, F. Pegoraro, S. V. Bulanov, E. M. Campbell, M. D. Perry, and H. Powell, "Fast Ignition by Intense Laser-Accelerated Proton Beams," *Phys. Rev. Lett.*, vol. 86, no. 3, pp. 436–439, 2001. 4

[11] M. Roth, T. E. Cowan, M. H. Key, S. P. Hatchett, C. Brown, W. Fountain, J. Johnson, D. M. Pennington, R. a. Snavely, S. C. Wilks, K. Yasuike, H. Ruhl, F. Pegoraro, S. V. Bulanov, E. M. Campbell, M. D. Perry, and H. Powell, "Fast Ignition by Intense Laser-Accelerated Proton Beams," *Phys. Rev. Lett.*, vol. 86, no. 3, pp. 436–439, 2001. 5, 6

[12] S. Jacquemot, "Inertial confinement fusion for energy: Overview of the ongoing experimental, theoretical and numerical studies," *Nucl. Fusion*, vol. 57, no. 10, 2017. 5

[13] G. Aiello, J. Aubert, L. Forest, J. C. Jaboulay, A. Li Puma, and L. V. Boccaccini, "Design of the helium cooled lithium lead breeding blanket in CEA: From TBM to DEMO," *Nucl. Fusion*, vol. 57, no. 4, 2017. 5

[14] R. R. Wilson, "Radiological use of fast protons.," *Radiology*, vol. 47, no. 5, pp. 487–491, 1946. 6

[15] J. F. Ziegler, M. D. Ziegler, and J. P. Biersack, "SRIM - The stopping and range of ions in matter (2010)," *Nucl. Instruments Methods Phys. Res. Sect. B Beam Interact. with Mater. Atoms*, vol. 268, no. 11-12, pp. 1818–1823, 2010. 6, 7

[16] U. Linz and J. Alonso, "What will it take for laser driven proton accelerators to be applied to tumor therapy?," *Phys. Rev. Spec. Top. - Accel. Beams*, vol. 10, no. 9, pp. 1–8, 2007. 6

[17] U. Linz and J. Alonso, "Laser-driven ion accelerators for tumor therapy revisited," *Phys. Rev. Accel. Beams*, vol. 19, no. 12, pp. 1–8, 2016. 6

[18] D. Sardari, R. Maleki, H. Samavat, and A. Esmaeeli, "Measurement of depth-dose of linear accelerator and simulation by use of Geant4 computer code," *Reports Pract. Oncol. Radiother.*, vol. 15, no. 3, pp. 64–68, 2010. 7

[19] R. Trebino, *Frequency-Resolved Optical Gating: The measurement of ultra-short Laser Pulses*. Kluwer Academic Publishers, 2002. 13, 42, 43

[20] S. N. Chen, M. Vranic, T. Gangolf, E. Boella, and P. Antici, "Collimated protons accelerated from an overdense gas jet irradiated by a 1 m wavelength high-intensity short-pulse laser," pp. 1–22. 14

[21] S. G. Rykovanov, J. Schreiber, J. Meyer-ter Vehn, C. Bellei, A. Henig, H. C. Wu, and M. Geissler, "Ion acceleration with ultra-thin foils using elliptically polarized laser pulses," *New J. Phys.*, vol. 10, 2008. 21, 32

[22] P. Gibbon, *Short Pulse Laser Interactions with Matter*. Imperial College Press, 2005. 23, 115

[23] A. Zigler, Y. Ehrlich, C. Cohen, J. Krall, and P. Sprangle, "Optical guiding of high-intensity laser pulses in a long plasma channel formed by a slow capillary discharge," *Josa B*, vol. 13, no. 1, pp. 68–71, 1996. 23

[24] E. Esarey, P. Sprangle, J. Krall, and A. Ting, "Self-focusing and guiding of short laser pulses in ionizing gases and plasmas," *IEEE J. Quantum Electron.*, vol. 33, no. 11, pp. 1879–1914, 1997. 23

[25] A. Sgattoni, P. Londrillo, A. MacChi, and M. Passoni, "Laser ion acceleration using a solid target coupled with a low-density layer," *Phys. Rev. E - Stat. Nonlinear, Soft Matter Phys.*, vol. 85, no. 3, pp. 1–9, 2012. 23

[26] A. M. M. Hussien, *Ionization of Diatomic Molecules in Intense Laser Fields*. PhD thesis, 2015. 24

[27] L. Keldysh, "Ionisation in the field of a strong electromagnetic wave," *Sov. Phys. JETP*, vol. 20, no. 5, pp. 1307–1314, 1965. 23

[28] S. C. Wilks and W. L. Kruer, "Absorption of ultrashort, ultra-intense laser light by solids and overdense plasmas," *IEEE J. Quantum Electron.*, vol. 33, no. 11, pp. 1954–1968, 1997. 25

[29] W. L. Kruer, *The Physics of Laser Plamsa Interactions*. ABP, 2003. 25, 26

[30] W. L. Kruer and K. Estabrook, "JXB heating by very intense laser light," *Phys. Fluids*, vol. 28, no. 1, pp. 430–432, 1985. 27

[31] S. P. Hatchett, C. G. Brown, T. E. Cowan, E. A. Henry, J. S. Johnson, M. H. Key, J. A. Koch, A. B. Langdon, B. F. Lasinski, R. W. Lee, A. J. Mackinnon, D. M. Pennington, M. D. Perry, T. W. Phillips, M. Roth, T. C. Sangster, M. S. Singh, R. A. Snavely, M. A. Stoyer, S. C. Wilks, and K. Yasuike, "Electron, photon, and ion beams from the relativistic interaction of Petawatt laser pulses with solid targets," *Phys. Plasmas*, vol. 7, no. 5, pp. 2076–2082, 2000. 28

[32] S. C. Wilks, A. B. Langdon, T. E. Cowan, M. Roth, M. Singh, S. Hatchett, M. H. Key, D. Pennington, A. MacKinnon, and R. A. Snavely, "Energetic proton generation in ultra-intense laser-solid interactions," *Phys. Plasmas*, vol. 8, no. 2, pp. 542–549, 2001. 28

[33] R. A. Snavely, M. H. Key, S. P. Hatchett, I. E. Cowan, M. Roth, T. W. Phillips, M. A. Stoyer, E. A. Henry, T. C. Sangster, M. S. Singh, S. C. Wilks, A. MacKinnon, A. Offenberger, D. M. Pennington, K. Yasuike, A. B. Langdon, B. F. Lasinski, J. Johnson, M. D. Perry, and E. M. Campbell, "Intense high-energy proton beams from petawatt-laser irradiation of solids," *Phys. Rev. Lett.*, vol. 85, no. 14, pp. 2945–2948, 2000. 28

[34] A. J. Mackinnon, Y. Sentoku, P. K. Patel, D. W. Price, S. Hatchett, M. H. Key, C. Andersen, R. Snavely, and R. R. Freeman, "Enhancement of proton acceleration by hot-electron recirculation in thin foils irradiated by ultraintense laser pulses," *Phys. Rev. Lett.*, vol. 88, no. 21, pp. 2150061–2150064, 2002. 28

[35] M. Borghesi, J. Fuchs, and O. Willi, "Laser-accelerated high-energy ions: State of-the-art and applications," *J. Phys. Conf. Ser.*, vol. 58, no. 1, pp. 74–80, 2007. 29

[36] J. Denavit, "Collisionless plasma expansion into a vacuum," *Phys. Fluids*, vol. 22, no. 7, pp. 1384–1392, 1979. 28

[37] A. V. Gurevich and A. P. Meshcherkin, "Ion acceleration in an expanding plasma," *Sov. Phys. JETP*, pp. 937–945, 1981. 28

[38] A. Pukhov, "Three-dimensional simulations of ion acceleration from a foil irradiated by a short-pulse laser," *Phys. Rev. Lett.*, vol. 86, no. 16, pp. 3562–3565, 2001. 28

[39] H. Ruhl, S. V. Bulanov, T. E. Cowan, T. V. Liseikina, P. Nickles, F. Pegoraro, M. Roth, and W. Sandner, "Computer Simulation of the Three-Dimensional Regime of Proton Acceleration in the Interaction of Laser Radiation with a Thin Spherical Target," *Plasma Phys. Reports*, vol. 27, no. 5, pp. 363–371, 2001. 28

[40] P. Mora, "Plasma Expansion into a Vacuum," *Phys. Rev. Lett.*, vol. 90, no. May, pp. 16–19, 2003. 28, 29

[41] P. Mora, "Collisionless expansion of a Gaussian plasma into a vacuum," *Phys. Plasmas*, vol. 12, no. 11, pp. 1–8, 2005. 28

[42] S. Buffechoux, J. Psikal, M. Nakatsutsumi, L. Romagnani, A. Andreev, K. Zeil, M. Amin, P. Antici, T. Burris-Mog, A. Compant-La-Fontaine, E. D'Humières, S. Fourmaux, S. Gaillard, F. Gobet, F. Hannachi, S. Kraft, A. Mancic, C. Plaisir, G. Sarri, M. Tarisien, T. Toncian, U. Schramm, M. Tampo, P. Audebert, O. Willi, T. E. Cowan, H. Pépin, V. Tikhonchuk, M. Borghesi, and J. Fuchs, "Hot electrons transverse refluxing in ultraintense laser-solid interactions," *Phys. Rev. Lett.*, vol. 105, no. 1, pp. 1–5, 2010. 29

[43] A. Higginson, R. J. Gray, M. King, R. J. Dance, S. D. R. Williamson, N. M. H. Butler, R. Wilson, R. Capdessus, C. Armstrong, J. S. Green, S. J. Hawkes, P. Martin, W. Q. Wei, S. R. Mirfayzi, X. H. Yuan, S. Kar, M. Borghesi, R. J. Clarke, D. Neely, and P. Mckenna, "Near-100 MeV protons via a laser-driven transparency-enhanced hybrid acceleration scheme," *Nat. Commun.*, no. 2018. 29, 33

[44] C. Scullion, D. Doria, L. Romagnani, A. Sgattoni, K. Naughton, D. R. Symes, P. McKenna, A. MacChi, M. Zepf, S. Kar, and M. Borghesi, "Polarization Dependence of Bulk Ion Acceleration from Ultrathin Foils Irradiated by High-Intensity Ultrashort Laser Pulses," *Phys. Rev. Lett.*, vol. 119, no. 5, pp. 1–6, 2017. 29, 120

[45] D. Margarone, I. J. Kim, J. Psikal, J. Kaufman, T. Mocek, I. W. Choi, L. Stolcova, J. Proska, A. Choukourov, I. Melnichuk, O. Klimo, J. Limpouch, J. H. Sung, S. K. Lee, G. Korn, and T. M. Jeong, "Laser-driven high-energy proton beam with homogeneous spatial profile from a nanosphere target," *Phys. Rev. Spec. Top. - Accel. Beams*, vol. 18, no. 7, pp. 1–7, 2015. 29

[46] J. S. Green, N. P. Dover, M. Borghesi, C. M. Brenner, F. H. Cameron, D. C. Carroll, P. S. Foster, P. Gallegos, G. Gregori, P. McKenna, C. D. Murphy, Z. Najmudin, C. A. Palmer, R. Prasad, L. Romagnani, K. E. Quinn, J. Schreiber, M. J. Streeter, S. Ter-Avetisyan, O. Tresca, M. Zepf, and D. Neely, "Enhanced proton beam collimation in the ultra-intense short pulse regime," *Plasma Phys. Control. Fusion*, vol. 56, no. 8, 2014. 29

[47] T. Esirkepov, M. Borghesi, S. V. Bulanov, G. Mourou, and T. Tajima, "Highly Efficient Relativistic-Ion Generation in the Laser-Piston Regime," *Phys. Rev. Lett.*, vol. 92, no. 17, pp. 2–5, 2004. 30, 31

[48] A. Robinson, M. Zepf, S. Kar, R. Evans, and C. Bellei, "Radiation pressure acceleration of thin foils with circularly polarized laser pulses," *New J. Phys*, vol. 10, no. 3, p. 013021, 2008. 30

[49] S. C. Wilks, W. L. Kruer, M. Tabak, and A. B. Langdon, "Absorption of ultra-intense laser pulses," *Phys. Rev. Lett.*, vol. 69, no. 9, pp. 1383–1386, 1992. 30, 33

[50] J. Denavit, "Absorption of high-intensity subpicosecond lasers on solid density targets," *Phys. Rev. Lett.*, vol. 69, no. 21, pp. 3052–3055, 1992. 30

[51] C. A. J. Palmer, J. Schreiber, S. R. Nagel, N. P. Dover, C. Bellei, F. N. Beg, S. Bott, R. J. Clarke, A. E. Dangor, S. M. Hassan, P. Hilz, D. Jung, S. Kneip, S. P. D. Mangles, K. L. Lancaster, A. Rehman, A. P. L. Robinson, C. Spindloe, J. Szerypo, M. Tatarakis, M. Yeung, M. Zepf, and Z. Najmudin, "Rayleigh-Taylor instability of an ultrathin foil accelerated by the radiation pressure of an intense laser," *Phys. Rev. Lett.*, vol. 108, no. 22, pp. 1–5, 2012. 31, 55

[52] A. P. L. Robinson, P. Gibbon, M. Zepf, S. Kar, R. G. Evans, and C. Bellei, "Relativistically correct hole-boring and ion acceleration by circularly polarized laser pulses," *Plasma Phys. Control. Fusion*, vol. 51, p. 024004, feb 2009. 32

[53] H. Daido, M. Nishiuchi, and A. S. Pirozhkov, "Review of laser-driven ion sources and their applications," *Reports Prog. Phys.*, vol. 75, no. 5, p. 056401, 2012. 32

[54] O. Buneman, "Instability, turbulence, and conductivity in current-carrying plasma," *Phys. Rev. Lett.*, vol. 1, no. 1, pp. 8–9, 1958. 32

[55] S. A. Reed, T. Matsuoka, S. Bulanov, M. Tampo, V. Chvykov, G. Kalintchenko, P. Rousseau, V. Yanovsky, R. Kodama, D. W. Litzenberg, K. Krushelnick, and A. Maksimchuk, "Relativistic plasma shutter for ultraintense laser pulses," *Appl. Phys. Lett.*, vol. 94, no. 20, pp. 3–5, 2009. 32, 70

[56] A. Henig, D. Kiefer, K. Markey, D. C. Gautier, K. A. Flippo, S. Letzring, R. P. Johnson, T. Shimada, L. Yin, B. J. Albright, K. J. Bowers, J. C. Fernández, S. G. Rykovanov, H. C.

Wu, M. Zepf, D. Jung, V. K. Liechtenstein, J. Schreiber, D. Habs, and B. M. Hegelich, "Enhanced laser-driven ion acceleration in the relativistic transparency regime," *Phys. Rev. Lett.*, vol. 103, no. 4, pp. 1–4, 2009. 32

[57] B. J. Albright, L. Yin, K. J. Bowers, B. M. Hegelich, K. A. Flippo, T. J. Kwan, and J. C. Fernández, "Relativistic Buneman instability in the laser breakout afterburner," *Phys. Plasmas*, vol. 14, no. 9, 2007. 33

[58] L. Yin, B. J. Albright, D. Jung, K. J. Bowers, R. C. Shah, S. Palaniyappan, J. C. Fernndez, and B. M. Hegelich, "Mono-energetic ion beam acceleration in solitary waves during relativistic transparency using high-contrast circularly polarized short-pulse laser and nanoscale targets," *Phys. Plasmas*, vol. 18, no. 5, 2011. 33

[59] N. P. Dover, M. J. V. Streeter, C. A. J. Palmer, H. Ahmed, B. Albertazzi, M. Borghesi, D. C. Carroll, J. Fuchs, R. Heathcote, P. Hilz, K. F. Kakolee, S. Kar, R. Kodama, A. Kon, D. A. MacLellan, P. McKenna, S. R. Nagel, M. Nakatsutsumi, D. Neely, M. M. Notley, R. Prasad, G. Scott, M. Tampo, M. Zepf, J. Schreiber, and Z. Najmudin, "Buffered spectrally-peaked proton beams in the relativistic-transparency regime," *New J. Phys*, 2014. 33

[60] F. N. Beg, A. R. Bell, A. E. Dangor, C. N. Danson, A. P. Fews, M. E. Glinsky, B. A. Hammel, P. Lee, P. A. Norreys, and M. Tatarakis, "A study of picosecond laser-solid interactions up to 1019 W cm-2," *Phys. Plasmas*, vol. 4, no. 2, pp. 447–457, 1997. 33, 127

[61] J. Yu, Z. Jiang, J. C. Kieffer, and A. Krol, "Hard x-ray emission in high intensity femtosecond laser-target interaction," *Phys. Plasmas*, vol. 6, no. 4, pp. 1318–1322, 1999. 33

[62] H. Chen, S. C. Wilks, W. L. Kruer, P. K. Patel, and R. Shepherd, "Hot electron energy distributions from ultraintense laser solid interactions," *Phys. Plasmas*, vol. 16, no. 2, 2009. 33

[63] M. G. Haines, M. S. Wei, F. N. Beg, and R. B. Stephens, "Hot-electron temperature and laser-light absorption in fast ignition," *Phys. Rev. Lett.*, vol. 102, no. 4, pp. 1–4, 2009. 33, 54

[64] T. Kluge, T. Cowan, A. Debus, U. Schramm, K. Zeil, and M. Bussmann, "Electron temperature scaling in laser interaction with solids," *Phys. Rev. Lett.*, vol. 107, no. 20, pp. 1–5, 2011. 33

[65] T. Kluge, M. Bussmann, U. Schramm, and T. E. Cowan, "Simple scaling equations for electron spectra, currents, and bulk heating in ultra-intense short-pulse laser-solid interaction," *Phys. Plasmas*, vol. 25, no. 7, 2018. 33

[66] K. Eidmann, T. Kawachi, A. Marcinkevičius, R. Bartlome, G. D. Tsakiris, K. Witte, and U. Teubner, "Fundamental and harmonic emission from the rear side of a thin overdense foil irradiated by an intense ultrashort laser pulse," *Phys. Rev. E - Stat. Nonlinear, Soft Matter Phys.*, vol. 72, no. 3, pp. 1–9, 2005. 34

[67] Z. M. Sheng, K. Mima, J. Zhang, and H. Sanuki, "Emission of electromagnetic pulses from laser wakefields through linear mode conversion," *Phys. Rev. Lett.*, vol. 94, no. 9, pp. 1–4, 2005. 34

[68] F. Quéré, C. Thaury, P. Monot, S. Dobosz, P. Martin, J. P. Geindre, and P. Audebert, "Coherent wake emission of high-order harmonics from overdense plasmas," *Phys. Rev. Lett.*, vol. 96, no. 12, pp. 2–5, 2006. 34

[69] S. Kahaly, S. Monchocé, H. Vincenti, T. Dzelzainis, B. Dromey, M. Zepf, P. Martin, and F. Quéré, "Direct observation of density-gradient effects in harmonic generation from plasma mirrors," *Phys. Rev. Lett.*, vol. 110, no. 17, pp. 1–5, 2013. 34, 120, 127

[70] A. Tarasevitch, K. Lobov, C. Wünsche, and D. Von Der Linde, "Transition to the relativistic regime in high order harmonic generation," *Phys. Rev. Lett.*, vol. 98, no. 10, pp. 10–13, 2007. 34, 127

[71] P. Gibbon, "Harmonic generation by femtosecond laser-solid interaction: A Coherent "water-window" light source?," *Phys. Rev. Lett.*, vol. 76, no. 1, pp. 50–53, 1996. 34

[72] L. Plaja, L. Roso, K. Rzazewski, and M. Lewenstein, "Generation of attosecond pulse trains during the reflection of a very intense laser on a solid surface," *J. Opt. Soc. Am. B*, vol. 15, no. 7, p. 1904, 1998. 34

[73] P. A. Norreys, M. Zepf, S. Moustaizis, A. P. Fews, J. Zhang, P. Lee, M. Bakarezos, C. N. Danson, A. Dyson, P. Gibbon, P. Loukakos, D. Neely, F. N. Walsh, J. S. Wark, and A. E. Dangor, "Efficient Extreme UV Harmonics Generated from Picosecond Laser Pulse Interactions with Solid Targets," *Phys. Rev. Lett.*, 1996. 34, 35

[74] M. Zepf, G. D. Tsakiris, G. Pretzler, I. Watts, D. M. Chambers, P. A. Norreys, U. Andiel, A. E. Dangor, K. Eidmann, C. Gahn, A. Machacek, J. S. Wark, and K. Witte, "Role of the plasma scale length in the harmonic generation from solid targets," *Phys. Rev. E - Stat. Physics, Plasmas, Fluids, Relat. Interdiscip. Top.*, 1998. 34

[75] B. Dromey, M. Zepf, A. Gopal, K. Lancaster, M. S. Wei, K. Krushelnick, M. Tatarakis, N. Vakakis, S. Moustaizis, R. Kodama, M. Tampo, C. Stoeckl, R. Clarke, H. Habara, D. Neely, S. Karsch, and P. Norreys, "High harmonic generation in the relativistic limit," *Nat. Phys.*, vol. 2, no. 7, pp. 456–459, 2006. 34

[76] R. Lichters, J. Meyer-ter Vehn, and A. Pukhov, "Short-pulse laser harmonics from oscillating plasma surfaces driven at relativistic intensity," *Phys. Plasmas*, vol. 3, no. 9, pp. 3425–3437, 1996. 34

[77] V. L. Ginzburg and I. M. Frank, "Radiation of a uniformly moving electron due to its transition from one medium into another," *J.Phys.(USSR)*, vol. 9, pp. 353–362, 1945. 35

[78] L. C. L. Yuan, "Some new developments on transition radiation detectors for high-energy particles," *Invit. Talk ESRO Work. Frascati 1974*, 1974. 35

[79] U. Happek, A. J. Sievers, and E. B. Blum, "Observation of coherent transition radiation," *Phys. Rev. Lett.*, vol. 67, no. 21, pp. 2962–2965, 1991. 35

[80] J. S. Nodvick and D. S. Saxon, "Suppression of coherent radiation by electrons in a synchrotron," *Phys. Rev.*, vol. 96, no. 1, pp. 180–184, 1954. 35

[81] J. D. Jackson., *Classical electrodynamics*. second edi ed., 1998. 35, 38

[82] L. C. L. Yuan, C. L. Wang, H. Uto, and S. Prunster, "Formation-Zone Effect in Transition Radiation Due to Ultrarelativistic Particles˜," *Phys. Rev. Lett.*, vol. 25, no. 21, pp. 1689–1699, 1970. 35

[83] M. L. Cherry, G. Hartmann, D. Miiller, and T. A. Prince, "Transition radiation from relativistic electrons in periodic radiators," *Phys. Rev. D*, 1974. 36

[84] C. Bellei, J. R. Davies, P. K. Chauhan, and Z. Najmudin, "Coherent transition radiation in relativistic lasersolid interactions," *Plasma Phys. Control. Fusion*, vol. 54, no. 3, 2012. 38, 65, 66, 77, 79

[85] J. J. Santos, A. Debayle, P. Nicolaï, V. Tikhonchuk, M. Manclossi, D. Batani, A. Guemnie-Tafo, J. Faure, V. Malka, and J. J. Honrubia, "Fast electron transport and induced heating in aluminium foils," *J. Phys. Conf. Ser.*, vol. 112, no. Part 2, 2008. 38

[86] P. F. Moulton, "Spectroscopic and laser characteristics of Ti:Al_2O_3," *J. Opt. Soc. Am. B*, vol. 3, no. 1, p. 125, 1986. 39

[87] K. W. Delong, R. Trebino, K. W. Delong, R. Trebino, and S. N. Laboratories, "Improved ultrashort pulse-retrieval algorithm for frequency-resolved optical gating," *J. Opt. Soc. Am. A*, vol. 11, no. 9, pp. 2429–2437, 1994. 43

[88] R. Trebino and D. J. Kane, "Using phase retrieval to measure the intensity and phase of ultrashort pulses: frequency-resolved optical gating," *J. Opt. Soc. Am. A*, vol. 10, no. 5, p. 1101, 1993. 43

[89] M. J. V. Streeter, *Ultrafast Dynamics of Relativistic Laser Plasma Interactions*. PhD thesis, 2013. 44, 45, 77

[90] B. YANG, R. HS, J. SEO, and J. KIM, "Design, Construction and Calibration of a GRENOUILLE, Single-Shot, Ultrashort-Pulse Measurement System," *J. Korean Phys. Soc.*, vol. 52, no. 2, pp. 269–274, 2008. 46

[91] E. Wigner, "On the quantum correction for thermodynamic equilibrium," *Phys. Rev.*, vol. 40, no. 5, pp. 749–759, 1932. 47

[92] A. Goshtasby, "Piecewise linear mapping functions for image registration," *Pattern Recognit.*, vol. 19, no. 6, pp. 459–466, 1986. 49

[93] A. Goshtasby, "Image registration by local approximation methods," *Image Vis. Comput.*, vol. 6, no. 4, pp. 255–261, 1988. 49

[94] T. D. Arber, K. Bennett, C. S. Brady, A. Lawrence-Douglas, M. G. Ramsay, N. J. Sircombe, P. Gillies, R. G. Evans, H. Schmitz, A. R. Bell, and C. P. Ridgers, "Contemporary particle-in-cell approach to laser-plasma modelling," *Plasma Phys. Control. Fusion*, vol. 57, no. 11, 2015. 49, 81

[95] A. Taflove, *Computational Electrodynamics: The Finite Difference Time Domain Method.* 1995. 50

[96] Y. Ping, R. Shepherd, B. F. Lasinski, M. Tabak, H. Chen, H. K. Chung, K. B. Fournier, S. B. Hansen, A. Kemp, D. A. Liedahl, K. Widmann, S. C. Wilks, W. Rozmus, and M. Sherlock, "Absorption of short laser pulses on solid targets in the ultrarelativistic regime," *Phys. Rev. Lett.*, vol. 100, no. 8, pp. 6–9, 2008. 54, 101

[97] R. J. Gray, R. Wilson, M. King, S. D. Williamson, R. J. Dance, C. Armstrong, C. Brabetz, F. Wagner, B. Zielbauer, V. Bagnoud, D. Neely, and P. McKenna, "Enhanced laser-energy coupling to dense plasmas driven by recirculating electron currents," *New J. Phys.*, vol. 20, no. 3, 2018. 54

[98] P. Mulser, D. Bauer, and H. Ruhl, "Collisionless laser-energy conversion by anharmonic resonance," *Phys. Rev. Lett.*, vol. 101, no. 22, pp. 1–4, 2008. 54

[99] M. C. Levy, S. C. Wilks, M. Tabak, S. B. Libby, and M. G. Baring, "Petawatt laser absorption bounded," *Nat. Commun.*, vol. 5, no. May, pp. 1–6, 2014. 54

[100] D. F. Price, R. M. More, R. S. Walling, G. Guethlein, R. L. Shepherd, R. E. Stewart, and W. E. White, "Absorption of ultrashort laser pulses by solid targets heated rapidly to temperatures 1-1000 eV," *Phys. Rev. Lett.*, vol. 75, no. 2, pp. 252–255, 1995. 54

[101] J. R. Davies, "Laser absorption by overdense plasmas in the relativistic regime," *Plasma Phys. Control. Fusion*, 2009. 54

[102] P. K. Singh, Y. Q. Cui, A. Adak, A. D. Lad, G. Chatterjee, P. Brijesh, Z. M. Sheng, and G. R. Kumar, "Contrasting levels of absorption of intense femtosecond laser pulses by solids," *Sci. Rep.*, vol. 5, no. July, pp. 1–7, 2015. 54

[103] P. Mora, "Theoretical model of absorption of laser light by a plasma," *Phys. Fluids*, vol. 25, no. 6, pp. 1051–1056, 1982. 54

[104] S. C. Rae and K. Burnett, "Detailed simulations of plasma-induced spectral blueshifting," *Phys. Rev. A*, vol. 46, no. 2, pp. 1084–1090, 1992. 55, 70

[105] AVT, "Allied Vision Technology (AVT) Marlin F-033 Data Sheet." [Online] https://www.alliedvision.com/en/products/cameras/detail/Marlin/F-033.html, accessed 2019-09-27. 58

[106] C. Bellei, S. R. Nagel, S. Kar, A. Henig, S. Kneip, C. Palmer, A. Sävert, L. Willingale, D. Carroll, B. Dromey, J. S. Green, K. Markey, P. Simpson, R. J. Clarke, H. Lowe, D. Neely, C. Spindloe, M. Tolley, M. C. Kaluza, S. P. Mangles, P. McKenna, P. A. Norreys, J. Schreiber, M. Zepf, J. R. Davies, K. Krushelnick, and Z. Najmudin, "Micron-scale fast electron filaments and recirculation determined from rear-side optical emission in high-intensity laser-solid interactions," *New J. Phys.*, vol. 12, 2010. 65

[107] R. H. H. Scott, F. Perez, J. J. Santos, C. P. Ridgers, J. R. Davies, and K. L. Lancaster, "A study of fast electron energy transport in relativistically intense laser- plasma interactions with large density scalelengths A study of fast electron energy transport in relativistically intense laser-plasma interactions with large density scalelength," *Phys. Plasmas*, vol. 053104, no. May, pp. –, 2012. 65

[108] S. Kar, A. P. Robinson, D. C. Carroll, O. Lundh, K. Markey, P. McKenna, P. Norreys, and M. Zepf, "Guiding of relativistic electron beams in solid targets by resistively controlled magnetic fields," *Phys. Rev. Lett.*, vol. 102, no. 5, pp. 1–4, 2009. 65

[109] L. Romagnani, A. P. Robinson, R. J. Clarke, D. Doria, L. Lancia, W. Nazarov, M. M. Notley, A. Pipahl, K. Quinn, B. Ramakrishna, P. A. Wilson, J. Fuchs, O. Willi, and M. Borghesi, "Dynamics of the Electromagnetic Fields Induced by Fast Electron Propagation in Near-Solid-Density Media," *Phys. Rev. Lett.*, vol. 122, no. 2, p. 25001, 2019. 65

[110] G. G. Scott, C. M. Brenner, V. Bagnoud, R. J. Clarke, B. Gonzalez-Izquierdo, J. S. Green, R. I. Heathcote, H. W. Powell, D. R. Rusby, B. Zielbauer, P. McKenna, and D. Neely, "Diagnosis of Weibel instability evolution in the rear surface density scale lengths of laser solid interactions via proton acceleration," *New J. Phys.*, vol. 19, no. 4, 2017. 65

[111] R. H. Scott, F. Pérez, M. J. Streeter, E. L. Clark, J. R. Davies, H. P. Schlenvoigt, J. J. Santos, S. Hulin, K. L. Lancaster, F. Dorchies, C. Fourment, B. Vauzour, A. A. Soloviev, S. D. Baton, S. J. Rose, and P. A. Norreys, "Fast electron beam measurements from relativistically intense, frequency-doubled laser-solid interactions," *New J. Phys.*, vol. 15, 2013. 66

[112] C. Bellei, *Measurements of Optical Radiation from High-Intensity Laser-Plasma Interactions*. PhD thesis, 2009. 66

[113] E. Eckner, J. Bierbach, C. Roedel, M. Zepf, S. Kuschel, M. Yeung, and G. G. Paulus, "Long-term operation of surface high-harmonic generation from relativistic oscillating mirrors using a spooling tape," *Opt. Express*, vol. 23, no. 9, p. 12321, 2015. 70

[114] M. Borghesi, A. J. Mackinnon, A. R. Bell, G. Malka, C. Vickers, O. Willi, J. R. Davies, A. Pukhov, and J. Meyer-Ter-Vehn, "Observations of collimated ionization channels in aluminum-coated glass targets irradiated by ultraintense laser pulses," *Phys. Rev. Lett.*, vol. 83, no. 21, pp. 4309–4312, 1999. 79

[115] L. Gremillet, F. Amiranoff, S. D. Baton, J. C. Gauthier, M. Koenig, E. Martinolli, F. Pisani, G. Bonnaud, C. Lebourg, C. Rousseaux, C. Toupin, A. Antonicci, D. Batani, A. Bernardinello, T. Hall, D. Scott, P. Norreys, H. Bandulet, and H. Pépin, "Time-resolved observation of ultrahigh intensity laser-produced electron jets propagating through transparent solid targets," *Phys. Rev. Lett.*, vol. 83, no. 24, pp. 5015–5018, 1999. 79

[116] G. S. Hicks, *Ion beams accelerated by laser irradiation of thin foils and their applications.* PhD thesis, 2016. 93

[117] B. Gonzalez-Izquierdo, M. King, R. J. Gray, R. Wilson, R. J. Dance, H. Powell, D. A. Maclellan, J. McCreadie, N. M. H. Butler, S. Hawkes, J. S. Green, C. D. Murphy, L. C. Stockhausen, D. C. Carroll, N. Booth, G. G. Scott, M. Borghesi, D. Neely, and P. McKenna, "Towards optical polarization control of laser-driven proton acceleration in foils undergoing relativistic transparency," *Nat. Commun.*, vol. 7, p. 12891, 2016. 97

[118] J. Diels and W. Rudolph, *Ultrashort laser pulse phenomena.* Elsevier Academic Press, second edi ed., 2006. 105

[119] L. Yin, B. J. Albright, K. J. Bowers, D. Jung, J. C. Fernández, and B. M. Hegelich, "Three-dimensional dynamics of breakout afterburner ion acceleration using high-contrast short-pulse laser and nanoscale targets," *Phys. Rev. Lett.*, vol. 107, no. 4, pp. 1–4, 2011. 115

[120] M. Zepf, E. L. Clark, F. N. Beg, R. J. Clarke, A. E. Dangor, A. Gopal, K. Krushelnick, P. A. Norreys, M. Tatarakis, U. Wagner, and M. S. Wei, "Proton Acceleration from High-Intensity Laser Interactions with Thin Foil Targets," *Phys. Rev. Lett.*, vol. 90, no. 6, p. 4, 2003. 120

[121] F. Quéré, C. Thaury, J. P. Geindre, G. Bonnaud, P. Monot, and P. Martin, "Phase properties of laser high-order harmonics generated on plasma mirrors," *Phys. Rev. Lett.*, vol. 100, no. 9, pp. 1–4, 2008. 120

[122] B. Dromey, D. Adams, R. Hörlein, Y. Nomura, S. G. Rykovanov, D. C. Carroll, P. S. Foster, S. Kar, K. Markey, P. McKenna, D. Neely, M. Geissler, G. D. Tsakiris, and M. Zepf, "Diffraction-limited performance and focusing of high harmonics from relativistic plasmas," *Nat. Phys.*, vol. 5, no. 2, pp. 146–152, 2009. 121

[123] M. J. Streeter, P. S. Foster, F. H. Cameron, M. Borghesi, C. Brenner, D. C. Carroll, E. Divall, N. P. Dover, B. Dromey, P. Gallegos, J. S. Green, S. Hawkes, C. J. Hooker, S. Kar, P. McKenna, S. R. Nage, Z. Najmudin, C. A. Palmer, R. Prasad, K. E. Quinn, P. P. Rajeev, A. P. Robinson, L. Romagnani, J. Schreiber, C. Spindloe, S. Ter-Avetisyan, O. Tresca, M. Zepf, and D. Neely, "Relativistic plasma surfaces as an efficient second harmonic generator," *New J. Phys.*, 2011. 121, 127

[124] M. J. Duff, R. Wilson, M. King, B. Gonzalez-Izquierdo, A. Higginson, S. D. R. Williamson, Z. E. Davidson, R. Capdessus, N. Booth, S. Hawkes, D. Neely, R. J. Gray, and P. McKenna, "High order mode structure of intense light fields generated via a laser-driven relativistic plasma aperture," *Sci. Rep.*, 2019. 135